Channel Modeling and Multiple Access Solutions for Medical Wireless Body-Area Networks based on Optical Wireless Technology

Oussama Haddad

École Doctorale – 352

Unité de recherche – INSTITUT FRESNEL

THÈSE DE DOCTORAT

pour obtenir le grade de

DOCTEUR de l'ÉCOLE CENTRALE de MARSEILLE

Discipline :

Optique, Photonique et Traitement d'Image

TITRE DE LA THÈSE :

Modélisation de canal et solutions d'accès multiple pour les réseaux corporels basés sur la technologie d'optique sans-fil dans un milieu hospitalier

Par

HADDAD Oussama

Directeur de thèse : KHALIGHI Ali
Co-Directeur de thèse : ADEL Mouloud

Soutenue le 07 Juillet 2021

Devant le jury composé de :

Mme. JULIEN-VERGONJANNE Anne	Professeur–HDR, ENSIL, Limoges	Présidente de jury
M. CLAVIER Laurent	Professeur - HDR, Université Lille-Douai	Rapporteur
M. LE GUENNEC Yannis	MdC - HDR, Université Grenoble Alpes	Rapporteur
M. ZUBOW Anatolij	Professeur–HDR, Université Technique de Berlin	Examinateur
M. SIMON Eric	MdC – HDR, Université de Lille	Examinateur
M. ZVANOVEC Stanislav	Professeur–HDR, Université Technique de Prague	Examinateur
M. KHALIGHI Ali	MdC – HDR, École Centrale Marseille	Directeur de thèse
M. ADEL Mouloud	Professeur – HDR, Université Aix-Marseille	Codirecteur de thèse

ÉCOLE CENTRALE MARSEILLE

N° attribué par la bibliothèque
XXXX

TITRE:

Modélisation de canal et solutions d'accès multiple pour les réseaux corporels basés sur la technologie d'optique sans-fil dans un milieu hospitalier

THÈSE
pour obtenir le grade de DOCTEUR

délivré par L'ÉCOLE CENTRALE MARSEILLE

École Doctorale : Physique et Sciences de la Matière
Mention : Optique, Photonique et Traitement d'Image

Effectuée à l'INSTITUT FRESNEL
Présentée et soutenue publiquement par:

Oussama HADDAD le 07 Juillet 2021

Directeur de thèse: M. Mohammad-Ali KHALIGHI
Co-Directeur de thèse: M. Mouloud ADEL

JURY :

Mme Anne JULIEN-VERGONJANNE	ENSIL, Limoges, France	Présidente de jury
M. Laurent CLAVIER	Université Lille-Douai, France	Rapporteur
M. Yannis LE GUENNEC	Université Grenoble Alpes , France	Rapporteur
M. Anatolij ZUBOW	Université Téchnique de Berlin, Allemagne	Examinateur
M. Eric Pierre SIMON	Université de Lille, France	Examinateur
M. Mohammad-Ali KHALIGHI	École Centrale Marseille, France	Directeur de thèse
M. Mouloud ADEL	Université Aix-Marseille, France	Codirecteur de thèse
M. Stanislav ZVÁNOVEC	Université Téchnique Tchéque	Invité

ANNEE : 2021

ÉCOLE CENTRALE MARSEILLE

N° assigned by library
XXXX

TITLE:

Channel Modeling and Multiple Access Solutions for Medical Wireless Body-Area Networks based on Optical Wireless Technology

THESIS
to obtain the degree of Doctor of Philosophy

issued by ÉCOLE CENTRALE MARSEILLE

Doctoral school : Physics and Material Sciences
Discipline : Optics, Photonics and Image Processing

Carried out at INSTITUTE FRESNEL
Presented and defended publicly by:

Oussama HADDAD on July 07th 2021

Thesis advisor: Dr. Mohammad-Ali KHALIGHI
Thesis co-advisor: Prof. Mouloud ADEL

COMMITTEE :

Prof. Anne JULIEN-VERGONJANNE	ENSIL, Limoges, France	Panel chair
Prof. Laurent CLAVIER	Lille-Douai University, France	Reviewer
Dr. Yannis LE GUENNEC	Grenoble Alpes University, France	Reviewer
Prof. Anatolij ZUBOW	Technische Universitat Berlin, Germany	Examiner
Dr. Eric Pierre SIMON	Lille University, France	Examiner
Dr. Mohammad-Ali KHALIGHI	École Centrale Marseille, France	Thesis supervisor
Prof. Mouloud ADEL	Aix-Marseille University, France	Thesis co-supervisor
Prof. Stanislav ZVANOVEC	Czech Technical University in Prague	Invited

YEAR : 2021

Acknowledgments

The work presented in this thesis was mainly carried out in Institut Fresnel. I would like to express my sincere gratitude to the École Centrale Marseille, who offered me the opportunity to carry out the research here. I also would like to acknowledge VISION Action for providing me the financial support to visit the lab of Telecommunications at Czech Technical University in Prague, and carry out a collaboration work in my thesis. I wish here to express sincere thanks to my supervisors Dr.Mohammad-Ali Khalighi and Prof. Mouloud Adel for their continuous guidance, support and encouragement throughout my PhD study. Without their constructive advice and reading the material without delay including this thesis, it would have been impossible to finish my research work on time. Also, I would like to thank Prof. Anatolij Zubow for his valuable advices.

Résumé étendu

La croissance de la population vieillissante et des maladies chroniques d'une part, et les progrès des technologies sans fil à courte portée d'autre part, ont suscité un intérêt croissant pour le développement de systèmes de télé-surveillance et de télé-soins médicaux grâce à l'utilisation de capteurs médicaux, également connus sous le nom de réseaux de capteurs corporels sans fil (WBAN). Ils sont constitués de réseaux de nœuds de capteurs médicaux (SN) situés á l'intérieur, sur, ou á l'extérieur du corps humain. Les capteurs sont connectés á un nœud central de coordination (CN), placé sur le corps, qui collecte les données et les transmet á un point d'accès (AP). Ce dernier, à son tour, effectue un prétraitement sur ces données avant de les transmettre, par exemple á un centre médical, où elles seront stockées et analysées par le personnel médical. Les applications typiques de ces réseaux comprennent la surveillance á distance des signes vitaux et la stimulation thérapeutique afin d'améliorer la qualité de vie des patients et réduire les coûts de traitement.

Les WBAN médicaux ont des exigences spécifiques qui les différencient des autres réseaux, notamment une fiabilité élevée, une faible consommation d'énergie, et un niveau de sécurité de données très élevé. Lorsqu'ils sont basés sur la technologie des radiofréquences (RF), ils doivent également garantir un faible taux d'absorption spécifique (SAR). Étant donné que la plupart des solutions WBAN actuellement proposées utilisent des ondes RF dans la bande de fréquences ISM, il y a un risque élevé d'interférences électromagnétiques avec les autres réseaux coexistants. De plus, les liaisons RF sont en général plus sujettes à des variations temporelles de canal dues principalement á l'évanouissement multi-trajets (small-scale fading). Ces considérations ont motivé l'étude de technologies alternatives (ou complémentaires) telles que les communications optiques sans fil (OWC) pour les réseaux WBAN médicaux. Ici, les principaux avantages de l'OWC incluent leur immunité aux interférences externes, n'étant pas affecté par le smale-scale fading, ainsi que leur sécurité inhérente due aux propriétés de confinement de la lumière. De toute évidence, une caractérisation et une modélisation précises du canal optique sont une condition préalable á la conception de techniques de transmission efficaces répondant aux exigences des systèmes WBAN médicaux. Aussi, étant donné la particularité des canaux optiques basés sur la modulation d'intensité et la détection directe (IM/DD), une étude dédiée des techniques d'accès multiple (MA) adéquates doit être réalisée. Dans cette thèse, nous nous intéressons á la caractérisation des canaux WBAN basés sur la technologie OWC et le problème d'accès multiple de différents SN dans le cadre des applications médicales.

Après avoir donné un aperçu des technologies WBANs et OWC au chapitre 1, nous décrivons au chapitre 2 les principaux blocs du système OWC, à savoir l'émetteur (Tx), le canal et le récepteur (Rx). Les caractéristiques des LED et les types de modulation utilisés dans nos travaux sont expliqués. Nous expliquons également les propriétés du canal optique et les modèles de canal disponibles ainsi que les principaux critères utilisés pour le caractériser. Ici, les méthodes de tracé de rayons (raytracing) déterministes et statistiques sont décrites avec une discussion de

leurs avantages et inconvénients. En ce qui concerne le Rx, nous expliquons les processus de photodétection et de démodulation dans le cas des Rxs basés sur des photodiodes PIN et APD et discutons les principales sources de bruit qui peuvent affecter la fiabilité de la transmission dans chacun des cas.

Dans le chapitre 3, nous discutons en détail les concepts théoriques de calcul de l'impulsion de canal (CIR) via l'approche Monte-Carlo Raytracing (MCRT), ainsi que la méthodologie d'analyse des performances des liaisons. Après avoir présenté le modèle analytique du MCRT, nous introduisons la méthode numérique utilisant le logiciel Zemax (Opticstudio). Ici, les détails du raytracing, la spécification de l'environnement 3D, la modélisation de la mobilité locale et globale du patient ainsi que le placement des capteurs sont présentés. Ensuite, nous discutons de la caractérisation statistique des canaux dynamiques à l'aide de l'estimation du modèle d'approximation optimal (best-fit model) et de densité de noyau (kernel densité) ainsi que l'évaluation de la probabilité de blocage.

Le chapitre 4 traite de la modélisation des canaux et de l'analyse des performances des liaisons intra-WBAN, càd, des SN vers le CN. Ici, nous prenons en considération la mobilité locale et globale du corps, où nous modélisons le mouvement des parties du corps en utilisant une animation 3D d'un cycle de marche et des trajectoires aléatoires basées sur un modèle random waypoint (RWP) modifié. Après avoir spécifié les paramètres de simulation, nous présentons les résultats de la simulation sur l'évolution temporelle du gain de canal, du retard de propagation et du temps de cohérence, ainsi que leur distribution statistique pour les liaisons intra-WBAN correspondantes. Ensuite, étant donné la nature aléatoire dynamique du canal et sur la base des modèles d'approximation optimale, nous évaluons les performances des liaisons à l'aide de la probabilité de blocage pour un schéma de modulation simple on-off keying (OOK). Nous évaluons les performances des Rx basés sur les photodiodes PIN et APD dans différentes conditions de bruit de fond. Nous montrons l'impact considérable de la position et de l'orientation du corps à l'intérieur de la pièce sur les variations du gain du canal. Les liens intra-WBAN sont fortement impactés par le shadowing et le blocage et leurs statistiques peuvent être mieux modélisées avec une distribution Gamma. Les canaux optiques peuvent néanmoins être considérés comme flat-fading pour des débits faibles á modérés. Ils présentent également des variations de temps plus lentes (temps de cohérence typiques de quelques secondes), par rapport à leurs homologues RF (temps de cohérence de plusieurs dizaines de ms). Cela permet d'utiliser des tailles de paquet plus grandes pour le premier, donc un surcoût pilote plus faible et un contrôle de puissance simplifié sur les trames successives. Concernant la fiabilité de la liaison, elle est significativement affectée par le shadowing résultant de la mobilité locale du patient, qui dépend également de la position du CN. Nous montrons aussi qu'étant donné les contraintes sur la complexité du système et la consommation d'énergie, un Rx (CN) basé sur une photodiode PIN est le choix approprié pour les liens intra-WBANs.

Avec une approche similaire à celle utilisée au chapitre 4, nous étudions le canal extra-WBAN, càd, du CN vers l'AP, et évaluons ses performances dans le chapitre 5. Nous considérons dif-

férentes configurations pour le CN et étudions les avantages de l'utilisation de plusieurs AP dans la chambre. Les résultats des principales métriques de canal, exposées précédemment, et l'analyse de la probabilité de blocage pour les Rx basés sur PIN et APD sont présentés et l'impact du bruit est discuté. Nous proposons une estimation de densité de noyau basée sur des noyaux Gaussiens pour les canaux extra-WBAN et montrons que l'utilisation d'une APD au Rx (AP) est la mieux adaptée sauf sous des conditions de fortes radiations ambiantes. Cela permet une robustesse accrue contre le shadowing lors de l'utilisation d'un PD plus sensible, ainsi qu'une réduction du niveau de puissance IR requise au Tx (CN). Enfin, la fiabilité de la liaison extra-WBAN peut être considérablement améliorée en utilisant plusieurs APs, ce qui réduit significativement le blocage des faisceaux lors des mouvements de l'utilisateur. Bien que l'utilisation de plusieurs APs augmente la complexité d'implémentation du réseau, elle peut se justifier compte tenu de l'amélioration des performances obtenue, notamment en ce qui concerne la réduction substantielle de la puissance d'émission requise.

Après avoir étudié les canaux intra et extra WBAN et évalué leurs performances, nous nous concentrons dans le chapitre 6 sur les techniques d'accès multiple (MA). Compte tenu du nombre potentiellement important de SN qui pourraient être utilisés pour chaque patient, le développement de schémas MA robustes dans la couche physique (PHY) est assez difficile. Une gestion MA plus efficace peut être obtenue grâce á la couche de contrôle d'accès au support (MAC) en minimisant les collisions de paquets et leur planification pour garantir une consommation d'énergie et un délai d'accès acceptables. Après avoir fourni un aperçu général des solutions de couche PHY et MAC, nous évaluons l'utilisation de schémas de multiplexage de fréquence tels que m-CAP MA, basé sur la modulation d'amplitude et phase sans porteuse à bande multiple (m-CAP) et montrons leurs performances compte tenu de canaux WBAN réalistes obtenus dans les chapitres précédents. Ensuite, compte tenu des limites des schémas MA basés sur la planification et/ou sur l'accès aléatoire, nous proposons au chapitre 7 l'utilisation du schéma d'accès aléatoire par mise en file d'attente distribuée (DQRA) multi-canal. Le schéma proposé a une meilleure efficacité énergétique, un accès transparent au canal et une flexibilité à gérer un flux de données hétérogènes. Nous présentons le modèle système du schéma DQRA basé sur l'OWC et fournissons une analyse analytique des principales métriques telles que le délai d'accès et la consommation d'énergie.

Enfin, les conclusions générales de la thèse avec certaines orientations de recherche possibles pour de futures études sont présentées au chapitre 7.

Table of contents

List of Acronyms **1**

1 General Introduction **3**

1.1 Introduction . . . 3

1.2 WBAN overview . . . 4

1.2.1 WBANs for Medical Applications . . . 4

1.2.2 Architecture of a WBAN . . . 6

1.2.3 Specific Requirements of Medical WBANs . . . 6

1.2.4 Existing Wireless Technologies for WBANs and Related Works . . . 7

1.3 OWC overview . . . 10

1.3.1 Technology . . . 10

1.3.2 OWC advantages and challenges . . . 10

1.3.3 OWC applications . . . 11

1.4 Thesis objectives . . . 14

1.5 Thesis overview and contributions . . . 15

1.5.1 Thesis outline . . . 15

1.5.2 Author's contributions . . . 17

1.5.3 Author's publications . . . 17

2 Fundamentals of OWC Communication **19**

2.1 Introduction . . . 19

2.2 Transmitter . . . 20

2.2.1 Optical source . . . 20

2.2.2 Modulation . . . 21

2.3 Receiver . . . 25

2.3.1 Photodetector 26
2.4 Channel 28
2.4.1 LOS 29
2.4.2 NLOS 29
2.5 Noise sources 30
2.5.1 Thermal noise 31
2.5.2 Background noise 31
2.5.3 Dark noise 31
2.5.4 Shot noise 31
2.6 Channel Characterization and Modeling 32
2.7 Chapter summary 33

3 WBAN Channel Modeling and Link Performance 35
3.1 Introduction 35
3.2 Modeling of dynamic channel 36
3.2.1 Potential Equation 36
3.2.2 RWP Mobility Model 38
3.2.3 Channel Characterization 39
3.2.4 Simulation validation 40
3.2.5 Statistical Channel Modeling 41
3.3 Numerical Simulation of intra-WBAN links 42
3.3.1 Simulation Methodology 42
3.3.2 Sensor Placement 43
3.3.3 User Mobility Modeling 45
3.3.4 Link Performance Analysis 47
3.4 Chapter summary 48

4 Channel Modeling and Performance Analysis of Intra-WBANs 49
4.1 Introduction 49
4.2 Environment Description and Parameter Specification 50
4.3 Channel characterization 50
4.3.1 Channel DC Gain 52
4.3.2 Delay Spread 54

4.3.3 Channel Dynamic Behavior . . . 55
4.3.4 Statistical Analysis of Channel Gain . . . 58
4.3.5 Channel Coherence Time . . . 59
4.4 Performance analysis . . . 60
4.4.1 Effect of PD Type and Data-Rate . . . 61
4.4.2 Comparison of Intra-WBAN Links for Low Background Noise Level . . . 62
4.4.3 Comparison of Intra-WBAN Links for Relatively High Background Noise Level 64
4.5 Chapter summary . . . 65

5 Channel Modeling and Performance Analysis of Extra-WBAN links 67
5.1 Introduction . . . 67
5.2 Simulation Approach . . . 68
5.2.1 General Assumptions . . . 68
5.3 Channel Characterization, Numerical Results . . . 69
5.3.1 Single AP Configurations . . . 69
5.3.2 Multiple AP Configurations . . . 70
5.3.3 Channel RMS Delay Spread . . . 71
5.3.4 Channel Coherence Time . . . 73
5.4 Link Performance Analysis . . . 73
5.4.1 Statistical Model of Channel Gain . . . 73
5.4.2 Performance Comparison of Single and Multiple AP Configurations . . . 75
5.4.3 Performance Comparison of PIN- and APD-based Rxs . . . 76
5.5 Chapter summary . . . 76

6 Multiple Access Management for Intra-WBAN Links 79
6.1 Introduction . . . 79
6.2 TDMA . . . 80
6.3 FDMA . . . 82
6.3.1 multi-user multi-band CAP (m-CAP) (MU m-CAP) . . . 82
6.4 Contention-based schemes . . . 86
6.4.1 ALOHA . . . 86
6.4.2 CSMA/CA . . . 86
6.5 DQRA Scheme . . . 88

6.5.1 DQ-MAC Description and modeling 89
6.5.2 Performance Metrics 91
6.5.3 Performance analysis 92
6.6 Chapter summary 94

7 Conclusions and Perspectives **95**
7.1 Conclusions 95
7.2 Perspectives 97

A **99**
A.1 Angles range of variation for each node 99
A.2 Detailed description of channel time variations for the cases of local and global mobility 100
A.2.1 Local mobility case 100
A.2.2 Global mobility case 100
A.3 Best-fit PDFs for H_0 for individual SN links 101

List of Figures **103**

List of Tables **107**

Bibliography **109**

List of Acronyms

ACF	autocorrelation function
ACK	acknowledgment
ACO-OFDM	assymetrically clipped optical Orthogonal frequency division multiplexing (OFDM)
ADO-OFDM	assymetrically clipped direct current (DC) biased optical OFDM
AIC	Akaike information criterion
AP	access point
APD	avalanche photodiode
ARS	access request sequences
AWGN	additive white Gaussian noise
BER	bit error rate
BLE	Bluetooth low-energy
BPSK	binary phase shift keying
BR/EDR	basic rate/enhanced data-rate
BRDF	bi-directional reflection distribution function
BSN	body sensor networks
CAD	computer-aided design
CAP	Carrierless amplitude and phase modulation
CDMA	code-division multiple access (MA)
CF	contention feedback
CIR	channel impulse response
CN	coordinator node
CR	contention resolution
CRQ	contention resolution queue
CRW	contention resolution window
CSMA/CA	carrier-sense MA with collision avoidance
DAC	digital-to-analogue converter
DC	direct current
DCO-OFDM	DC biased optical OFDM
DD	direct detection

DIFS	distributed inter-frame space
DQ	distributed queuing
DQRA	distributed queuing (DQ) random access
DTQ	data transmission queue
DTW	data transmission window
ECG	electrocardiogram
EEG	electroencephalogram
EGC	equal gain combining
EMG	electromyogram
EMI	electromagnetic interference
FBP	feedback packet
FDD	frequency division duplexing
FDMA	frequency-division MA
FFT	fast Fourrier transform
FIFO	first-in first-out
FIR	finite impulse response
FOV	field-of-view
FSO	Free-space optical
FSOI	free-space optics interconnects
FWHM	full width at half maximum
GPS	global positionning system
HAP	high altitude platforms
HBC	human body communication
HSTN	heterogeneous satellite and terrestrial networks
ICI	inter-channel interference
IFFT	inverse fast Fourrier transform
IM	intensity modulation
IM/DD	intensity modulation and direct detection
IoT	Internet-of-things
IR	infrared
IrDA	Infrared Data Association
ISI	inter-symbol interference
ISM	industrial, scientific, and medical
KDE	kernel density estimate
LACO-OFDM	layered assymetrically clipped optical OFDM (ACO-OFDM)
LAN	local area network
LD	laser diode
LE	low-energy
LED	light-emitting diode
LEO	low earth orbit

LiFi	light-fidelity
LOS	line-of-sight
LPF	low-pass filter
m-CAP	multi-band CAP
M2M	machine to machine
MA	multiple access
MAC	media-access control
MCRT	Monte-Carlo raytracing
MEMS	micro-electro-mechanical systems
MICS	medical implant communication service
MIMO	multiple-input multiple-output
MLD	maximum likelihood detection
mmW	millimeter wave
MoCap	motion capture
MTBF	mean time between failures
MU m-CAP	multi-user m-CAP
NAC	new-user access control
NACK	negative acknowledgment
NLOS	non line-of-sight
NM-CAP	non-orthogonal m-CAP
NRZ	non-return-to-zero
OCC	optical camera communications
OFDM	Orthogonal frequency division multiplexing
OFDMA	orthogonal frequency-division MA
OOC	optical orthogonal codes
OOK	ON-OFF keying
OWC	optical wireless communication
PAM	Pulse amplitude modulation
PAM-DMT	PAM discret multi-tone modulation
PAPR	peak to average power ratio
PD	photodetector
PDF	probability density function
PER	packet error transmission
PHY	physical
PIN	P-i-N
PL	path-loss
PPM	Pulse position modulation
PR	packet radio
PSD	power spectral density
QAM	quadrature amplitude modulation

QoS	quality-of-service
RF	radio frequency
RMS	root mean squared
RWP	random waypoint
Rx	receiver
SAR	specific absorption rate
SC	selection combining
SN	sensor node
SNR	signal-to-noise ratio
SO2	pulse oximetry
SRRC	square-root raised-cosine
STL	standard tessellation language
TBS	terrestrial base stations
TDD	time division duplexing
TDMA	time-division MA
TIA	transimpedance amplifier
Tx	transmitter
U-OFDM	unipolar OFDM
UAV	unmanned-aerial-vehicle
UV	utlra-violet
UWB	ultra-wideband
UWC	underwater communications
V2I	vehicle-to-infrastructure
V2V	vehicle-to-vehicle
VCSEL	vertical-cavity surface-emitting laser
VL	visible light
VLC	visible light communication
VLSI	very-large-scale integration
WBAN	wireless body area network
WHO	World Health Organization
WiFi	wireless fidelity
WMTS	wireless medical telemetry service
WPAN	wireless personal-area network
WSN	wireless sensor networks

Chapter 1

General Introduction

Contents

1.1 Introduction . . . 3
1.2 WBAN overview . . . 4
1.2.1 WBANs for Medical Applications . . . 4
1.2.2 Architecture of a WBAN . . . 6
1.2.3 Specific Requirements of Medical WBANs . . . 6
1.2.4 Existing Wireless Technologies for WBANs and Related Works . . . 7
1.3 OWC overview . . . 10
1.3.1 Technology . . . 10
1.3.2 OWC advantages and challenges . . . 10
1.3.3 OWC applications . . . 11
1.4 Thesis objectives . . . 14
1.5 Thesis overview and contributions . . . 15
1.5.1 Thesis outline . . . 15
1.5.2 Author's contributions . . . 17
1.5.3 Author's publications . . . 17

1.1 Introduction

According to the World Health Organization (WHO), Life expectancy is consistently increasing and this trend will continue thanks to more efficient medical follow-up of the newborns and a better epidemics prevention and control [1],[2]. At the same time, the changing lifestyle is resulting in an increased mortality rate due to cardiovascular diseases [3] as well as an increased number of chronic diseases such as diabetes [4]. These trends will put more and more pressure on the health-care systems, increasing the treatment costs for both health centers and patients.

With the advances made in the different fields of engineering, smart solutions can be developed to endorse traditional health-care methods. In particular, the advances in very-large-scale integration (VLSI) had made possible the integration of diverse sensors and micro-electro-mechanical systems (MEMS) in millimeter-size chips [5–7]. Furthermore, with the development of low-power short-range communication technologies, wireless connection of these sensors and actuators can be readily done, giving rise to wireless sensor networks (WSN)s, which are the building blocks of an Internet-of-things (IoT) network [8]. Indeed, the progress made in cloud computing and machine learning has made computing power and data analysis available at very low costs [9], which has, in turn, allowed removing the processing load from these WSNs.
The application of WSN technology to health-care has given birth to body sensor networks (BSN)s or wireless body area network (WBAN)s, which consist of networks of medical sensors located inside, on, or outside the human body. By the aid of such networks, early detection of health emergencies can be made possible. They can also be used for remote monitoring of vital signs of patients such as electrocardiogram (ECG), electroencephalogram (EEG), and temperature, as well as for remote drug delivery such as by insulin pumps. The obvious benefit of using such networks is in saving lives by offering a more efficient and reactive health-monitoring and treatment of patients with chronic conditions, as well as in cost reduction. Compared with general WSNs, WBANs have specific characteristics including: The relatively small number of network nodes, the necessity of a very small delay latency; the non-stationary nature of the networks due to the movement of the patients; and the heterogeneity of the type of transmitted signals (that can be a mixture of continuous-time signals like ECG and event-based signals like temperature) [10].
A number of relatively recent works have studied different aspects of radio frequency (RF) based WBANs. In [10], a survey of a few WBAN-related projects and enabling technologies at hardware and connectivity levels was presented. In [11], WBAN physical and data link layers were investigated, whereas the design of corresponding media-access control (MAC) and network layer protocols were discussed in [12] together with solutions for a cross layer design. In [13], Movassaghi *et al.* presented in particular the different layers of the IEEE 802.15.6 standard dedicated to WBANs. Also, the requirements for wireless technologies that can be used for these networks were discussed in [14], and a survey on the related textile-based sensors was presented in [15].

In the next two sections of this chapter, we present a general overview of WBANs and optical wireless communication (OWC).

1.2 WBAN overview

1.2.1 WBANs for Medical Applications

The use of WBANs has been considered for different applications including medical, military, sport, interactive gaming, etc [16]. Here, we focus on the application of these networks in the medical domain. Figure 1.1 illustrates typical scenario of a hospital ward with several patients

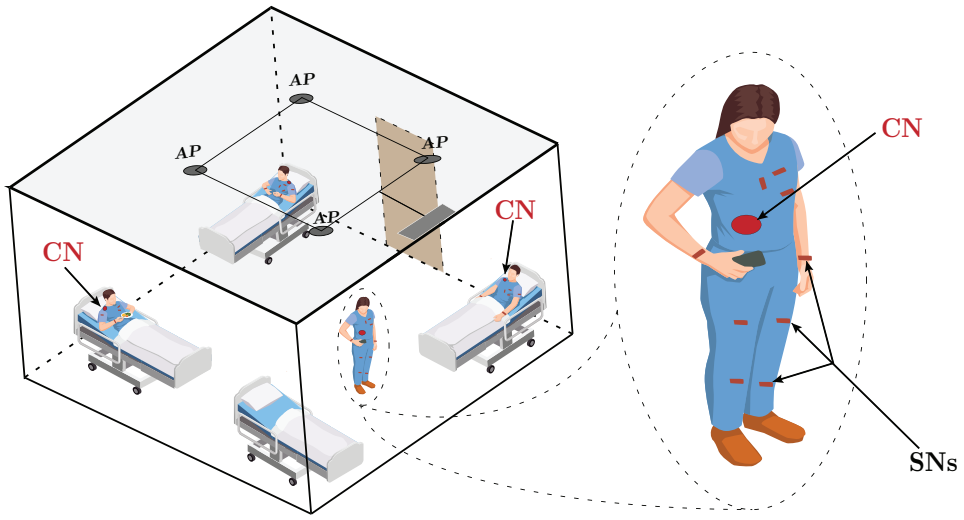

Figure 1.1 — Typical hospital ward scenario with several patients equipped with medical WBANs.

equipped with medical WBANs. These, sensor node (SN)s collect the medical data and then send them to a coordinator node (CN) that could be placed on the body. The CN then forwards the data to an access point (AP).

Such a WBAN can be used for continuous monitoring of vital signs such as ECG, EEG, electromyogram (EMG), blood glucose level, blood pressure, heart rate, body temperature, motion, etc. The related physiological signals can be used to monitor or diagnose diseases such as cardiovascular disease, diabetes, epilepsy, as well as for monitoring, sleep, stress, activity, etc. Some typical relevant physiological sensors include: ECG sensors to record the heart electrical activity, i.e., the electrical changes that arise from the pattern of polarizing and depolarizing of the heart muscles; EEG sensors to record the brain electrical activity using several electrodes placed along the scalp to measure voltage fluctuations resulting from ionic currents within the neurons; EMG sensors to record the electrical activity produced by skeletal muscles by measuring the electric potential generated by muscle cells when electrically or neurologically activated; and pulse oximetry (SO2) sensor to measure the blood oxygen saturation based on the changing absorbance of two wavelengths of light passing through the body and determining the absorbance corresponding to the pulsing arterial blood. Continuous monitoring of these vital signs helps also detect health emergencies in order to alarm physicians or health practitioners for early interventions, especially in the case of elderly people and disabled persons.

Another important application of WBANs is to deliver therapeutic treatments via actuators that work through electrical stimulation or biochemical injections. Typical examples are: pacemakers that deliver electrical impulses through electrodes to regulate the electrical conduction of the heart; cochlear implants that is used to capture sound using a microphone and to convert it to an electrical signal to stimulate directly the auditory nerve; neuromuscular stimulators that deliver electrical impulses muscles, mimicking the action of the central nervous system; and insulin pump used for administering the delivery of insulin based on the blood glucose level. Some other

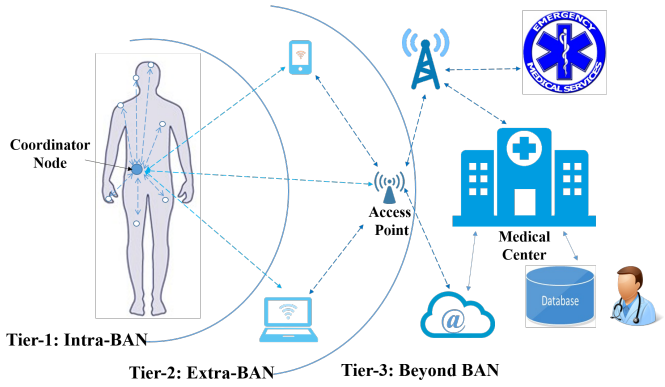

Figure 1.2 — A typical WBAN with the underlying communication tiers.

examples include defibrillator, brain stimulator, artificial retina, etc.

1.2.2 Architecture of a WBAN

The general architecture of a WBAN consists of three different tiers: intra-WBAN with a typical transmission range on the order of tens of centimeters, extra-WBAN, and beyond-WBAN communications, as illustrated in Fig. 1.2 [13]. As we mentioned earlier, for the first tier, i.e., intra-WBAN, communication takes place between SNs on or inside the body on one hand, and a CN on the other hand. SNs can be either sensors that measure physiological data, or actuators that upon feedback information from sensors, conduct an electrical or biochemical stimulation.
As concerns extra-WBAN tier, communication takes place between the CN and one or more APs, which can be part of the infrastructure or be placed in an ad-hoc mode. After collecting data from different SNs, the CN transmits it to the AP, probably after preprocessing, e.g., data fusion or compression. The communication between the AP and the medical center concerns the third tier, which is done via local area network (LAN) or a cellular network, for instance. The received data could be stocked in a database and/or used by the medical staff for real-time diagnosis or monitoring.

1.2.3 Specific Requirements of Medical WBANs

As mentioned previously, a WBAN used in medical applications has special requirements that differentiate it from other sensor networks. We briefly present these considerations in the following.
Data rate and link reliability: Based on the target application, nodes in a WBAN have different requirements in terms of data rate, which can range from a few bits per second (bps), e.g. for a temperature sensor, to a few Mbps, e.g., for capsule endoscopy. According to the IEEE 802.15.6 standard requirements, WBAN links have to support data rates in the range of 10 Kbps to 10 Mbps [17]. Meanwhile, the network should satisfy requirements in terms of quality-of-service (QoS) to ensure reliable communication, which is usually specified in terms of bit error rate (BER). The

Table 1.1 — Requirements on data-rate and BER for some medical applications [18, 19].

Sensor nodes	Target data rate	Target BER
ECG	72 Kbps	$< 10^{-10}$
EEG	86.4 Kbps	$< 10^{-10}$
EMG	1.536 Mbps	$< 10^{-10}$
SPO2	32 bps	$< 10^{-10}$
Temperature, glucose level, pH	20 bps	$< 10^{-10}$
Cochlear implant	$\sim$ 200 Kbps	$< 10^{-10}$
Deep brain stimulation	128 – 320 Kbps	$< 10^{-3}$
Accelerometer, blood pressure	< 10 Kbps	$< 10^{-10}$
Endoscope capsule	1 Mbps	$< 10^{-10}$

BER requirement depends on the medical device and can vary from 10^{-3} for deep brain stimulation to 10^{-10} for EEG recording. Also, the required delay latency for medical applications is less than 125 ms [17]. Table 1.1 presents typical data-rate and BER requirements for some WBAN applications [18, 19].

Energy consumption: Obviously, low energy consumption is an important feature of WBANs because it affects the battery lifetime of the medial devices. Battery lifetime is in particular crucial for implant devices where replacing power sources needs a costly surgical operation, although ongoing research considers harvesting techniques to recharge the device batteries remotely [20, 21]. Moreover, a high energy consumption may cause a temperature rise in the tissue that surrounds the sensor. As the human tissue is semi-conductive, it will absorb a part of the radiations emitted at transmission, which can cause severe thermal damage to sensitive organs. The amount of energy absorption is defined by the so-called specific absorption rate (SAR) that needs to be minimized for WBAN sensors. The upper limit of SAR exposure is fixed to 2 W/Kg over 10 g of tissue according to the standards in the European Union countries and Japan, and 1.6 W/Kg over 1 g of tissue in the United States and Australia, which are equivalent to maximum transmit powers of 20 and 1 W, respectively [17].

Security and privacy: Security is of high concern in medical WBANs since medical data is considered as sensitive, private, and confidential. As such, data should be encrypted to ensure user's privacy, and authentication mechanisms should be used to verify data integrity and to ensure that data is being sent from a trusted node. This is an important issue in RF-based networks where data-carrying signals can be intercepted and jammed relatively easily, as we will discuss later.

1.2.4 Existing Wireless Technologies for WBANs and Related Works

RF technologies: Most of the current realizations of WBAN systems are based on the rather well-known wireless personal-area network (WPAN) technologies (initially IEEE 802.15) operating in

the 2.4 GHz industrial, scientific, and medical (ISM) band. Bluetooth as a popular short-range communication system [22] with two main modes of basic rate/enhanced data-rate (BR/EDR) and low-energy (LE), has received particular attention. It is especially the case for the fourth version, known as Bluetooth low-energy (BLE), designed for device-to-device communications with low complexity, low cost, and low power consumption, offering data rates up to 2 Mbps. The most recent (i.e., the fifth) version of Bluetooth, specially developed for IoT device connectivity, has different power classes that can serve different ranges of 100, 10, and 1 m, with a maximum transmit power of 100, 2.5, and 1 mW, respectively.

Another solution is the IEEE 802.15.4 standard [23], which was developed for low-cost wireless connectivity for applications with limited power and relaxed throughput requirements. With a simple and flexible protocol, it offers data rates from 20 to 250 Kbps within a typical range of 10 m and a transmit power limited to 10 mW. The popular Zigbee [24] is a low-cost and low-power technology built on the top of IEEE 802.15.4 standard by modifying the network and application layers. Lastly, the short-range low-power IEEE 802.15.6 standard [25] was specifically designed for WBANs, offering up to 15 Mbps data-rate with a transmit power between 0.1 and 1 mW. It has been developed to overcome the limitations of the other existing WPANs to meet the requirements of medical applications discussed in Section 1.2.3. This standard defines narrow-band transmission in the ISM, wireless medical telemetry service (WMTS), and medical implant communication service (MICS) bands, as well as ultra-wideband (UWB) and human body communication (HBC), with data-rates in the range of 57.5 – 971.4 Kbps for narrow-band transmission, 0.487 – 15.6 Mbps for UWB, and 164 Kbps – 1.3 Mbps for HBC (operating at 21 MHz).

Although Bluetooth and Zigbee do not meet the requirements in terms of data-rate, reliability, and SAR of certain medical applications (e.g., in hospital environments) [18], most of the reported WBAN implementations rely on these standards [26–31]. However, to the best of the author's knowledge, no realization of WBANs has been reported based on IEEE 802.15.6, which can be explained by the availability of Bluetooth and Zigbee transceivers and their ease of use, compared to the former. For instance, a system for monitoring temperature and heart rate was proposed in [28] based on Power-Class 2 (with a maximum emitted power of 2.5 mW) EDR Bluetooth module. In [27] a 3-lead ECG system was designed to measure the respiration rate, based on a Power-Class 2 BLE module. A similar device was used in [32] for a wearable WBAN with solar energy harvesting to measure body temperature, heart rate, and fall detection.

Concerning Zigbee applications, a wearable system was designed in [31] comprising of an accelerometer and temperature and humidity sensors, using an IEEE 802.15.4 compatible transceiver capable of implementing Zigbee protocols and transmitting at 2 mW. Also, a wearable system equipped with global positionning system (GPS) and 3-lead ECG was proposed in [33] for the purpose of fall detection and assisting elderly people. A health monitoring system equipped with a 1-lead ECG, a pulse sensor, and a body weight sensor was also designed in [34] where a Zigbee transceiver module with 6.3 mW was used to interconnect sensors with a CN, and a Bluetooth v.2 module with 2.5 mW to connect this latter to an AP.

Ultrasonic technologies: Ultrasonic communications are enabled by the propagation of acoustic

waves inside the human body at frequencies higher than 20 KHz. They have the potential to complement or replace RF technologies for implant communications thanks to their low attenuation in the human tissues. Transceivers used for ultrasonic communications are mainly piezoelectric transducers. In [35], an implantable pressure sensor was tested with a data-rate of 40 Kbps and a transmit power of 100 μW through a 12 cm tick castor oil. Also, in [36] an ultrasonic wideband system communicating through a human kidney phantom at 10 cm was demonstrated with a data-rate of 700 Kbps and a power consumption of 40 μW at a BER of 10^{-6}.

Optical wireless technologies: OWC in the infrared (IR), visible, or utlra-violet (UV) parts of the spectrum are a potential alternative or complement to RF technologies for medical WBANs thanks to their high immunity to external interference and their inherent security due to confinement of optical waves in indoor spaces. In addition, the transmit power in OWC systems is not constrained by SAR regulations unlike RF counterparts. The interest of the optical wireless technologies has been investigated in several works for on-body, extra-body, and in-body medical applications.

The use of OWC for on-body WBAN links was investigated in [19], where their practical feasibility was demonstrated. Characterizing the communication channel using ray-tracing based numerical simulations, the authors evaluated the theoretical performance of an optical link using ON-OFF keying (OOK) modulation and code-division MA (CDMA) for connecting several sensors for the case of purely diffuse links (i.e., without a line-of-sight (LOS)). They showed a BER of 10^{-10} for data-rates from 10 to 890 Kbps, with a power consumption of 17 mW for 10 Kbps data-rate, which is much lower than the maximum permitted emitted power for IR communications (based on eye safety regulations) [19]. Lower power consumption would be attainable using more efficient transmission schemes, however.

Concerning extra-WBAN links, a bidirectional OWC system was studied in [37] for connecting a CN with an AP, where visible light communication (VLC) was used for the downlink (the AP being integrated into a light-emitting diode (LED) luminaire, for instance) and IR transmission for the uplink. It was shown that for most medical sensors, it is possible to satisfy QoS and data-rate requirements with a low radiated power for both IR and VLC links. Moreover, the use of OWC for transmitting accelerometer data for indoor physical activity monitoring was investigated in [38] where its efficacy was demonstrated through experimental measurements using a designed wearable system.

On the other hand, in-body communication in the optical domain has attracted increasing attention in the past few years as it provides a better performance in terms of data rate and interference level, as compared to RF technologies [39–41]. For instance, a transdermal optical link operating at 1 Mbps through porcine skin was reported in [39] using a 860 nm LED at the transmitter and a P-i-N (PIN) photo-diode at the receiver. Also, a telemetry system based on a laser diode (LD) was studied in [42] with a data rate of 16 Mbps through a skin thickness of 4 mm and a power consumption of less than 10 mW. Experimental results were also presented in [43] for data transmission through a 1 mm thick chicken derma, where a data rate of 20 Kbps at a BER of 10^{-6} was reported with both direct and retroflection links with a power consumption of 4 mW and 0.4 μW, respectively. Using a vertical-cavity surface-emitting laser (VCSEL) laser, a transmission

Figure 1.3 — Block diagram of a typical OWC system.

link through a 4 mm tissue was demonstrated in [44], achieving 50 Mbps data rate at BER of 10^{-5} with a power consumption of 4.1 mW. An extension of this study was done in [45], where a data rate of 100 Mbps at a BER of 2×10^{-7} was achieved with a power consumption of 2.1 mW through a tissue of an anesthetized sheep of 2.5 mm thickness. These results were further extended in [46] to a bidirectional link through a 2 mm porcine skin, achieving 1 Mbps with a power consumption of 290 μW in downlink and 100 Mbps with 3.2 mW in uplink.

1.3 OWC overview

As was mentioned previously, OWC is an alternative or complementary technology to RF, which covers the UV, visible light (VL), and IR bands. OWC enjoys from a huge unregulated spectrum (400 THz in bandwidth) and offers numerous advantages compared to RF and ultrasound solutions, including immunity to external interference and inherent security due to confinement of light in indoor spaces.
In this Section, we will review the main applications of OWC as well as its advantages and main challenges.

1.3.1 Technology

A typical OWC system consists of a transmitter (Tx), the optical channel, and a receiver (Rx), as illustrated in Fig. 1.3. The Tx employs either a LD or a LED depending on the targeted application. On the other hand, a photodetector (PD) is used at the Rx. As for the optical channel, the LOS configuration is the best in terms of achievable data rate and link reliability. However, due to user mobility and link blockage and shadowing, the received signal usually arises from diffuse component (corresponding to multipath propagation), which results in high path-loss (PL) and channel dispersion. OWC systems generally use intensity modulation and direct detection (IM/DD) due to its low cost and implementation complexity. When a non-coherent source (like an LED) is used at the Tx, IM/DD is the only transmission solution.

1.3.2 OWC advantages and challenges

OWC offers a number of advantages compared to RF systems. We summarize them as follows.
High data rate: The use of optical spectrum offers ultra-large bandwidth of 400 THz, which potentially enables data transmission with high data-rates.
Unlicensed spectrum: The very large optical spectrum is currently free and unlicensed, unlike

the RF spectrum which is expensive and regulated, in addition to being increasingly congested.
Inherent security: Due to the confinement properties of light in indoor environment and the narrow beams used in outdoor applications, OWC links benefit from inherent security and make their interception a relatively hard task.
Ease of deployment: OWC transceivers often use off-the-shelf components, which allows their easy deployment in both indoor and outdoor environments with a relatively affordable cost.
Immunity to EMIs: The use of very large optical bandwidth and the confinement properties of light, mentioned above, enables easy frequency reuse and thus dealing with electromagnetic interference (EMI).

On the other hand, OWC faces some challenges that need to be addressed for a robust, operational implementation. We mention the most important challenges of OWC in the following.

Signal level fluctuations: OWC links are susceptible to LOS link blockage by obstacles between the Tx and Rx, which can cause transmission interruption or, otherwise, random signal fluctuations due to shadowing. Note that small-scale fading is mostly negligible due to the fact that the PD surface area is much larger than the optical signal wavelength. Nevertheless, signal level fluctuations may occur due to pointing errors and misalignment in point-to-point links or due to atmospheric turbulence in outdoor scenarios.
Eye safety: Laser safety standards impose an upper-limit on optical transmit power, which restricts the achievable performance especially for narrow beam and narrow field-of-view (FOV) links.

1.3.3 OWC applications

OWC applications can be classified based on their transmission range, starting from ultra-short range communications in inter-chip wireless communications to ultra-long range communications as for space communications [47–49]. Figure 1.4 illustrates some of these applications. We distinguish the following applications.

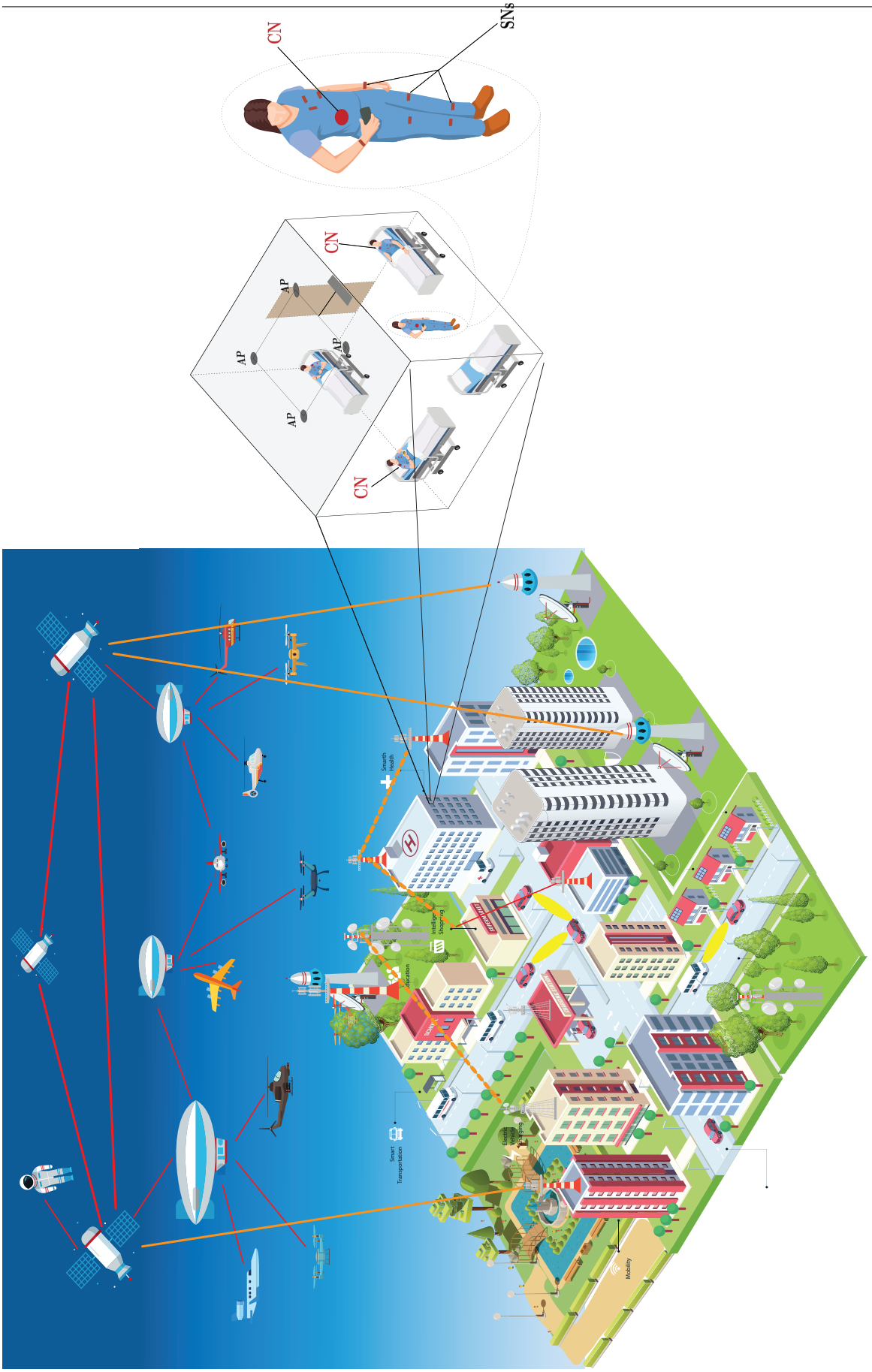

Figure 1.4 — OWC applications.

Ultra-short range applications: The standard copper-based electrical interconnects have become a major bandwidth bottleneck for ultra high data rate, low latency, data centers and super computer systems. Also, their lack of reconfigurability does not enable them to adjust to the network topology and traffic patterns. Within this context, free-space optics interconnects (FSOI) can provide ultra-high data rate and EMI-robust alternative [50]. FSOI have a great potential to address issues such as bandwidth, latency, and power consumption. In addition, the development of optical transmission, switching, and control and management have an important impact on the flexibility and scalability of data centers [51].

Short range applications (tens of centimeters): The growing deployment of LEDs for illumination infrastructures has encouraged the investigation of VLC systems to enable both lighting and communication in indoor environments. These systems are commonly referred to as light-fidelity (LiFi), which can improve the spectral density, compared to their RF counterparts (i.e., wireless fidelity (WiFi)) networks [52]. Nowadays, many short-range indoor applications can be addressed through the use of OWC. For instance, indoor localization using VLC technologies can provide a low-cost, high accuracy system where the classical GPS cannot be used, such as in indoor public spaces (i.e., malls, train stations, airports), tunnels, hospitals, factories, etc. [53, 54]. Another example is optical camera communications (OCC), where cameras (imaging sensors) are used as optical Rx to enable machine to machine (M2M)) communications [55]. Also, OWC was proposed for aircraft cabin communications to replace the wired networks and thus reduce the weight and flying costs [56, 57]. Lastly, optical WBANs were proposed to complement the growing RF-based WBANs as discussed above [19].

Medium range applications (several meters): Similar to indoor applications, the availability of LED-based lighting systems in outdoor environment has led to the development of optical vehicle-to-vehicle (V2V) and vehicle-to-infrastructure (V2I) communications [58, 59]. Here, the front and back lighting of cars can be used to transmit information to the adjacent cars in order to enable applications such as platooning, autonomous driving, etc. Another application of OWC is in underwater communications (UWC) [60–63], where VLC (generally in the green and blue wavelength range) can be used to augment/complement the traditional acoustic communications, enabling much higher data-rates.

Long range applications (hundreds of meters to several kilometers): Free-space optical (FSO) systems can be deployed for high speed point-to-point data transmission. Here, the use of narrow laser beams gives the link an inherent security and an immunity to EMI, as well as a high reuse factor [64]. However, FSO links are vulnerable to fog and snowfalls, which can cause a severe performance degradation and failure. To solve this, hybrid millimeter wave (mmW) RF/FSO links are used to complement each other in cases of fog or rain [65]. FSO networks are, in particular, proposed as first- and last-mile solution for high data rates applications to bridge the gap between the end users and the existing fiber optics infrastructure [66, 67]. Furthermore, FSO can provide a viable solution for high capacity inter-building links in enterprises with decentralized offices or university campuses [68]. Due to their ease of deployment, FSO links can serve in remote areas and disaster situations, where the communication infrastructure could be

damaged or non existing [64]. Last, FSO links have been investigated for mobile platforms such as for unmanned-aerial-vehicle (UAV)-to-ground and UAV-to-UAV communications [69]. These applications would require reliable tracking algorithms to enable strong LOS links [70].

Ultra-long range applications: Aerospace communications could also benefit from the advantages of OWC, mentioned above. For instance, coherent FSO links can be used for space-to-ground and space-to-space communications,thus benefiting from a high Rx sensitivity and a high spectral efficiency [71, 72]. Also, FSO links can be used for heterogeneous satellite and terrestrial networks (HSTN)s, especially for air-to-air, air-to-ground, and space-to-air links between UAVs, low earth orbit (LEO) satellite, high altitude platforms (HAP)s, and terrestrial base stations (TBS) [73–75].

1.4 Thesis objectives

This dissertation focuses on the characterization and modeling of optical-based WBAN channels as well as on the design of suitable signaling schemes to address the requirement of multiple access management (regarding to data transmission from multiple sensors) in the physical (PHY) and MAC transmission layers. This work has been supported by VisIoN, a European project funded by the European Union's Horizon 2020 research and innovation program under the Marie Skłodowska-Curie Grant Agreement No. 764461. Under the framework of vision project, I have been involved in the work package 4, on "Manufacturing and Medical". I have benefited from a secondment in the communications lab of Czech technical university in Prague (CTU) (for 4 months) and a virtual secondment to the technical university of Berlin (TUB) (for 2 months).

In summary, regarding WBAN channel characterization, in order to accurately model the mobility and shadowing effects of the body, we have considered animation based 3D body walk cycles and walk trajectories based on an improved random waypoint (RWP) mobility model. In fact, the movements of the body parts change the link geometry (related to body posture) between the Tx and the Rx, which could occasionally result in LOS blockage or beam shadowing. Moreover, body movement inside a room exhibits a correlation between consecutive sequences of the walk trajectory, which needs to be taken into consideration for a realistic channel model. As a result, appropriate non-uniform mobility modeling needs to be considered within this context. Also, given the potentially large number of nodes that could be used for each WBAN, developing a robust MA scheme is quite challenging. Therefore, we have considered efficient MA management through the MAC layer by minimizing packet collisions and their scheduling to ensure acceptable energy consumption and access delay.

The main questions we try to answer in this thesis are: how to evaluate the impact of body shadowing and mobility on the intra-WBAN and extra-WBAN communication channels, and how to represent this impact within the channel models in order to evaluate the link performance. We also look for appropriate MA schemes for the case of intra-WBAN links that satisfy the low-energy,

low-complexity, high-reliability and low-latency requirements of WBANs. To reach these objectives, we have proceeded as follows:

- Reviewed the fundamentals of the indoor OWC systems, with a special focus on the modeling of dynamic channels via Monte-Carlo raytracing (MCRT) simulations (presented in **Chapters 2** and **3**).
- Characterized the WBAN channel using first- and second- order statistics while considering the effects of mobility and body shadowing during a walk cycle and evaluated their performance considering different ambient noise conditions, SN, CNs and APs configurations, as well as different Rx types (presented in **Chapter 4** and **5**).
- Evaluated the performance of MA techniques such as MU m-CAP and their combination with the DQ random access (DQRA) and analyzed its performance in terms of energy efficiency and access delay, while comparing it to its RF counterpart (presented in **Chapter 6**).

1.5 Thesis overview and contributions

1.5.1 Thesis outline

This dissertation contains 7 chapters, including this Introduction as **Chapter 1**.
Chapter 2 describes the main blocks of an OWC system, i.e., the Tx, the channel and the Rx. The LED characteristics and the types of modulation used in our work are also explained. Also, we explain the optical channel properties and the main metrics used to characterize it. As for the Rx, we explain the photo-detection and demodulation processes for PIN and avalanche photodiode (APD)-based Rxs and discuss the main noise sources that impact the reliability of the transmission for each Rx.
In **Chapter 3**, we discuss in detail the theoretical concepts behind channel impulse response (CIR) computation via the MCRT approach and the link performance analysis methodologies. After presenting the analytical model of MCRT, we introduce the numerical method using Zemax (Opticstudio) software. There, the details of ray-tracing, the 3D environment specifications, local and global mobility modeling as well as sensor placement are presented. Next, we discuss the statistical characterization of dynamic channels using best-fit and kernel density estimation, as well as and outage probability calculation.
Chapter 4 deals with the channel modeling and performance analysis of intra-WBANs uplink, i.e., form the SNs to the CN. There, we take into consideration both local and global movements of the body, where we model the body parts movements by using a 3D animation of a walk cycle and random trajectories based on a modified RWP mobility model. After specifying the simulation parameters, we present simulation results on the temporal evolution of the channel gain, delay spread, and coherence time, as well as on their statistical distribution for the underlying intra-WBAN links. Next, based on best-fit statistical characterization, we evaluate the link perfor-

mance for a simple OOK modulation scheme based on the outage probability criterion. We further evaluate the performances of PIN and APD Rxs under different background noise conditions. We show the high impact of the body position and orientation inside the room on the variations of the channel gain: Intra-WBANs links are shown to be highly impacted with shadowing and blockage, where their statistics can be appropriately modeled with a gamma distribution. Meanwhile, we show that the intra-WBAN channels can nevertheless be considered as effectively flat for low-to-moderate data-rates. They also have slower time variations (typical coherence times of a few seconds), compared to the RF counterparts (coherence times of tens of ms). This allows using larger packet sizes for the former, thus a lower pilot overhead and a simplified power control over successive frames. Concerning the link reliability, we show that it is significantly affected by shadowing resulting from local body mobility, which also depends on the position of the CN. We also show that given the constraints on the system complexity and power consumption, a PIN-based Rx (CN) could be a suitable choice.

Similar to the approach used in **Chapter 4**, we study the extra-WBAN channel by focusing on the uplink data transmission, i.e., from the CN to the AP, and evaluate its performance in **Chapter 5**. We consider different configurations for the CN and investigate the benefit of using multiple APs in the room. Numerical results for the main channel metrics presented previously and outage probability analysis for PIN- and APD-based Rxs are presented and the impact of noise is discussed. We propose a kernel density estimate (KDE) based on Gaussian kernels for the extra-WBAN channels and show that using an APD at the Rx (AP) is best suited except under strong background radiations; this allows increased robustness against shadowing when using a more sensitive PD, as well as reduced required IR power level at the Tx (CN). Lastly, we demonstrate the significant improvement in the extra-WBAN link reliability through the use of multiple APs, which is due to a significant reduction of beam shadowing during user movements. Although the use of multiple APs increases the implementation complexity of the network, it can be justified given the achieved performance improvement, in particular, regarding the substantial reduction of the required transmit power.

After studying the intra- and extra-WBANs channels and evaluating their performance, we focus in **Chapter 6** on the design of appropriate MA techniques. Given the potentially large number of SNs that could be used for each patient, and, furthermore, the presence of several patients in a hospital, developing a robust MA scheme in the PHY layer is quite challenging. More efficient MA management can be achieved through the MAC layer by minimizing packet collisions and their scheduling to ensure acceptable energy consumption and access delay. Therefore, after providing a general overview of PHY and MAC layer techniques solutions, we evaluate the use of frequency multiplexing schemes such as MU m-CAP and investigate their performance considering realistic WBAN channel models. Also, we present the contention-based schemes such as ALOHA and carrier-sense MA with collision avoidance (CSMA/CA) techniques. Next, given the limitations of scheduled- and contention-based MAC schemes, we propose the use of multi-channel DQRA scheme for energy-efficiency, seamless access to the channel, and the flexibility to cope with heterogeneous data traffic. We present the system model of optical-based DQRA scheme and provide

an analytical analysis of the main metrics such as access delay and energy consumption.
Finally, general conclusions of the thesis and some future research directions are presented in **Chapter 7**.

1.5.2 Author's contributions

The main author's contributions in this thesis are summarized in the following.

- Characterization of the intra- and extra-WBAN channels in terms of first- and second-order statistics based on MCRT simulations via Zemax software and proposed a dynamic model that consider realistic mobility and shadowing effects. Derivation of statistical distributions to fit the channel models.
- Evaluation of the outage probability performance of WBAN links for different configurations of ambient light and Rx types.
- Proposition of a DQ-based MAC scheme to decrease energy consumption and access delay in intra-WBAN links.

1.5.3 Author's publications

1. O. Haddad, M. A. Khalighi, "Enabling Communication Technologies for Medical Wireless Body-Area Networks," *2019 Global LIFI Congress (GLC)*, pp. 1–5, June. 2019. Paris, France.
2. O. Haddad, M. A. Khalighi, S. Zvanovec, M. Adel, "Channel Characterization and Modeling for Optical Wireless Body-Area Networks," *IEEE Open Journal of the Communications Society*, vol. 1, pp. 760–776, June. 2020.
3. O. Haddad, M. A. Khalighi, S. Zvanovec, "Channel characterization for optical extra-WBAN links considering local and global user mobility," *Proc. SPIE 11307, Broadband Access Communication Technologies XIV, 113070G* , Jan. 2020, San Francisco, CA.
4. O. Haddad, M. A. Khalighi, S. Zvanovec, "Performance Analysis of Optical Intra-WBAN Links," *12th International Symposium on Communication Systems, Networks and Digital Signal Processing (CSNDSP)*, pp. 1–6, July. 2020, Porto, Portugal.
5. O. Haddad, M. A. Khalighi, S. Zvanovec, "Performance Analysis of Optical Extra-WBAN Links Based on Realistic Channel Modeling," *Optical Engineering*, accepted.
6. O. Haddad, M. A. Khalighi, A. Zubow, "Wireless Body-Area Networks in Medical Applications Using Optical Signal Transmission," *Optical Fiber Conference (Invited paper)*, Jun. 2021, San Francisco, CA.

Chapter 2

Fundamentals of OWC Communication

Contents

2.1 Introduction . . . 19
2.2 Transmitter . . . 20
2.2.1 Optical source . . . 20
2.2.2 Modulation . . . 21
2.2.2.1 Serial transmission . . . 22
2.2.2.2 Multiple sub-carrier techniques . . . 24
2.3 Receiver . . . 25
2.3.1 Photodetector . . . 26
2.3.1.1 PIN . . . 26
2.3.1.2 APD . . . 27
2.4 Channel . . . 28
2.4.1 LOS . . . 29
2.4.2 NLOS . . . 29
2.5 Noise sources . . . 30
2.5.1 Thermal noise . . . 31
2.5.2 Background noise . . . 31
2.5.3 Dark noise . . . 31
2.5.4 Shot noise . . . 31
2.6 Channel Characterization and Modeling . . . 32
2.7 Chapter summary . . . 33

2.1 Introduction

Consider a typical OWC transmission link as illustrated in the block diagram of Fig. 2.1. At the Tx, binary data is modulated in the electrical domain and then passed to the driver, which feeds it to

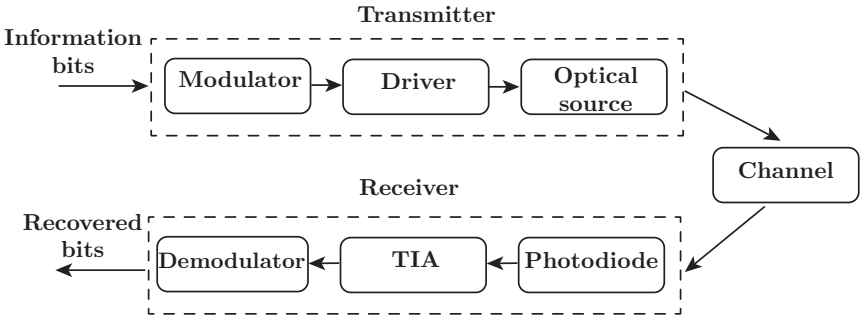

Figure 2.1 — Block diagram of a typical OWC system.

an optical source, which could be a LD or a LED, to convert it into an optical signal. the signal then propagates through the channel to reach the Rx via the LOS or multipath reflections. A PD, which could be a PIN or an APD converts back the optical signal to an electrical signal, which is amplified by a transimpedance amplifier (TIA) before being demodulated. In what follows, we will present in more detail the three main building blocks of the Tx, the channel, and the Rx in Sections 2.2, 2.3, and 2.4, respectively. In Section 2.5, we will discuss the main noise sources affecting the Rx. Section 2.6 presents methods for characterizing the optical channel and some of the main works from the literature. Finally, Section 2.7 concludes the chapter while summarizing the main assumptions that we make on the OWC link, to be used in the subsequent chapters.

2.2 Transmitter

The optical Tx is composed of a modulator, a driver, and an optical source, as illustrated in Fig. 2.1. Information bits are converted to data symbols based on a modulation scheme and then fed through the driver to the optical source for transmission.

2.2.1 Optical source

The optical source converts the signal at the output of the driver, which is in the form of electrical current, to an optical signal, which will propagate through the wireless channel. It consists typically of a semiconductor coherent sources LD or incoherent sources LED with intensity modulation. In contrast to LDs, LEDs are mainly used for low-to-moderate data-rates in indoor applications, and have the advantages of lower cost and wider beam profiles.

Light-emitting diodes: An LED consists of a semiconductor p-n junction that spontaneously emits light when subjected to a forward bias voltage across the junction. The LED electrical-to-optical efficiency is around 20 to 30 percent [76]. Depending on the energy band-gap of the semiconductor, the spectrum of the emitted light can be in the UV, VL, or IR wavelengths. The rate of photon emission and its wavelength are given by [77]:

$$I(E = h\nu) \sim \sqrt{E - E_g}\, exp\left(-\frac{E}{K_b T}\right), \tag{2.1a}$$

$$\lambda = \frac{hc}{E(eV)}\,\mu m, \tag{2.1b}$$

where E_g is the band-gap energy of the semiconductor, ν is the frequency of radiation, E is the energy level, and K_b is the Boltzmann constant. Also, T is the absolute temperature, c is the speed of light, and h is the Planck constant. As we can see from equation (2.1a), the photon emission rate is inversely proportional to the temperature.

An important property of LEDs is their modulation bandwidth, which ranges from a few kHz to hundreds of MHz depending on the type of LED. For instance, organic LEDs have a cut-off frequency around 100 kHz [78, 79], resonant-cavity LEDs offer a 100 MHz [80, 81], and μLEDs can attain a modulation bandwidth of 800 MHz [82]. Another important property is the LED FOV, defined as the angle between the points of maximum and 50 percent directivity in the radiation pattern, or the semi-angle at half-power $\theta_{1/2}$. It ranges generally from ±10 to ±60 degrees. The radiation pattern of an LED can be modeled by a Lambertian pattern P_{li}, which is given by:

$$P_{li}(\theta) = P_{Tx}\,\frac{m+1}{2\pi}\,\cos^m(\theta), \tag{2.2}$$

where P_{Tx} is the transmitted power, θ is the radiation angle, m is the Lambertian order, given by $m = -\ln(2)/\ln(\cos(\theta_{1/2}))$.

Laser diodes: Laser is an acronym for light amplification by stimulated emitted radiation. LD structure is similar to that of LED, except that the former has an optical feedback that consists of a polished mirror for photon amplification [76]. When driven by a low current, the LD has a similar response to an LED where spontaneous emission occurs. However, above a threshold level, sufficient enough to produce a population inversion, the stimulated emission process of coherent light occurs [77]. The later process gives LDs a higher electrical-to-optical conversion efficiency, compared to LEDs (about 30 to 70 percent), at the expense of a more complex driving circuitry and thus a higher cost [83]. Also, LDs have a much larger modulation bandwidth compared to LEDs (typically about tens of GHz), which enables ultra-high data rate transmissions. However, LDs are more subject to temperature variations, compared to LEDs [84].

The normalized spatial distribution of the transmitted intensity I_{ga} at a distance z of a LD source is usually modeled by a Gaussian profile as follows [85]:

$$I_{ga}(\rho, z) = \frac{2}{\pi\, w_z^2}\,\exp\left(-\frac{2\,\|\rho\|^2}{w_z^2}\right), \tag{2.3}$$

where ρ is the radial vector from the beam center and w_z is the beam waist at distance z. The beam-width of an LD source is generally narrow, which makes the effects of misalignment more significant. However, an optical diffuser can be used to enlarge the beam-width and thus reduce the sensitivity to pointing errors.

2.2.2 Modulation

Typically used IM/DD techniques for OWC systems can be classified in two categories: serial transmission or carrier-less modulation, and multiple sub-carrier (usually called "multiple carrier")

modulation. The former exploits all the available bandwidth to transmit signals, while the latter divide the bandwidth into narrow sub-bands, e.g., to restore the channel frequency selectivity. These techniques are adopted from RF systems while accounting for the fact that optical intensity should be real and positive.

2.2.2.1 Serial transmission

serial transmission techniques use intensity modulation (IM) to transmit data by setting the average power P_{avg} and the symbol period T_s. We mention here the most common approaches.

OOK: OOK is the most reported modulation technique for OWC systems due to its implementation simplicity. Here, a bit 'one' is represented by a pulse that occupies the entire or a part of T_s, while a bit 'zero' is represented by the absence of the pulse. For a non-return-to-zero (NRZ) OOK, the pulse representing the bit 'one' occupies the entire T_s, thus the system bandwidth is the same as the system data rate $BW_{NRZ} = R_b$ and the average power is expressed by:

$$P_{\text{avg,OOK}} = \frac{\left(P_{1,\text{OOK}} + P_{0,\text{OOK}}\right)}{2}, \tag{2.4}$$

where $P_{1,\text{OOK}}$ and $P_{0,\text{OOK}}$ are the power of bits 'one' and 'zero', respectively. Figure 2.2(a) illustrates the waveform of an OOK system. In practice, 'one' and 'zero' correspond to 2 different intensity levels, i.e., high and low.

Pulse position modulation (PPM): In PPM, the symbol period T_s is divided into several time slots $M = \log_2(k)$, where k is the number of bits per symbol. Each symbol is assigned to one of the time slots M, while the other time slots being set to zero as it is shown in Fig. 2.2(b). PPM has the best efficiency compared to the other IM/DD techniques. It can be used for relatively low data rate OWC systems, where the bandwidth is not a major concern. The average power of a PPM signal is expressed by:

$$P_{\text{avg,PPM}} = \frac{1}{M}\left(P_{1,\text{PPM}} + (M-1)\,P_{0,\text{PPM}}\right), \tag{2.5}$$

$P_{1,\text{PPM}}$ and $P_{0,\text{PPM}}$ denote the optical power of the 'one' and 'zero' states, respectively. The bandwidth of PPM is given as a function of the data-rate R_b by $\text{BW}_{\text{PPM}} = M R_b / \log_2 M$.

Pulse amplitude modulation (PAM): In PAM, M different intensity levels are used as it is shown in Fig. 2.2(c), each symbol corresponding to $\log_2 M$ bits. It can be considered as the generalization of OOK signaling. The spectral efficiency of PAM is improved as M increases, but at the cost of reduced power efficiency. The m^{th} intensity level of a PAM signaling scheme is given by:

$$P_m = \frac{2\,m\,P_{\text{avg,PAM}}}{M-1} + P_{\text{low,PAM}}, \tag{2.6}$$

where $P_{\text{avg,PAM}}$ is the average optical power and $P_{\text{low,PAM}}$ is the lowest power level used. The bandwidth of PAM is given compared to OOK as $BW_{PAM} = BW_{\text{OOK}} / \log_2 M$.

Carrierless amplitude and phase modulation (CAP): CAP is basically a quadrature amplitude modulation (QAM) where the mixers that are used for up- and down-conversion are replaced by

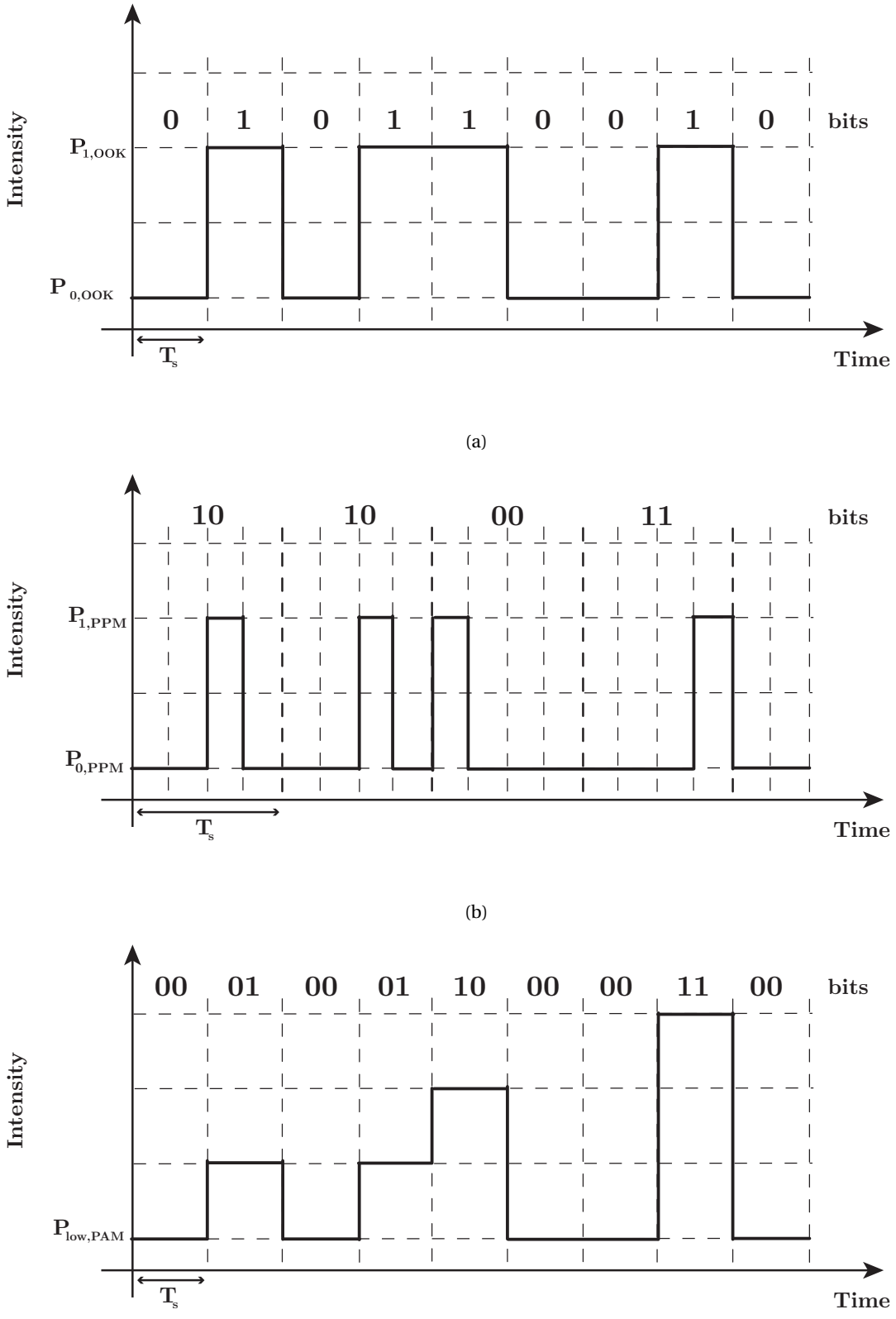

Figure 2.2 — Illustration examples of modulation schemes: (a) OOK, (b) 4-PPM, and (c) 4-PAM.

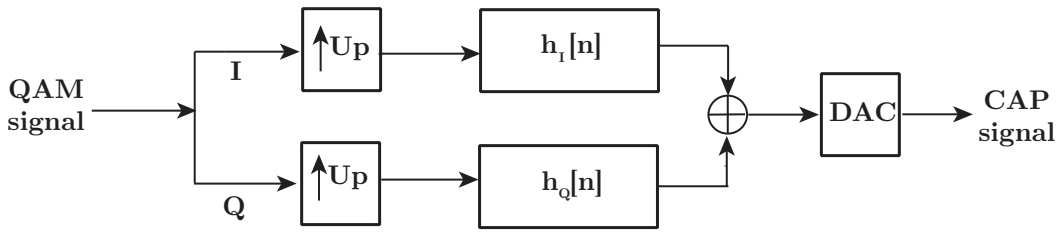

Figure 2.3 — CAP transmission: Blocks denote up-sampler, FIR filers, and DAC.

two orthogonal finite impulse response (FIR) digital filters $h_I[n]$ and $h_Q[n]$ that form a Hilbert-transform pair [86] as it is shown in Fig. 2.3. A square-root raised-cosine (SRRC) filter is used as a shaping filter for in-phase and quadrature signals. Compared to the previously mentioned modulation schemes, CAP can offer a typically higher data rate.

2.2.2.2 Multiple sub-carrier techniques

The previously-mentioned modulation techniques may suffer from inter-symbol interference (ISI) for high data rates necessitating channel equalization, at the cost of increased Rx complexity [86, 87]. Another approach is multiple sub-carrier modulation where the available bandwidth is split into several sub-bands to multiplex the transmitted data on each sub-carrier. We mention here the two main related techniques that are used in the context of OWC.

OFDM: OFDM has been adopted for RF communications to simplify dealing with channel frequency selectivity [76]. Here, frequency multiplexing is done through the use of inverse fast Fourrier transform (IFFT) at the Tx, and likewise, frequency de-multiplexing at the Rx is performed using fast Fourrier transform (FFT) operation. OFDM split the channel into several narrow flat sub-channels, allowing the use of simple single-tap equalizers at the Rx. Bit and power loading can be used to enhance further the system performance. Nevertheless, OFDM signal generally suffer from relatively high peak to average power ratio (PAPR), and consequently the system performance is affected by the so-called clipping noise, due to the limited dynamic range of the Tx. To be used in optical systems, several techniques have been proposed so far to transform the bipolar, complex OFDM signal to a real-valued, unipolar signal [88]. The most famous techniques are DC biased optical OFDM (DCO-OFDM), ACO-OFDM, and unipolar OFDM (U-OFDM). Basically, to get real-valued signals, Hermitian symmetry is imposed through the insertion of symbols complex conjugates on half of the available sub-carriers.

- **DCO-OFDM [89]:** The simplest way to ensure the signal non-negativity is to add a DC bias, equal to the peak negative amplitude, to the bipolar signal. DCO-OFDM offers higher spectral-efficiency but suffers from lower energy-efficiency, compared to the other approaches [90] (see below).

- **ACO-OFDM [63]:** The energy-efficiency of DCO-OFDM can be improved by using ACO-OFDM. Here, only the odd sub-carriers are modulated, followed by negative signal clipping

at zero. As we use only odd sub-carriers, the spectral-efficiency of ACO-OFDM is half that of DCO-OFDM [86].

- **U-OFDM [91]:** Here, the bipolar OFDM symbol is split into its negative and positive parts. The negative part is inverted and then both parts are transmitted using two consecutive OFDM symbols. U-OFDM, also known as flipped-OFDM offers higher power-efficiency compared to DCO-OFDM and ACO-OFDM.

Note that other OFDM variations that offer different properties in term of energy- and spectral-efficiencies have been proposed in the literature. For instance, by assymetrically clipped DC biased optical OFDM (ADO-OFDM), the odd sub-carriers are modulated using ACO-OFDM and the even sub-carriers using DCO-OFDM, offering higher energy-efficiency [92]. Also, by PAM discret multi-tone modulation (PAM-DMT), all sub-carriers are modulated with PAM, but, only the imaginary parts of the symbols are used for data transmission [93], resulting in improved power-efficiency compared to DCO-OFDM, while having the same spectral-efficiency as ACO-OFDM. Lastly, layered ACO-OFDM (LACO-OFDM) can improve the spectral efficiency of ACO-OFDM through the use of multiple layers of transmission [94].

m-CAP: In m-CAP, the available bandwidth is divided into multiple sub-bands, then a CAP modulation is performed on each sub-band, with Hilbert pulse shaping pairs at the center of each sub-band [95]. Similar to OFDM, the channel is transformed to multiple narrow flat-fading sub-channels, where bit and power loading can be further used to improve the link performance. The main advantage of m-CAP, compared to OFDM is its lower PAPR. However, its implementation complexity can be much higher, especially when using a large number of multi-bands. Figure 2.4 shows the power spectral density (PSD) of an m-CAP signal.

A non-orthogonal m-CAP (NM-CAP) scheme was recently proposed to improve further the spectral efficiency of conventional m-CAP without any performance degradation and no additional computational complexity [96]. Here, the filter carrier frequencies are modified to force the compression of sub-carrier spacing below orthogonality, causing overlapping in the adjacent filter pass-bands.

2.3 Receiver

The optical Rx is typically composed of a PD, a TIA, and a demodulator, as illustrated in Fig. 2.1.The PD transforms the received optical signal into electrical current, which is amplified and converted to a voltage using the TIA before direct detection (DD) demodulation. Since the received signal is generally weak due to propagation losses through the channel, the Rx should have a high sensitivity within the operation wavelengths range and a low noise level. Optical concentrators and filters can be used to improve the detection process. This section discusses the main aspects of

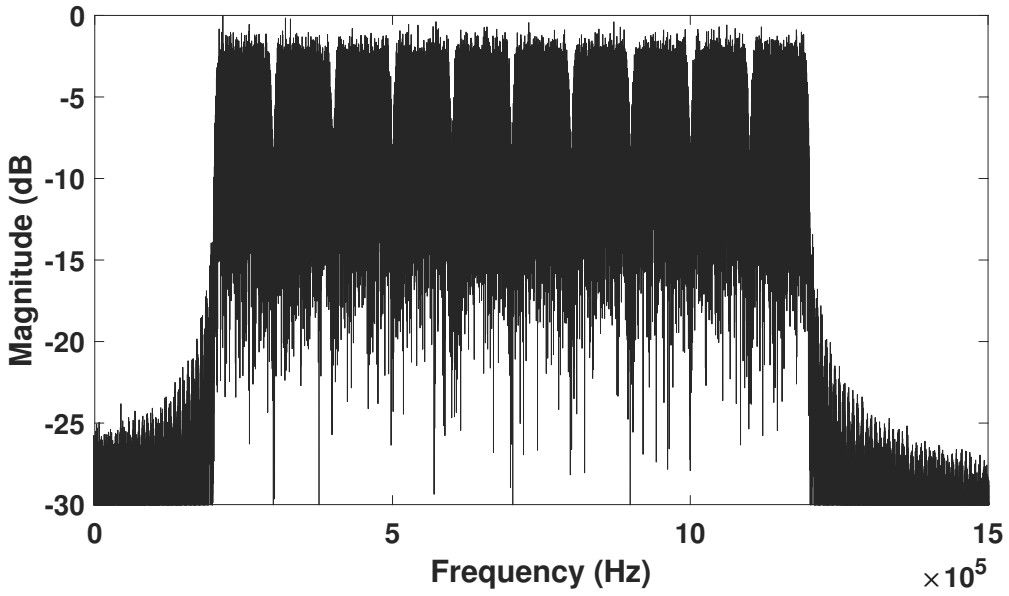

Figure 2.4 — PSD of a m-CAP signal: $m = 10$, $\beta = 0.1$, and system bandwidth is 1 MHz.

PDs, along with the photo-detection techniques that are used in OWC systems.

2.3.1 Photodetector

A PD is an opto-electronic transducer that generates an electrical signal, in the form of current that is proportional to the square of the instantaneous optical field impinging on its surface. The most important characteristics of PDs within the context of OWC are: the detection surface area (i.e., aperture), which should be large enough for photon collection; sensitivity at the operating wavelength; response time which should be short for high data rate applications; and noise level. The PD is characterized usually by its quantum efficiency η_{qe}, which is the ratio of the number of electron-hole generated by a PD to that of the incident photons. The mostly used PDs in the context of OWC are PINs and APDs, that are presented in the following.

2.3.1.1 PIN

A PIN PD consists of a p- and n-type semiconductor material, separated by a lightly n-doped intrinsic region [77]. When a reverse voltage is applied through the PIN diode, sufficient enough to deplete the intrinsic region from any charge carrier, an incident photon with an energy exceeding the band-gap energy will generate a pair of electron-hole that will be collected by the junction. This will lead to the generation of a photo-current that will flow in the external circuit as shown in Fig. 2.5. The generated photo-current I_{PIN} is expressed by:

$$I_{\text{PIN}} = \frac{\eta_{qe}\, q\, \lambda\, P_r}{h\, c} = \mathscr{R}\, P_r, \tag{2.7}$$

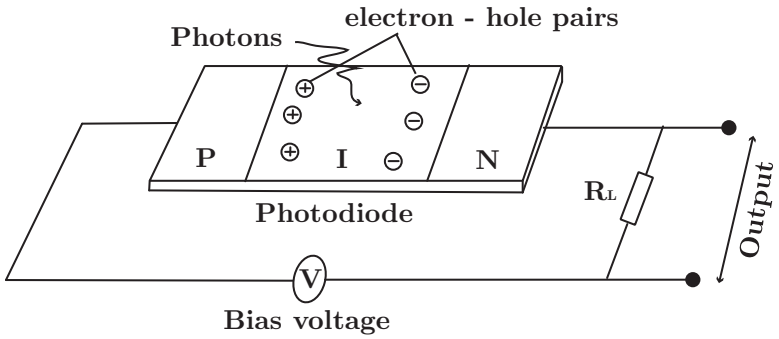

Figure 2.5 — PIN-based PD schematic.

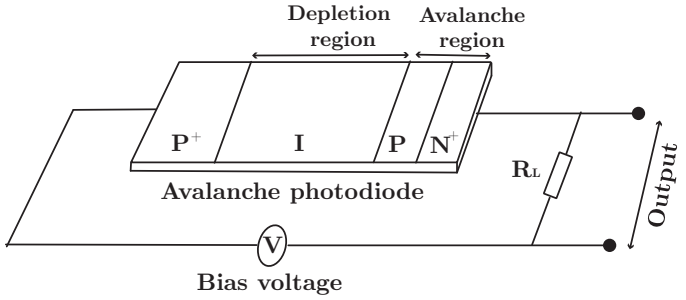

Figure 2.6 — APD-based PD schematic.

where q is the electron charge and $\mathscr{R}$ is the PD responsivity defined as the photo-current generated per unit incident optical power P_r, with λ in μm the wavelength.
For a PIN, the gain is less than unity and $\mathscr{R}$ ranges from 10 to 90 percent. They can be used for high data rates, thanks to their large modulation bandwidths that can attain tens of GHz [76]. Also, the relatively low cost and the temperature tolerance of PINs makes them suitable for use in a number of OWC systems.

2.3.1.2 APD

APDs exploit the avalanche effect to provide an inherent current gain. The avalanche effects occurs under higher electrical field regions where free carriers with enough energy generate other carriers that are also accelerated through the field and give rise to new carriers [77]. That is the repeated electron ionization process. The APD consists of a junction formed by a highly doped n-type with a p-type semiconductor that acts as a current multiplication buffer. The active region is formed by an intrinsic layer ended with a highly doped p-type region as illustrated in Fig. 2.6. The generated photo-current of an APD, compared to a PIN includes a multiplication factor given by $G = I_{\text{APD}}/I_{\text{PIN}}$, where I_{APD} and I_{PIN} denote the total output and primary un-multiplied photo-current, respectively. The APD responsivity $\mathscr{R}_{\text{APD}}$ is defined as:

$$\mathscr{R}_{\text{APD}} = \frac{\eta_{qe}\, q\, \lambda\, G}{h\, c}. \tag{2.8}$$

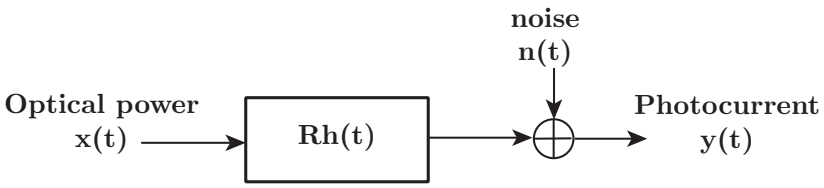

Figure 2.7 — System model of an optical system.

Typical APD gains range from 50 to 300 [76], hence, APD offers a higher sensitivity than PIN and potentially a faster response. However, the statistical nature of the avalanche process generates an associated multiplication noise with the APD, called also shot noise [77]. Note that, the avalanche process is highly temperature dependent. Also, the reverse voltage for the case of APD is much higher than PIN, typically ranging from 50 to 100V [76].

2.4 Channel

The understanding of the channel characteristics is essential to the design and implementation of OWC systems. The channel can be represented by its CIR, accounting for signal propagation through the medium. Two main propagation configurations can be considered, namely the LOS and non line-of-sight (NLOS), i.e., diffuse propagation. For the LOS configuration, the channel is characterized mainly by the Tx beam characteristics and the Rx FOV. The NLOS depends on the reflection characteristics of the object surfaces within the propagation medium. This multipath propagation can induce signal fading and ISI. Note that small scale fading effect is mostly negligible in OWC systems [97, 98]. Figure 2.7 illustrates the system model of an OWC system, where $\mathscr{R}$ is the PD responsivity, $h(t)$ is the CIR, and $n(t)$ is the additive white Gaussian noise (AWGN). The received signal $y(t)$ is given by:

$$y(t) = \mathscr{R}\, x(t) \circledast h(t) + n(t), \tag{2.9}$$

where $x(t)$ is the transmitted optical power and $\circledast$ denotes the convolution operator.
The electrical signal-to-noise ratio (SNR) is then expressed for an OOK-based link by [77]:

$$\text{SNR} = \frac{\mathscr{R}^2\, H_0^2\, P_r^2}{R_b\, N_0}, \tag{2.10}$$

where H_0 is the channel DC gain, given by $H_0 = \int_{-\infty}^{\infty} h(t)\,dt$. Also, P_r is the received optical power, N_0 denotes the noise PSD, and R_b is the system data-rate.
Equation (2.10) shows that the SNR is a function of the square of the received optical power, in

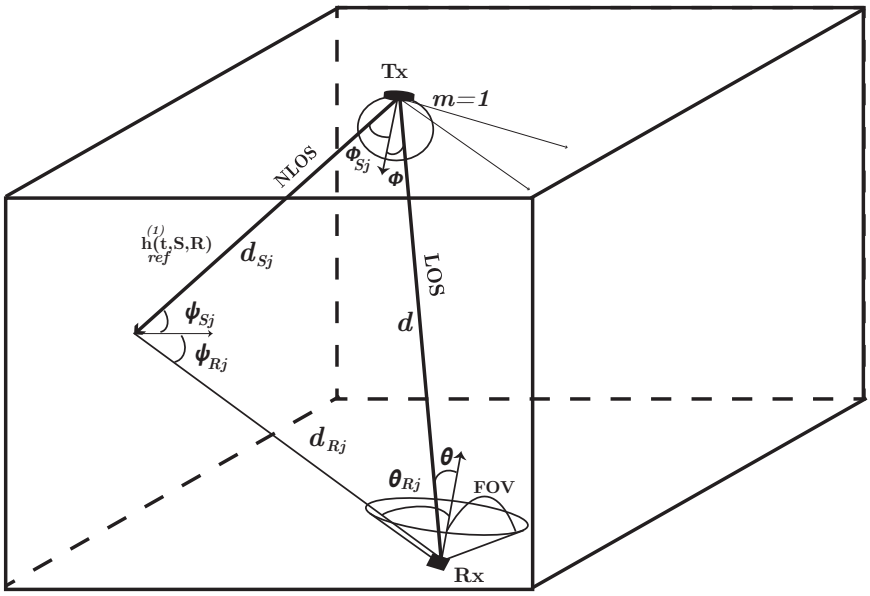

Figure 2.8 — LOS and NLOS Contribution links of OWC systems.

contrast to RF systems, where the SNR is a function of the received power. This means that higher power is required for OWC systems to achieve a given electrical SNR.
As we mentioned previously, the optical channel can be described as the contribution of LOS and NLOS links with the frequency response expressed as:

$$H_0 = H_{\text{LOS}} + H_{\text{NLOS}}. \tag{2.11}$$

We describe briefly these two contributions in the following.

2.4.1 LOS

For a Lambertian source with a radiation order m and a detector with a FOV θ_{FOV} and an active area A_{PD}, H_{LOS} can be described as [99, 100]:

$$H_{\text{LOS}} = \begin{cases} \frac{A_{\text{PD}}\,(m+1)}{2\pi d^2} \cos^m(\phi) \cos(\theta) & 0 \le \theta \le \theta_{\text{FOV}} \\ 0 \text{ Otherwise.} & \end{cases} \tag{2.12}$$

where d is the distance between the Tx and Rx, ϕ is the radiation angle, and θ is the incident angle at the Rx as shown in Fig. 2.8.
For indoor short links, attenuation due to beam propagation can be low compared to the attenuation resulting from link misalignment. When the Tx beam is highly directive (i.e., $m \gg 1$) and the FOV is very small, H_0 is maximized, but, the link is susceptible to misalignment and beam blockage. In the absence of Tx-Rx tracking to deal with mobility, the Tx and Rx should have a wide angles, which helps reduce the effects of shadowing and beam blockage. However, the signal will experience much attenuation.

2.4.2 NLOS

The NLOS contribution corresponds to the ensemble of reflective paths inside the propagation medium. These reflective paths undergo several bounces with different path lengths before reaching the Rx, broadening the CIR and hence affecting the frequency response of the channel, resulting ultimately to induced ISI. At the same time, a NLOS link is less sensitive to shadowing and beam blockage. Figure 2.8 illustrates a NLOS configuration where the rays launched from the Tx undergo several reflections before arriving at the Rx. Let us consider the contribution of the first reflection. It is given as follows [99, 100]:

$$h_{\text{ref}}^{(1)}(t,S,R) = \begin{cases} \sum_{j=1}^{K} \frac{A_{\text{PD}}(m+1)}{2\pi d_{Rj}^2 d_{Sj}^2} \rho_j \Delta A_{\text{ref}} \cos^m(\phi_{Sj}) \cos(\psi_{Sj}) \cos(\psi_{Rj}) \cos(\theta) \delta\left(t - \frac{d_{Sj}+d_{Rj}}{c}\right) & 0 \le \theta \le \theta_{\text{FOV}} \\ 0 & \text{Otherwise} \end{cases} \tag{2.13}$$

where K is the number of reflecting elements of the room, ρ_j is the reflactance of the reflective area, ΔA_{ref} is the surface of the reflective area, ψ_{Sj} is the incident angle of irradiance to the reflective area, ψ_{Rj} is the reflection angle from the reflective area, and c is the speed of light. Also, d_{Sj} and d_{Rj} are the distances from the Tx to the reflective area and from the reflective area to the Rx, respectively.

Note the complex nature of the NLOS contribution, where it depends on several factors such as the reflectance of the materials consisting the environment, the geometrical aspects of the propagation medium, and the position of the Tx and Rx.

For the k^{th}-bounce reflection, it can be calculated iteratively following the model of Barry as follows [100, 101]:

$$h_{\text{ref}}^{(k)}(t,S,R) = \frac{A_{\text{PD}} \Delta A_{\text{ref}}(m+1)}{2\pi} \sum_{j=1}^{K} \rho_j \cos^m(\phi_{Sj}) \frac{\cos(\psi_{Sj})}{d_{Sj}^2} \text{rect}\left(\frac{2\phi_{Sj}}{\pi}\right) h_{\text{ref}}^{(k-1)}\left(t - \frac{d_{Sj}}{c}, S, R\right). \tag{2.14}$$

Finally, the total NLOS CIR is given as the sum of all the reflective components as:

$$h_{\text{NLOS}}(t,S,R) = \sum_{k=0}^{\infty} h_{\text{ref}}^{(k)}(t,S,R). \tag{2.15}$$

2.5 Noise sources

OWC systems are subject to various noise sources that impact their performance. The main noise sources are the thermal noise, ambient light or background noise, the shot noise, and the dark noise. This section will briefly introduce each of these noise sources.

2.5.1 Thermal noise

Thermal noise, describes the charge carriers' movements at a certain temperature and depends strongly on the kind of circuitry used at the Rx. It is mainly caused by the TIA load resistor R_{load}

and the PD shunt resistor R_{shunt}, and is modeled as a signal independent AWGN of variance σ^2_{th} [102].

$$\sigma^2_{\text{th}} = \frac{4\,K_b\,T\,B}{R_{\text{load}}} + \frac{4\,K_b\,T\,B}{R_{\text{shunt}}}, \tag{2.16}$$

where B is the Rx bandwidth, K_b is the Boltzmann constant, and T is the absolute temperature. Note that R_{shunt} is generally very large compared to R_{load} and hence its term is usually neglected.

2.5.2 Background noise

Background noise is caused by the random fluctuations of the current generated by the natural and artificial ambient light. It is modeled as an AWGN with variance σ^2_{b} and given by [102, 103]:

$$\sigma^2_{\text{b}} = 2\,e^2\,G\,F\,B\left(\frac{\eta_{qe}}{h\,\nu}\,P_s\right) = 2\,e\,G\,F\,I_b\,B, \tag{2.17}$$

where G and F are the PD gain and excess noise factor, respectively (equal both to 1 for a PIN). Also, P_b is the ambient light power, and I_b is the generated ambient light photo-current or the background current.

2.5.3 Dark noise

Dark noise is caused by the random fluctuations of the leakage surface and bulk current, which is generated by the reverse voltage applied across the PD. The dark noise is modeled as an AWGN with variance σ^2_{dark} and given by:

$$\sigma^2_{\text{dark}} = 2\,e\,(I_{ds} + G^2\,F\,I_{db})\,B, \tag{2.18}$$

where I_{ds} and I_{db} are the diode surface and the bulk leakage currents, respectively. Note that the dark current $I_d = I_{ds} + G^2\,F\,I_{db}$ values range from 1 to 500 nA for a PIN-based Rx and is generally neglected, compared to the other noise sources.

2.5.4 Shot noise

Shot noise is caused by the quantum noise effect which manifests itself through random fluctuations of the current generated by the collected photons and flowing through the device. It is also modeled as signal dependent AWGN with variance σ^2_{shot}:

$$\sigma^2_{\text{shot}} = 2\,e^2\,G\,F\,B\left(\frac{\eta_{qe}}{h\,\nu}\,P_s\right) = 2\,e\,G\,F\,I_s\,B, \tag{2.19}$$

where P_s is the signal optical power, and I_s is the generated signal photo-current.

2.6 Channel Characterization and Modeling

Accurate characterization and modeling of the optical channel is a prerequisite to the design of efficient transmission techniques ensuring the requirements of medical WBAN systems. Extensive work has been done so far on wireless optical channel modeling and several methods have been proposed to calculate the optical CIR mainly for the case of a static indoor channel [97, 101]. The pioneering works were these of [100, 104, 105], which are based on a time-domain ray-tracing approach. Some other works such as [106–108] used a MCRT based approach with the advantage of faster computation. Reduced computational time can also be achieved by switching to the frequency domain by estimating the channel transfer function [109]. The accuracy of these algorithms was verified experimentally using IR sources, e.g., in [110, 111].

An important point is to model time-varying channels, whose their dynamics can be taken into account by adding a mobility model to the previous methods. For instance, a statistical modeling approach was proposed in [112, 113], based on a large set of CIRs generated through simulations. Meanwhile, it was shown that the LOS channel gain follows a modified Gamma distribution, whereas the channel gain including LOS and diffuse components follows a modified Rayleigh distribution [113]. In [114], the effect of shadowing on a VLC system using multiple LEDs was investigated. An algorithm accounting for the human body shadowing effect was also proposed in [115]. Also, [116] investigated via simulations and experimentally an indoor VLC channel considering random movements of people, concluding a Rayleigh distribution for the channel gain. A distance-dependent VLC path loss model was presented in [117] for a user moving along different trajectories in a furnished indoor environment. Lastly, [118] studied the influence of random device orientations on the statistics of the received SNR for a mobile user.

A few studies have considered channel characterization for optical WBANs in the IR band such as the work in [19], which was based on MCRT simulations using a dedicated software, called RapSor [119]. On the other hand, channel characterization for extra-WBAN links was considered in [38, 120–122], where user mobility was considered based on uniformly distributed random user positions and orientations of the sources/detectors. The patient's body was modeled by a simple rectangular surface in [120, 121], and by a combination of three rectangular volumes in [122], whereas a static three-dimensional (3D) model was used in [38].

Notice that channel modeling for RF-based WBANs is a rather well-explored topic. For instance, in [123–125], an avatar derived from an animation software was used to characterize the intra-WBAN channels for different scenarios including walking, running, and getting up from a chair. A similar approach was adopted in [126] to study a dynamic soldier-to-soldier communication scenario. Another approach considered a mobility model based on motion capture (MoCap) data to study the extra-WBAN channel [127, 128]. Analytical models were also proposed to describe body postures and movements, as well as node mobility patterns, such as in [129, 130].

2.7 Chapter summary

In this chapter, a general overview of OWC technology was presented. We discussed the main building blocks of an OWC transmission system, where the fundamentals of the Tx, the optical channel, and the Rx were described. In particular, we discussed the main types of optical sources available as well as modulation techniques adapted to OWC. Similarly, we discussed the main types of PDs available and enumerated the main noise sources that impacts their performance. Also, we detailed the main characteristics of optical indoor channels and provided an analytical model to characterize it.

As we mentioned in Section 2.4, the complexity of these models become significant when considering complex environments. In the next chapter, we will propose a more efficient approach for realistic simulation of OWC channels based on MCRT and will apply this to the case of WBAN systems. The proposed methodology calculates the CIR while taking into account complex 3D environments and user mobility.

Chapter 3

WBAN Channel Modeling and Link Performance

Contents

3.1 Introduction 35

3.2 Modeling of dynamic channel 36

3.2.1 Potential Equation 36

3.2.2 RWP Mobility Model 38

3.2.3 Channel Characterization 39

3.2.4 Simulation validation 40

3.2.5 Statistical Channel Modeling 41

3.3 Numerical Simulation of intra-WBAN links 42

3.3.1 Simulation Methodology 42

3.3.2 Sensor Placement 43

3.3.3 User Mobility Modeling 45

3.3.4 Link Performance Analysis 47

3.4 Chapter summary 48

3.1 Introduction

As indicated in Chapter 2, MCRT-based simulations can provide an accurate characterization for complex channels. In this chapter, a complete channel modeling approach and performance analysis of dynamic channels is presented for WBAN links. For this, we firstly introduce in Section 3.2 the method to characterize dynamic channels by introducing the potential equation and how it is used to derive the channel parameters. Then we present the RWP mobility model and explain the first- and second-order statistics that are used for channel characterization. Then, we focus

on the special case of WBAN in Section 3.3, and present the 3D human body model and how to place the SN-CN on it. We present also the local and global mobility models used in our approach. Furthermore, the link performance analysis approach is described. Lastly, the chapter summary is provided in Section 3.4.

3.2 Modeling of dynamic channel

This section presents the basic theoretical concepts behind our approach for dynamic optical channel modeling. These concern the potential equation and its relation to CIR, and the RWP mobility model. Although, as we will explain later, we use the Opticstudio software for channel characterization, it is quite useful to relate the theoretical concepts to the software parameters and outputs for a better understanding of the method used.

3.2.1 Potential Equation

The potential equation is a recursive relation that expresses the potential of a surface to illuminate a virtual Rx. For a surface located at a given position x_S, its potential $W(x_S,\vec{\omega}_S)$ to illuminate a Rx at x_R along the direction $\vec{\omega}_S$ after reflection on a surface at position y (see Fig. 3.1(a)) is given by [131]:

$$W(x_S,\vec{\omega_S}) = g(x_S,\vec{\omega}_S) + \int_{\vec{\Omega}_y} f_y(\vec{\omega_y},\vec{\omega}_S)\, W(y,\vec{\omega}_y)\cos\theta_y \,\mathrm{d}\vec{\omega}_y, \tag{3.1}$$

where θ_y is the angle between the surface normal at y and the outgoing direction $\vec{\omega}_y$, and $g(x_S,\vec{\omega}_S)$ is a visibility function which equals 0 if the path from x_S to x_R is obstructed, and 1 otherwise. In fact, $g(x_S,\vec{\omega}_S)$ here indicates the LOS path, whereas the integral term describes the reflective paths. Also, $f_y(\vec{\omega}_y,\vec{\omega}_S)$ is the bi-directional reflection distribution function (BRDF) at point y. The total power P_e emitted by the source located at x_S can be written as:

$$P_e = \iint_{A_S\Omega_S} L_e(x_S,\vec{\omega}_S)\cos\theta_S \,\mathrm{d}\vec{\omega}_S \,\mathrm{d}A_S, \tag{3.2}$$

where A_S is the surface of the source and Ω_S is the upper half hemisphere centered around the point x_S. Also, $L_e(x_S,\vec{\omega}_S)$ is the radiance leaving x_S in the direction $\vec{\omega}_s$, expressed in $\mathrm{W\,m^{-2}\,sr^{-1}}$, and θ_S is the angle between $\vec{\omega}_S$ and the surface normal to x_S, see Fig. 3.1(a). The corresponding received power P_r at x_R is related to the potential at x_S as follows [132]:

$$P_r = \iint_{A_S\Omega_S} L_e(x_S,\vec{\omega}_S)\, W(x_S,\vec{\omega}_S)\cos\theta_S \,\mathrm{d}\omega_S \,\mathrm{d}A_S. \tag{3.3}$$

For the LOS contribution, as illustrated in Fig. 3.1(b), the potential $W(x_S,\vec{\omega}_S)$ equals 1. We assume that the detector surface A_R and the source surface A_S are negligible compared to the distance d between x_S and x_R. Also, denoting by θ_R the angle between $\vec{\omega}_S$ and the normal vector of the

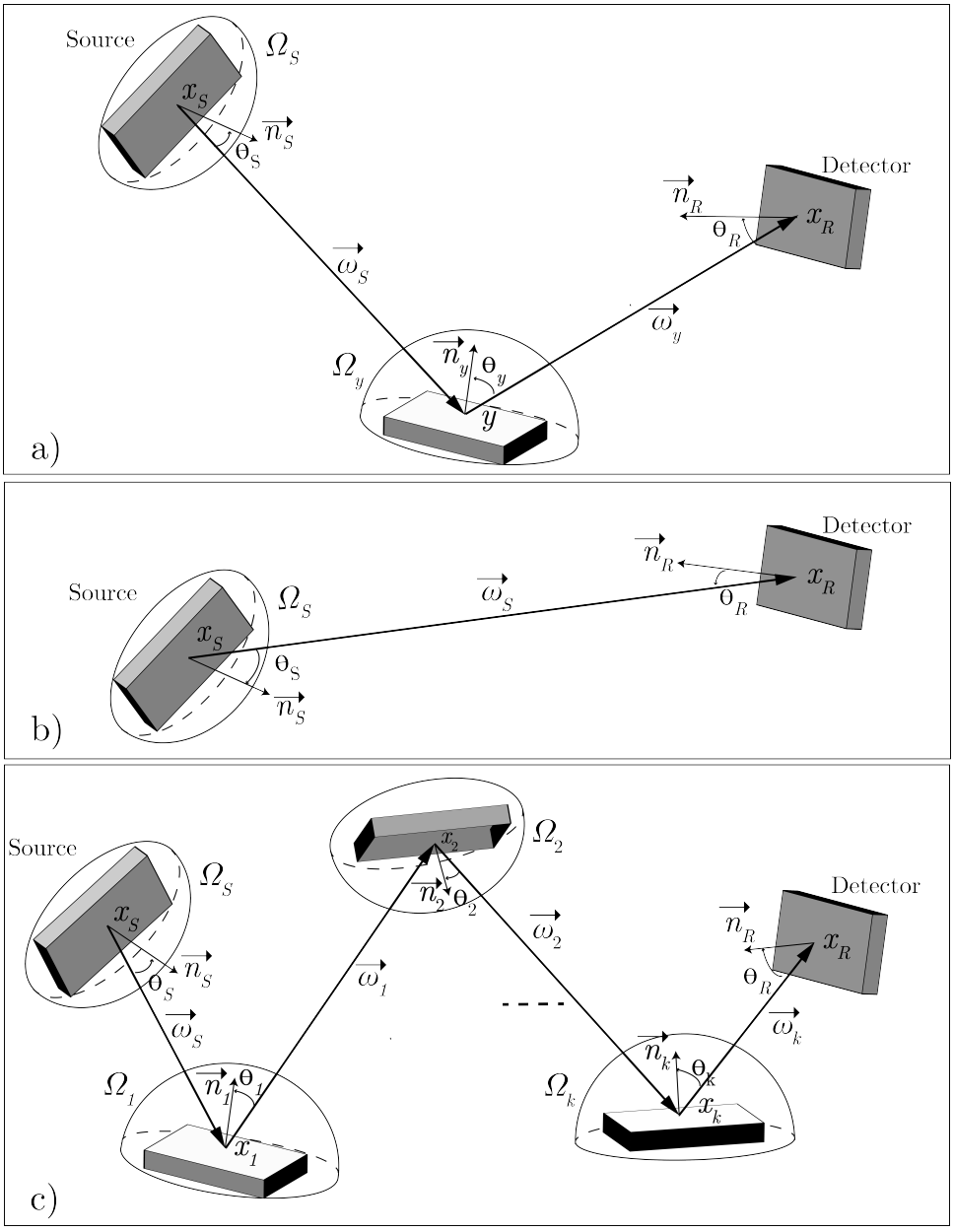

Figure 3.1 — Illustration of potential function: a) single reflection case, b) LOS case, c) multiple reflection case.

detector $\vec{n}_R$, we have $\mathrm{d}\omega_S \approx \cos\theta_R\, A_R / d^2$. Then, from (3.3), the received power from the LOS is (see Fig. 3.1(b)):

$$P_r^{(0)} = R_e(\vec{\omega}_S)\,\frac{\cos\theta_S \cos\theta_R}{d^2}\,A_R, \tag{3.4}$$

where the superscript $.^{(0)}$ stands for the zero-reflection path, i.e., the LOS. Also, $R_e(\vec{\omega}_S)$ is the radiant intensity of the source expressed in $\mathrm{W\,sr^{-1}}$. For a contribution that undergoes k reflections before arriving at the Rx, see Fig. 3.1(c), the corresponding received power $P_r^{(k)}$ can be written using (3.1) and (3.3) in recursive form as follows:

$$P_r^{(k)} = \iint\limits_{A_S\Omega_S}\int\limits_{\Omega_1}\cdots\int\limits_{\Omega_k} G_k(\boldsymbol{x},\vec{\boldsymbol{\omega}})\,\mathrm{d}\omega_k \ldots \mathrm{d}\omega_1\,\mathrm{d}\omega_S\,\mathrm{d}A_S, \tag{3.5}$$

where Ω_j denotes the hemisphere around the reflection surface x_j. Also,

$$G_k(\boldsymbol{x},\vec{\boldsymbol{\omega}}) = L_e(x_S,\vec{\omega}_S)\cos\theta_S\,A_R\,\frac{\cos(\theta_R)}{d_k^2} \times \prod_{j=1}^{k} f_{x_j}(\vec{\omega}_{j-1},\vec{\omega}_j)\cos\theta_{x_j}, \tag{3.6}$$

where $\boldsymbol{x}$ and $\vec{\boldsymbol{\omega}}$ denote the sets of the intersection points $x_S, x_1, \ldots, x_k$ and directions $\vec{\omega}_S, \vec{\omega}_1, \ldots, \vec{\omega}_k$, respectively. Here, d_k is the distance between the Rx and the last intersection point x_k, and $f_{x_j}(\vec{\omega}_{j-1},\vec{\omega}_j)$ is the BRDF at x_j.

Equation (3.5) can be solved by deterministic [100] or non-deterministic approaches such as Monte Carlo integration methods [107]. Denoting the estimated received power by $\hat{P}_r$, the basic Monte Carlo method for solving (3.5) consists of taking N_{rays} samples from the hemisphere around x_S and taking the average. For a given sample i, we denote by $\boldsymbol{x}_i$ and $\vec{\boldsymbol{\omega}}_i$ the sets of intersection points $x_{iS}, x_{i1}, \ldots, x_{ik}$ and directions $\vec{\omega}_{iS}, \vec{\omega}_{i1}, \ldots, \vec{\omega}_{ik}$, with the occurrence probability $p(\boldsymbol{x_i},\vec{\boldsymbol{\omega}}_i) = \prod_{j=1}^{k} p(x_{ij},\vec{\omega}_{ij})$. We have:

$$\hat{P}_r = \frac{1}{N_{\text{rays}}}\sum_{i=1}^{N_{\text{rays}}}\frac{G_k(\boldsymbol{x_i},\vec{\boldsymbol{\omega}}_i)}{p(\boldsymbol{x_i},\vec{\boldsymbol{\omega}}_i)}, \tag{3.7}$$

where the term in the summation corresponds to the power of the i^{th} sample, that we denote by $P_{r,i}$.

3.2.2 RWP Mobility Model

By the RWP model, a mobile node chooses a random destination point P_m within the movement area $\mathscr{A}$ according to a uniform distribution, and moves toward it with a constant speed v_m (chosen randomly from an interval $[v_{\min}, v_{\max}]$), see Fig. 3.2. After reaching P_m, it stops for a random pause time before choosing a new destination point P_{m+1} and moves toward it with a new speed v_{m+1}. These steps are repeated until the simulation time is reached. For instance, an n-step walking process can be described by the couplets $\{(P_0, v_0), (P_1, v_1), \ldots, (P_n, v_n)\}$. Note that, for simplicity, in this work, we do not consider any pause time for the mobile node.[1] This way, the RWP model

[1] The reason is to simplify the "synchronization" of the local and global mobility models, as will be described later in Subsection 3.3.3.

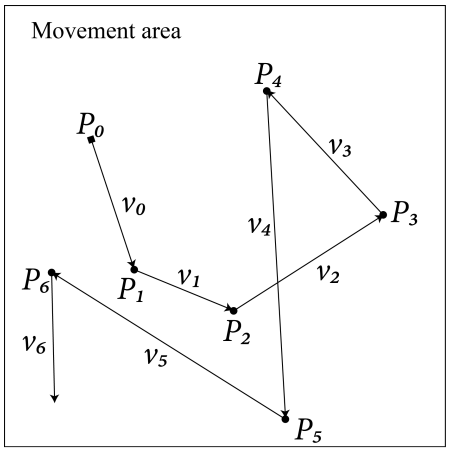

Figure 3.2 — Illustration of the RWP mobility model for a node initially located at P_0.

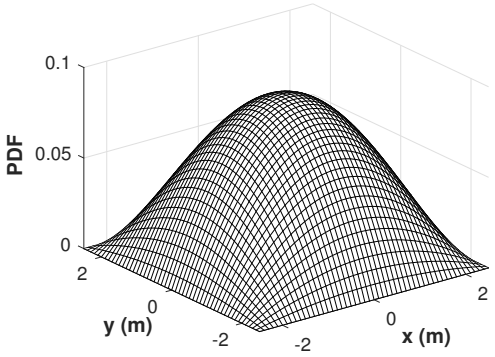

Figure 3.3 — Spatial node distribution according to RWP in a rectangular area of size (5 m × 5 m).

becomes similar to the random walk model. Denoting by x and y the Cartesian coordinates of a given position, the spatial distribution $f_{XY}(x,y)$ of positions in a rectangular area of size $a \times a$ can be approximated by [133] :

$$f_{XY}(x,y) \approx \frac{36}{a^6}\left(x^2 - \frac{a^2}{4}\right)\left(y^2 - \frac{a^2}{4}\right). \tag{3.8}$$

This distribution for the case of a rectangular room of dimension (5m×5m) is shown in Fig. 3.3. We note that the positions near to the room center have a higher probability than those at the corners, which is rather realistic for the movement of a person inside a room.

3.2.3 Channel Characterization

In this work, we use the non-sequential ray-tracing feature of Opticstudio from Zemax [134], which is a licensed optical design software for MCRT simulations. The advantage of Opticstudio is its ability to model complex 3D environments [135]. The ray-tracing output consists of a detailed

Table 3.1 — Simulation parameters for configuration A of [100].

Source	m	1
	Position (x,y,z) m	$2.5 \times 2.5 \times 3$
	Orientation (elevation,azimuth)	$(-90°,0°)$
Receiver	FOV	85°
	Area	$1\,\text{cm}^2$
	Position (x,y,z) m	$0.5 \times 1.0 \times 0$
	Orientation (elevation,azimuth)	$(90°,0°)$
Room	Dimensions	$(5 \times 5 \times 3)\,\text{m}^3$
	Wall Reflectivity	0.80
	Floor Reflectivity	0.30
	Ceiling Reflectivity	0.80

database file of the generated rays, including their power and optical path length after each reflection. The CIR, $h(t)$, can then be estimated as follows.

$$h(t) = \frac{1}{N_{\text{rays}}} \sum_{i=1}^{N_{\text{rays}}} P_{r,i}\, \delta\big(t - \frac{d_i}{c}\big), \tag{3.9}$$

where c is the speed of light and d_i is the total distance that the i^{th} ray has traveled before reaching the detector. We use several metrics to analyze the obtained simulation results, including the channel DC gain and delay spread. The DC gain H_0 is defined as [99]:

$$H_0 = \int_0^{\infty} h(t)\,\mathrm{d}t. \tag{3.10}$$

Also, the root mean squared (RMS) delay spread τ_0 of the channel is defined by [76]:

$$\tau_0 = \sqrt{\frac{\int_0^{\infty} (t-\tau)^2\, h^2(t)\,\mathrm{d}t}{\int_0^{\infty} h^2(t)\,\mathrm{d}t}}, \tag{3.11}$$

where τ is mean excess delay, given by:

$$\tau = \frac{\int_0^{\infty} t\, h^2(t)\,\mathrm{d}t}{\int_0^{\infty} h^2(t)\,\mathrm{d}t}. \tag{3.12}$$

3.2.4 Simulation validation

We propose to validate the proposed simulation against reference results from the literature. Here, we consider the configuration A from [100], where the simulation parameters are described in Table 3.1. The number of simulation rays considered for the MCRT is $N_{\text{rays}} = 10^9$. Figure 3.4 shows the calculated CIR using Opticstudio, along with the CIR from [100]. As can be seen, the simulated CIR approaches the reference CIR, with a needed simulation time much smaller, which validates our simulation methodology. Note that, as the number of simulation rays increases, the accuracy gets improved, at the cost of increased simulation time.

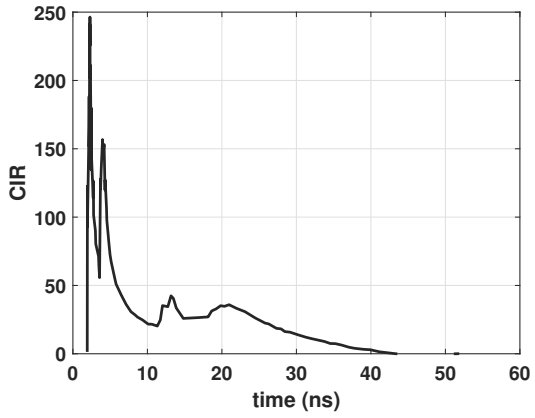

(a)

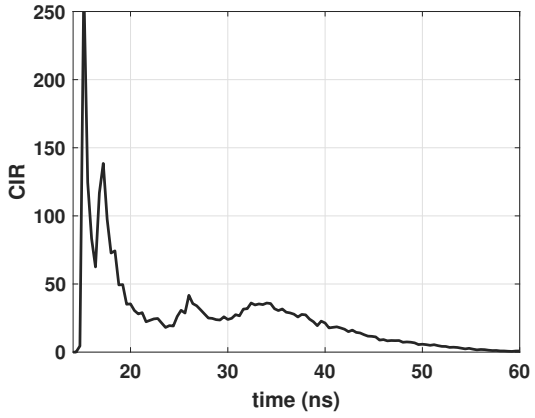

(b)

Figure 3.4 — The simulated CIR for configuration A of [100]. (a) reference CIR and (b) simulated CIR using Opticstudio.

3.2.5 Statistical Channel Modeling

For the case of dynamic WBAN channels, we will consider their statistical modeling by fitting the histogram of the channel gains to a given probability density function (PDF) such as Rayleigh, lognormal, Weibull, Nakagami, etc. To find the best fit model, we use the Akaike information criterion (AIC), defined as [136]:

$$\mathrm{AIC} = -\log\big(L(\boldsymbol{\Theta}|\boldsymbol{x})\big) + 2p + \frac{2p\,(p+1)}{(N_{\mathrm{p}} - p - 1)}, \tag{3.13}$$

where $\log(L(\boldsymbol{\Theta}|\boldsymbol{x}))$ is the log-likelihood of the estimated model parameters $\boldsymbol{\Theta}$ of size p, conditioned on the data samples $\boldsymbol{x}$ of size N_{p}. The model corresponding to the minimum AIC value provides the best fit to the data.

To characterize channel time variations, we also consider the channel coherence time that is approximated by the time for which the autocorrelation function (ACF) falls below a certain value, e.g., 0.5 [76].

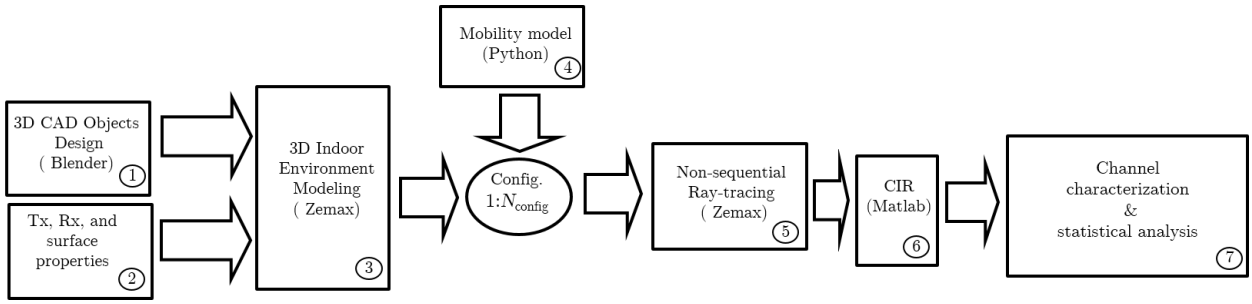

Figure 3.5 — Adopted simulation methodology.

We generate a random trajectory based on the modified RWP and calculate the corresponding H_0 for each point. This results in N_{config} realizations of H_0 for each link, based on which we propose a statistical model for H_0 based on non-parametric KDE method. This avoids us to do time-consuming MCRT simulations for calculating P_{out}. For a given set of N realizations x_j of a random variable x with a PDF $f_X(x)$, the KDE estimate of the PDF is given by [137]:

$$\hat{f}_X(x) = \frac{1}{N\delta} \sum_{j=1}^{N} \mathscr{K}\left(\frac{x - x_j}{\delta}\right), \tag{3.14}$$

where $\mathscr{K}$ is the kernel, considered here to be Gaussian, and δ is the smoothing parameter, calculated from $\delta = 1.06\,\hat{\sigma}\,N^{-1/5}$, where $\hat{\sigma}$ is the estimated standard deviation of $\log(x)$ [138].

3.3 Numerical Simulation of intra-WBAN links

3.3.1 Simulation Methodology

The block diagram of our simulation methodology is given in Fig. 3.5. The first step consists in building the 3D scene inside the Opticstudio simulator. The 3D objects are either created from built-in objects or imported using a 3D computer-aided design (CAD) software such as Blender [139] (Block ① in Fig. 3.5). We then define the reflective properties of these objects (e.g., the BRDF of the different surfaces), as well as the properties of the sources and detectors, i.e., Tx radiation pattern, detectors FOV, detector area, etc. (Block ②). By adding up these 3D objects, we construct the environment and its constituent reflectors (Block ③). The next step is to include the mobility model (Block ④). We use a Python script to load a set of N_{config} configurations describing objects' movements and orientations during the consecutive snapshots of a mobility scenario. Once the configuration is loaded, the script runs the non-sequential ray-tracing tool from Opticstudio (Block ⑤) that will be used to estimate the CIR for the given configuration, as explained in Subsection 3.2.1. Afterward, based on the calculated CIRs, e.g. using Matlab® (Block ⑥), we analyze different channel metrics and their statistics (Block ⑦).

3.3.2 Sensor Placement

We consider a set of 10 SNs on the patient's body, as shown in Fig. 3.6(a). The sensor positions correspond to the most likely placements for potential applications such as EEG (SN1 and SN2), ECG (SN3, SN4, and SN6), insulin pump (SN8), etc. To study the effect of CN placement, we consider two potential positions as suggested in [19, 122], i.e., on the shoulder and the hip, denoted by CN1 and CN2, respectively. Considering these two different CN locations provides sufficient insight on the channel statistics for different potential SNs. Note that, the selected location for the CN impacts the reliability of the links between the CN and SNs for the intra-WBAN links, as well as that of the link between the CN and the AP for the extra-WBAN link (given that the AP is likely placed on the room ceiling or wall). For CN1, the links are less sensitive to shadowing from body parts than for CN2, where they can be impacted by the arms of the user. Also, since CN2 is around the center of the network, there is less difference in its distance to the SNs, compared to CN1.

We model the human body by a 3D standard tessellation language (STL) mesh object [140], which is a widely used file format in CAD tools to describe surfaces of a 3D object. It consists of a set of vertices, edges, and faces to define the shape of the object. Vertices are defined by their corresponding 3D coordinates and faces by the vertices that delimit them, as well as by their normal vector $\vec{n}_{\text{face}}$. We represent the patient's body by a set of 902 vertices, connected into 1800 triangular faces, as shown in Fig. 3.6(a), allowing sufficient precision for the simulations. We then place each SN on a triangular face, where its position and orientation are defined by the face center coordinates and its normal vector $\vec{n}_{\text{face}}$, respectively. To direct the node, initially oriented along $\vec{z}$, towards the face's normal vector $\vec{n}_{\text{face}} = (n_x, n_y, n_z)^T$, we apply the Davenport yaw-pitch-roll intrinsic chained rotation [141] to the reference vector $\vec{z} = (0,0,1)^T$, as illustrated in Fig. 3.6(b). The corresponding rotation matrix, taking into account roll, pitch, and yaw rotations around $\vec{x}$, $\vec{y}$, and $\vec{z}$, respectively, can be expressed as:

$$\boldsymbol{R} = \boldsymbol{R}_x(\phi)\,\boldsymbol{R}_y(\theta)\,\boldsymbol{R}_z(0) = \begin{pmatrix} \cos\theta & 0 & \sin\theta \\ \sin\phi\sin\theta & \cos\phi\cos\theta & -\sin\phi\cos\theta \\ -\cos\phi\sin\theta & \sin\phi & \cos\phi\cos\theta \end{pmatrix}. \tag{3.15}$$

Here, ϕ and θ denote the roll and pitch angles, respectively. We have set the yaw angle to zero because such rotations are included in the rotations of the corresponding faces. In fact, as shown in Fig. 3.6, the orientations of the nodes, and hence the vectors $\vec{n}_{\text{node}}$ are changed following the body's position and local mobility. Therefore, the yaw angle, which is with respect to $\vec{n}_{\text{face}}$, is set to zero without having an impact on the orientation of the node, as its corresponding rotation only tilts the node around $\vec{z}$ in the xy plane of the face. The orientation of the node is hence obtained from $\vec{n}_{\text{node}} = \vec{n}_{\text{face}} = \boldsymbol{R}\vec{z}$ and (3.15):

$$\begin{aligned} \phi &= \text{atan2}(-n_y, n_z), \quad \text{with } \phi \in [-\pi, \pi], \\ \theta &= \arcsin n_x, \quad \text{with } \theta \in [-\pi/2, \pi/2], \end{aligned} \tag{3.16}$$

where atan2 stands for the two-argument arctangent [142].

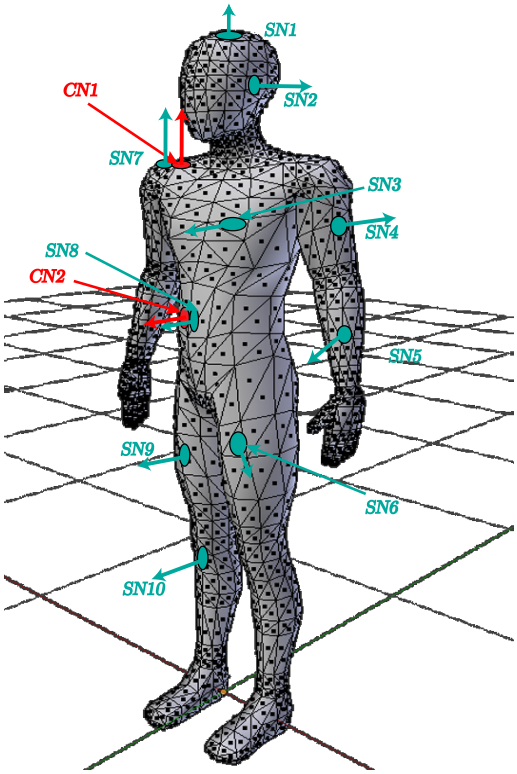

(a)

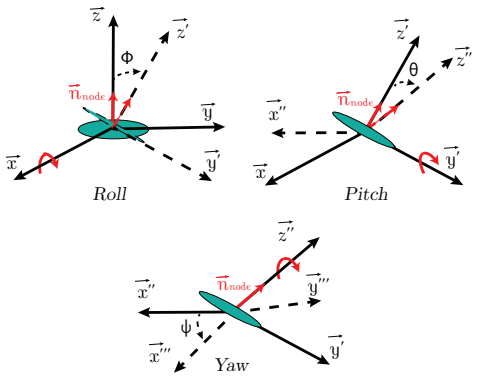

(b)

Figure 3.6 — Illustration of the STL model of the body; (a) considered placements of SNs and CNs with the corresponding $\vec{n}_{\text{node}}$ vectors; (b) xyz intrinsic rotations made to direct the node along the orientation $\vec{n}_{\text{face}}$ of the triangular face: the Cartesian coordinates after roll-pitch-yaw rotations (in order) are denoted by $xy'z'$ (after roll rotation), $x''y'z''$ (after pitch rotation), and $x'''y'''z''$ (after yaw rotation).

Table 3.2 — Sensor and coordinator node positions and orientations as considered in Fig. 3.6(a).
The last column indicates the corresponding Cartesian coordinates of the unit vectors $\vec{n}_{\text{node}}$ (after rotation).

Node	x (m)	y (m)	z (m)	$\phi(^\circ)$	$\theta(^\circ)$	$\vec{n}_{\text{node}}^{\,T}$
SN 1	0.01	−0.04	1.63	22.84	11.95	$(0.21, -0.38, 0.9)$
SN 2	0.07	−0.01	1.56	−4.88	84.74	$(1.0, 0.01, 0.09)$
SN 3	0.18	−0.04	1.24	82.73	44.32	$(0.7, -0.71, 0.09)$
SN 4	0.23	0.08	1.18	76.27	63.18	$(0.89, -0.44, 0.11)$
SN 5	0.26	0.05	0.95	80.68	33.94	$(0.56, -0.82, 0.13)$
SN 6	0.10	−0.08	0.74	89.45	11.96	$(0.21, -0.98, 0.01)$
SN 7	−0.18	−0.01	1.37	19.82	−5.91	$(-0.1, -0.34, 0.94)$
SN 8	−0.10	−0.04	1.05	87.60	−47.97	$(-0.74, -0.67, 0.03)$
SN 9	−0.10	−0.04	0.59	106.18	−25.55	$(-0.43, -0.87, -0.25)$
SN 10	−0.09	0.00	0.15	87.96	−22.89	$(-0.39, -0.92, 0.03)$
CN 1	−0.19	−0.02	1.36	24.37	−7.97	$(-0.14, , -0.41, 0.9)$
CN 2	−0.07	−0.07	1.02	87.63	−27.46	$(-0.46, -0.89, 0.04)$

Table 3.2 summarizes the SN and CN positions on the body and their corresponding rotation angles, as well as the Cartesian coordinates of the unit vector $\vec{n}_{\text{node}}$ (after rotation) for the *anatomical* position configuration (i.e., at rest position). The considered body height, width, and depth are $(1.7 \times 0.3 \times 0.2)$ m^3, which correspond to the typical body shape of an adult person.

3.3.3 User Mobility Modeling

To account for user mobility, we should consider at the same time the local mobility, which concerns body parts movements, and the global mobility, which concerns the movements of the whole body inside the room. We describe the local mobility of the body by a 3D animation of a walk cycle created (manually) using the Blender software [139]. Guidlines for creating the animation can be found in [143] The animation consists of a set of $N_{\text{f}} = 27$ frames, representing the body at different instants of the walk cycle, as illustrated in Fig. 3.7.[2] Note that as the result of this body movement, the positions and orientations (i.e., angles ϕ and θ) of the SNs will change since the body configuration is different from one frame to another. To account for these changes, we use (3.16) to calculate the new SNs' positions and orientations in each frame (based on the position and orientation of the corresponding faces on the mesh object). This way, the set of five matri-

[2]Note that here we consider the case of "normal" walking, which is reasonable for the case of medical surveillance of patients or elderly people, considered in this work. For studying specific walk scenarios with more precision, a more detailed model based on motion capture could be used.

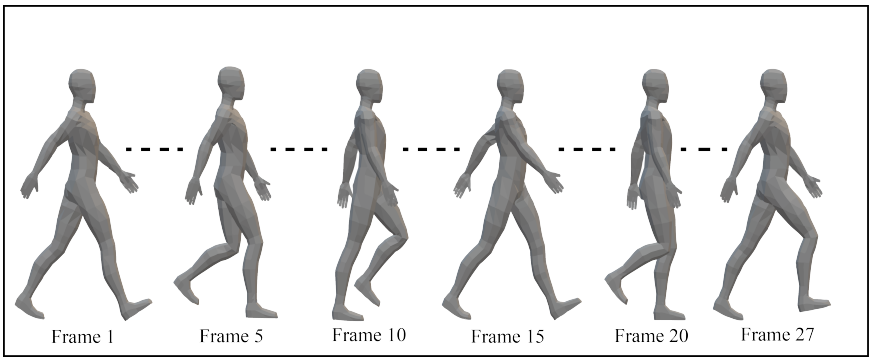

Figure 3.7 — Illustration of the local mobility during a walk cycle.

ces $\boldsymbol{X}, \boldsymbol{Y}, \boldsymbol{Z}, \phi$, and $\boldsymbol{\theta}$ of size $(N_\mathrm{f} \times 12)$ will represent nodes movements along the walk cycle (10 SNs plus 2 CNs). The minimal and maximal range of variations of ϕ and θ for each sensor and coordinator node during local mobility is presented in Appendix A.1.

As concerns the global user mobility, as discussed in Subsection 3.2.2, we use the RWP model to generate a random sequence of trajectory points $\{(P_{x_\mathrm{i}}, P_{y_\mathrm{i}}), (P_{x_{\mathrm{i}+1}}, P_{y_{\mathrm{i}+1}}), \vec{v}_\mathrm{i}\}$, with i referring to a given time instance. We then calculate the appropriate time step Δt that synchronizes the local and global mobility models. By this approach, consecutive animation frames are changed each Δt, which is calculated based on the distance d_cycle traveled by the user during a walk cycle with a velocity v_user, as follows:

$$\Delta t = \frac{1}{N_\mathrm{f}} \frac{d_\mathrm{cycle}}{v_\mathrm{user}}, \tag{3.17}$$

To determine Δt, we assume $v_\mathrm{user} = 0.45\,\mathrm{m/s}$ and $d_\mathrm{cycle} = 2\,\mathrm{m}$ as reasonable values [144, 145], and we take $N_\mathrm{f} = 27$, which has been verified to capture the movement pattern. We have $\Delta t \approx 0.17\,\mathrm{sec}$. Note that with the classical RWP model, the user moves in a straight line from one point to another, producing a sharp rotation when reaching a waypoint. To consider a more realistic model, we propose here to improve the RWP model by moving the user along a curved path rather than straight lines. For this, we interpolate over the waypoints using a 3-order polynomial. Note that the spatial node distribution with this proposed approach is close to that with the classical RWP model, shown in Fig. 3.2, yet with slightly more spreading with respect to the center of the room. Note that, referring to the general model in Subsection 3.2.2, here for the sake of simplicity, we consider a constant speed of 0.45 m/s for all user movements. However, due to 3-order polynomial interpolation over the waypoints, the actual speed varies between 0.06 and 1.36 m/s, with a mean of 0.38 m/s and a standard deviation of 0.19 m/s. The high speeds correspond to straight trajectories and low speeds are obtained near to rotation points. This will affect the degree of arms and legs swing. However, for the sake of simplicity, the motion cycle is not modified as the difference is rather negligible, given the relatively low speed (walk scenario) and relatively large coherence times, which are around a few seconds as we will see later. Overall, the interest of the proposed mobility model is the adequate description of realistic walk scenarios by favoring the positions in the vicinity of the room center and by taking into account a more smooth walk

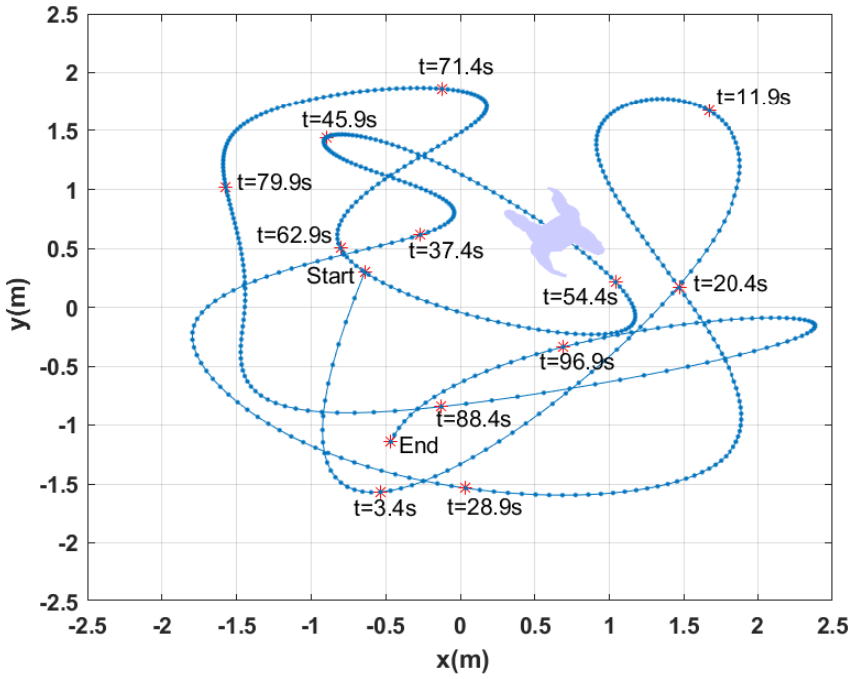

Figure 3.8 — Top view of the typical user trajectory generated with the proposed improved RWP model for $N_{\mathrm{p}} = 588$ positions.

trajectory (avoiding sharp rotations). This especially concerns the statistics of channel time variations, where by avoiding unrealistic abrupt changes in the node direction, the estimated ACF and channel coherence time (see Subsection 5.3.4) are more realistic.

The resulting model can be described by the matrix $[\boldsymbol{p}_x, \boldsymbol{p}_y, \boldsymbol{\gamma}]$, where, for instance, $\boldsymbol{p}_x$ is the vector of x coordinates $P_{x_{\mathrm{i}}}$ of the considered trajectory points, and $\boldsymbol{\gamma}$ is the vector of rotation angles γ_{i}, corresponding to the global rotation around $\vec{z}$ of the body, after the i^{th} time instance:

$$\gamma_{\mathrm{i}} = \arccos \frac{\vec{v}_{\mathrm{i}} \cdot \vec{n}_{\mathrm{body}}}{\|\vec{v}_{\mathrm{i}}\| \left\|\vec{n}_{\mathrm{body}}\right\|}, \tag{3.18}$$

where $\vec{v}_{\mathrm{i}}$ is the corresponding instantaneous velocity and $\vec{n}_{\mathrm{body}} = -\vec{y}$ is the initial vector normal to the body.

Figure 3.8 illustrates the top view of a typical trajectory inside the room, generated using our proposed method. We can see that the generated trajectory is smooth and more realistic than the classical RWP (compare with Fig. 3.2).

3.3.4 Link Performance Analysis

Using the statistical models, obtained following the steps described in the previous subsections for every SN-CN link, we randomly generated N'_{config} values for H_0, such that $N'_{\mathrm{config}} \gg N_{\mathrm{config}}$. Then, for each channel realization, we calculated the BER for an uncoded NRZ OOK-based link for given

data-rate R_b and transmit power P_t. Assuming optimal maximum likelihood detection (MLD), we have [146, 147]:

$$\text{BER} = \frac{1}{4}\text{erfc}\Big(\frac{\gamma_{\text{th}} - \alpha I_1}{\sqrt{2(\alpha\sigma_{s,1}^2 + \sigma_0^2)}}\Big) + \frac{1}{4}\text{erfc}\Big(\frac{I_1 - \gamma_{\text{th}}}{\sqrt{2(\sigma_{s,1}^2 + \sigma_0^2)}}\Big), \tag{3.19}$$

where $\text{erfc}(x) = \frac{2}{\sqrt{\pi}}\int_x^\infty \exp(-u^2)du$ is the complementary error function, $\alpha = 0.2$ is the LED extinction ratio, and γ_{th} is the optimal MLD threshold that minimizes the BER. Also, $I_1 = \mathscr{R}GP_tH_0$ is the received current for symbol '1', where $\mathscr{R} = 0.65\,\text{A/W}$, stands for the PD responsivity and G is the PD gain ($G = 1$ for PIN and we set $G = 50$ for APD). Furthermore, $\sigma_0^2 = \sigma_{\text{th}}^2 + \sigma_{\text{b}}^2$, where $\sigma_{\text{b}}^2 = 2eG^2FBI_b$ and $\sigma_{\text{th}}^2 = 4K_bT_eB/R_l$ are the variances of background and thermal noises, respectively [102]. Here, e is the electron charge, K_b is the Boltzman constant, $T_e = 298\,\text{K}$ the equivalent noise temperature, and F is the PD excess noise factor ($F = 1$ for PIN and we set $F = 3$ for APD), B denotes the Rx low-pass filter, typically approximated by $R_b/2$, and R_L the load resistor of the TIA, set to $50\,\Omega$. Also, I_b is the average photo-current generated by a PIN PD due to the background noise [98]. Lastly, $\sigma_{s,1}^2 = 2eGFBI_1$ in (3.19) is the variance of the signal shot noise. We neglect the dark current noise compared with background and thermal noises.

For the case of APD, γ_{th} is calculated as follows [146]:

$$\gamma_{\text{th,APD}} = -\frac{I_1\sigma_0^2}{\sigma_{s,1}^2} + \Big[\frac{I_1^2\sigma_0^4}{\sigma_{s,1}^4} + \frac{\alpha I_1^2\sigma_{s1}^2 + (1+\alpha)I_1^2\sigma_0^2}{\sigma_{s1}^2} + \frac{(\sigma_{s,1}^2 + \sigma_0^2)(\alpha\sigma_{s,1}^2 + \sigma_0^2)}{(\alpha-1)\sigma_{s,1}^2}\ln\Big(\frac{\alpha\sigma_{s,1}^2 + \sigma_0^2}{\sigma_{s,1}^2 + \sigma_0^2}\Big)\Big]^{0.5}. \tag{3.20}$$

In the case of using a PIN PD, given the negligible signal shot noise [102], we have

$$\gamma_{\text{th,PIN}} = \frac{(\alpha+1)I_1}{2}. \tag{3.21}$$

Finally, the outage probability is defined as the probability that the instantaneous link BER goes above a given threshold BER_{th} ($\text{P}(BER > BER_{\text{th}})$).

3.4 Chapter summary

In this chapter, we presented a channel characterization and modeling approach that considers the effects of mobility and shadowing due to the body parts as well as a realistic body movement inside an indoor environment. A dynamic model based on a 3D animation of the walk cycle was proposed to model body parts movement. We also introduced a modified RWP mobility model to generate a realistic random trajectory of a patient inside a room. The approach was first validated against reference results from the literature, confirming its good accuracy. Also, a statistical approach to characterize the channel based on best-fit and KDE estimate was presented and the BER as well as the outage probability was derived for link performance evaluation.

In the next two chapters, we will apply the approach developed here to characterize the intra- and extra-WBAN channels.

Chapter 4

Channel Modeling and Performance Analysis of Intra-WBANs

Contents

4.1 Introduction . . . 49
4.2 Environment Description and Parameter Specification . . . 50
4.3 Channel characterization . . . 50
4.3.1 Channel DC Gain . . . 52
4.3.1.1 Standing configuration . . . 52
4.3.1.2 Local mobility configuration . . . 53
4.3.1.3 Global mobility configuration . . . 53
4.3.2 Delay Spread . . . 54
4.3.3 Channel Dynamic Behavior . . . 55
4.3.3.1 **Local mobility** . . . 56
4.3.3.2 **Global mobility** . . . 57
4.3.4 Statistical Analysis of Channel Gain . . . 58
4.3.5 Channel Coherence Time . . . 59
4.4 Performance analysis . . . 60
4.4.1 Effect of PD Type and Data-Rate . . . 61
4.4.2 Comparison of Intra-WBAN Links for Low Background Noise Level . . . 62
4.4.3 Comparison of Intra-WBAN Links for Relatively High Background Noise Level . . . 64
4.5 Chapter summary . . . 65

4.1 Introduction

In Chapter 3, we proposed a channel characterization approach based on MCRT simulations that accounts for body movements and mobility inside an indoor environment.

In this chapter, we focus on channel characterization and modeling of optical intra-WBAN links, while taking into account the effects of mobility and shadowing due to the body parts as well as a realistic body movement inside an indoor environment. First, we describe the environment and specify the simulation parameters used for the intra-WBAN scenario in Section 4.2. In Section 4.3, we provide a set of simulation results to characterize the intra-WBAN optical channel, where the main channel metrics such as channel DC gain, delay spread, and coherence time are calculated. We also show the temporal evolution of the channel gain and present a best-fit statistical characterization based on AIC criterion for different SN-CN links. Then, in Section 4.4, we evaluate the outage probability performance for PIN- and APD-based Rxs using the statistical channel estimates. We also study the performance under low and high background noise conditions. Finally, the chapter summary is provided in Section 4.5.

4.2 Environment Description and Parameter Specification

We consider at each SN an IR LED at $\lambda_0 = 850\,\text{nm}$ wavelength with full width at half maximum (FWHM) of $\Delta\lambda = 30\,\text{nm}$, modeled by the typical Lambertian radiation of order $m = 1$. For CNs, we consider a PD of $1\,\text{cm}^2$ active area (considered as typical value in the related literature) without any lens, and the Rx FOV is assumed to be 60°. Since in this work we are interested in the effects of body shadowing and user mobility on the channel metrics, we consider the case of an empty room as illustrated in Fig. 4.1 of dimension $(5 \times 5 \times 3)\,\text{m}^3$, with plaster walls and ceiling, and pinewood floor. The classical Lambertian BRDF is used for the materials [97] while taking into account the wavelength dependency of their reflectivity as in [108, 148]. The body itself is assumed to be absorbent, given the low reflectivity of skin, compared to that of the walls [149]. Note that by assuming an absorbing body, we are considering the worst-case scenario where we have the maximum effect of beam shadowing. At least 3-order reflections are considered for beam propagation. Note that, although the room dimension can affect channel characteristics such as the DC gain and the delay spread, it has a negligible effect on their overall trend [113]. Also, given the typically low data-rates that are used in medical WBANs, the room furniture has a negligible impact on the main characteristics of the channel [120, 150]. At each user position, and from each SN, $N_{\text{rays}} = 2.5 \times 10^7$ rays are used for MCRT simulations with Opticstudio, insuring sufficient accuracy in the obtained CIRs. Table 4.1 summarizes the main parameters we use in our simulations.

4.3 Channel characterization

We provide here a set of simulation results to characterize the intra-WBAN IR optical channel. We consider three different cases of standing, local mobility, and global mobility configurations:

- In the standing configuration, the body is in anatomical position at the center of the room, which is the worst case for NLOS links as the distance from the reflectors is maximal. We have

Table 4.1 — Simulation parameters.

Tx (SN)	m	1
	λ_0	850 nm
	$\Delta\lambda$	30 nm
Rx (CN)	FOV	60°
	Area	1 cm^2
Room	Dimensions	$(5 \times 5 \times 3)\,m^3$
	Wall Reflectivity	0.83 (Plaster)
	Floor Reflectivity	0.87 (Pinewood)
	Ceiling Reflectivity	0.83 (Plaster)
Body	Dimensions	$(1.7 \times 0.3 \times 0.2)\,m^3$
	Reflectivity	absorbing

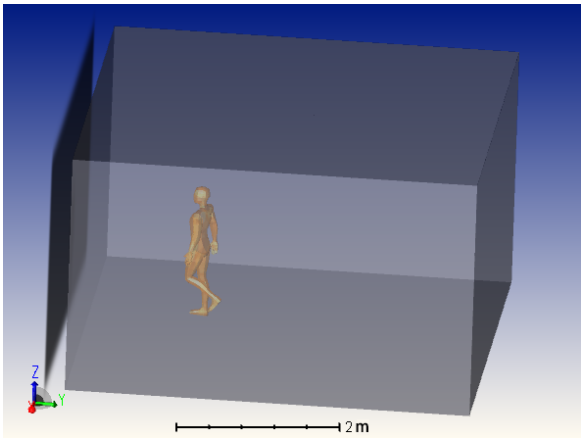

Figure 4.1 — A snapshot of the simulated random walk inside an empty room with Opticstudio.

$N_{\text{config}} = 1$.

- For the local mobility configuration, the body has a fixed position at the center of the room but moves its parts (i.e., arms, legs, etc.) following the walk cycle described in Subsection 3.3.3. Indeed, the interest in considering the local mobility case is to gain insight into the effects of body parts movement. For this case, we have $N_{\text{config}} = N_{\text{f}} = 27$.

- The global mobility case involves both the movements of the body inside the room (according to the proposed modified RWP model) and the local mobility of the body parts. Considering a simulation time of 100 sec, the total number of samples for the particular trajectory in Fig. 3.8 is $N_{\text{p}} = 588$. We have $N_{\text{config}} = N_{\text{p}}$.

The analysis of the obtained simulation data is presented in the following subsections.

Table 4.2 — Mean H_0(in dB) and Standard variation σ_0 of the channel gain for different intra-WBAN links corresponding to CN1, for the Three considered configurations.

SN	Standing	Local mobility		Global mobility	
	H_0	$\bar{H_0}$	σ_0	$\bar{H_0}$	σ_0
1	−53.45	−53.41	0.15	−52.36	0.67
2	−57.52	−57.76	0.15	−56.38	0.8
3	−56.27	−56.44	0.26	−55.3	0.81
4	−57.17	−57.83	0.35	−56.68	0.68
5	−56.32	−56.87	0.72	−55.96	0.9
6	−56.05	−56.76	0.86	−55.8	1.06
7	−53.57	−53.34	0.38	−52.01	1.36
8	−55.63	−56.27	0.66	−55.26	1.35
9	−56.22	−56.17	0.75	−55.58	1.08
10	−56.24	−56.81	0.56	−56.37	0.59

4.3.1 Channel DC Gain

First, to study the channel attenuation, we analyze the average channel gain $\bar{H_0}$ and its standard deviation σ_0 for each intra-WBAN link in the three above mentioned configurations. These results are presented in Tables 4.2 and 4.3 for the cases of CN1 and CN2, respectively.

4.3.1.1 Standing configuration

Obviously, for this configuration, we have $\bar{H_0} = H_0$ and $\sigma_0 = 0$. We can see that those SNs which have the same orientation as the CN (e.g., SN7 for CN1, and SN9 for CN2) have a higher $\bar{H_0}$ (around −53 dB) compared to the other sensors. This can be explained by the presence of a strong first-order reflection contribution and would suggest, when it is possible, directing the nodes towards the same reflection surfaces, especially for sensors that do not move considerably. We can also see that SNs that are partially blocked by the body have a lower $\bar{H_0}$, which shows the impact of body shadowing on the channel gain. This is the case for most links to CN1; for instance, $\bar{H_0} = -57.5$ and −57.1 dB for SN2 and SN4, respectively. We notice a higher $\bar{H_0}$ for SNs located on the lower part of the body for the case of CN2, with differences with respect to CN1 case on the order of 2 to 3 dB. For SN2 and SN4, we have similar results for CN1 and CN2, whereas for SN1 and SN7, $\bar{H_0}$ is about 2 dB higher for CN1. Lastly, note that the relatively low difference between the channel gains of different links can be justified by the relatively high reflectivity of walls in the case of IR transmission.

Table 4.3 — Mean H_0(in dB) and Standard variation σ_0 of the channel gain for different intra-WBAN links corresponding to CN2, for the Three considered configurations.

SN	Standing	Local mobility		Global mobility	
	H_0	$\bar{H}_0$	σ_0	$\bar{H}_0$	σ_0
1	−55.79	−55.98	0.26	−55.17	0.65
2	−58.21	−57.38	0.52	−56.27	1.06
3	−55.7	−54.76	0.45	−53.48	1.41
4	−57.02	−56.54	1.06	−55.44	1.59
5	−55.51	−55.19	0.76	−54.01	1.52
6	−54.05	−53.43	1.11	−52.24	1.5
7	−55.6	−56.77	0.21	−55.81	0.75
8	−53.72	−53.81	0.46	−52.28	1.83
9	−52.98	−53.28	0.36	−51.88	1.56
10	−53.47	−54.03	0.97	−52.86	1.58

4.3.1.2 Local mobility configuration

We observe similar behavior in $\bar{H}_0$ as in the previous case. For the case of CN2 (located on the right side of the hip) and compared to the standing configuration, we notice that, reasonably, $\bar{H}_0$ decreases for SNs located on the right side of the body, whereas it increases for SNs on the left side. For the case of CN1, we notice an increase in $\bar{H}_0$ for SN1 and SN7 and a decrease of it for the other SNs. Focusing on σ_0, we notice that it is, in general, higher for the case of CN2 compared to CN1: it ranges between 0.15 to 0.86 dB for the former case and between 0.21 to 1.11 dB for the latter case. For both CNs, the largest σ_0 values are observed for SNs placed on the legs and arms, while the lowest values are observed for SNs that are rather fixed during the local mobility (e.g., SN1 and SN7, placed on the head and the shoulder, respectively). An exception concerns SN8, which experiences periodic shadowing from the right arm, which makes its variations more important despite its relatively low mobility.

4.3.1.3 Global mobility configuration

We observe a similar trend as in the previous case with a general increase in $\bar{H}_0$ for all links on the order of 1 dB. This was expected since with the body rotations and movements, for the positions that are close to the walls, we get a higher $\bar{H}_0$. Compared to the local mobility configuration, here σ_0 increases for all SN links due to more significant mobility, ranging in 0.59 to 1.36 dB for CN1 and 0.65 to 1.83 dB for CN2, while following a similar trend as observed for the local mobility case. This shows that body position and orientation inside the room have a large impact on the variations of

Table 4.4 — Mean and Standard Deviation (in ns) of the RMS delay spread for different intra-WBAN links corresponding to CN1, for the three considered configurations.

SN	Standing	Local mobility		Global mobility	
	τ_0	$\bar{\tau_0}$	σ_τ	$\bar{\tau_0}$	σ_τ
1	4.34	3.81	0.32	3.85	0.63
2	12.20	12.61	0.28	12.46	2.02
3	9.25	10.07	0.18	10.08	2.30
4	9.31	9.84	1.32	11.27	1.37
5	8.57	9.17	0.95	10.02	1.58
6	7.23	8.33	0.45	9.19	1.63
7	4.15	3.95	0.97	4.06	0.95
8	6.89	7.16	0.14	8.69	2.51
9	6.13	6.78	0.41	8.62	1.94
10	6.53	6.40	0.25	8.27	1.65

H_0.

Comparing the cases of CN1 and CN2, as expected, a higher $\bar{H_0}$ is obtained for SNs located on the upper part of the body in the case of CN1, and vice versa. For instance, the difference between $\bar{H_0}$ for the cases of CN1 and CN2 is about 2.81 dB for SN1 and −3.5 dB for SN10. Concerning σ_0, we notice that in general using CN2 results in higher σ_0 compared to CN1. This can be explained by the fact that for the former case, the corresponding links experience more significant movements and frequent shadowing.

4.3.2 Delay Spread

To evaluate the channel frequency selectivity, we have calculated the average delay spread $\bar{\tau_0}$ and its standard deviation σ_τ for the three above-mentioned configurations. Results are presented in Tables 4.4 and 4.5 for the cases of CN1 and CN2, respectively. For the standing configuration, $\bar{\tau_0} = \tau_0$ and $\sigma_\tau = 0$; with τ_0 ranging from 4 to 12 ns for the case of CN1 and from 6 to 10 ns for the case of CN2. We notice slight variations in $\bar{\tau_0}$ for the local and global mobility cases. It can decrease or increase depending on the corresponding position of the SN and the CN; for a given user position, the proximity to room walls could then result in a shorter or a longer path length. For the local mobility case, the changes in $\bar{\tau_0}$ with respect to the standing configuration are less than 1.1 ns for CN1 and less than 2.2 ns for CN2. These variations are less than 2.5 ns for the case of global mobility.

As concerns the delay spread standard deviation, for the cases of CN1 and CN2, respectively, σ_τ ranges in 0.1 to 1.3 ns and in 0.2 to 1.9 ns for the local mobility configuration, while it ranges in

Table 4.5 — Mean and Standard Deviation (in ns) of the RMS delay spread for different intra-WBAN links corresponding to CN2, for the three considered configurations.

SN	Standing	Local mobility		Global mobility	
	τ_0	$\bar{\tau_0}$	σ_τ	$\bar{\tau_0}$	σ_τ
1	8.30	7.46	0.2	9.15	1.70
2	8.65	8.90	0.24	10.38	2.36
3	8.45	6.28	0.39	6.95	3.02
4	9.83	8.36	0.70	9.32	2.99
5	7.83	7.38	1.16	7.90	3.37
6	7.63	6.82	1.90	6.18	3.09
7	7.50	7.79	0.20	9.55	1.73
8	6.05	6.58	0.21	6.40	3.47
9	7.56	6.61	0.54	6.06	3.19
10	8.68	7.92	0.68	6.79	3.02

0.6 to 2.5 ns and in 1.7 to 3.5 ns for the global mobility configuration. The reason for the increase in σ_τ for the global mobility case is that, compared to the local mobility case where the user is at the center of the room, here we experience more important variations of the link path length. For instance, for the positions close to the walls, links will have relatively shorter path lengths when the user is facing the wall, and inversely, they will have longer path lengths when the back is against the wall. This results in more significant variations in τ_0, thus a larger σ_τ.

These results indicate that, when using a simple modulation technique such as OOK, the communication channel can be considered as frequency non-selective roughly for data rates up to approximately 5 Mbps (considering a rather loose upper bound of 20 ns for τ_0), where no channel equalization is required at the Rx. Given that the data rates in typical intra-WBAN applications are less than 1 Mbps [13, 16], we can effectively neglect the channel delay dispersion in practice.

4.3.3 Channel Dynamic Behavior

In order to evaluate the channel dynamics resulting from the user local and global mobility, let us investigate more closely the variations of the channel DC gain over time. This provides insight on the trend and the nature of the time variations of the channel DC gain (e.g. probable periodic patterns, stationarity properties, etc.) and its temporal correlation characteristics.

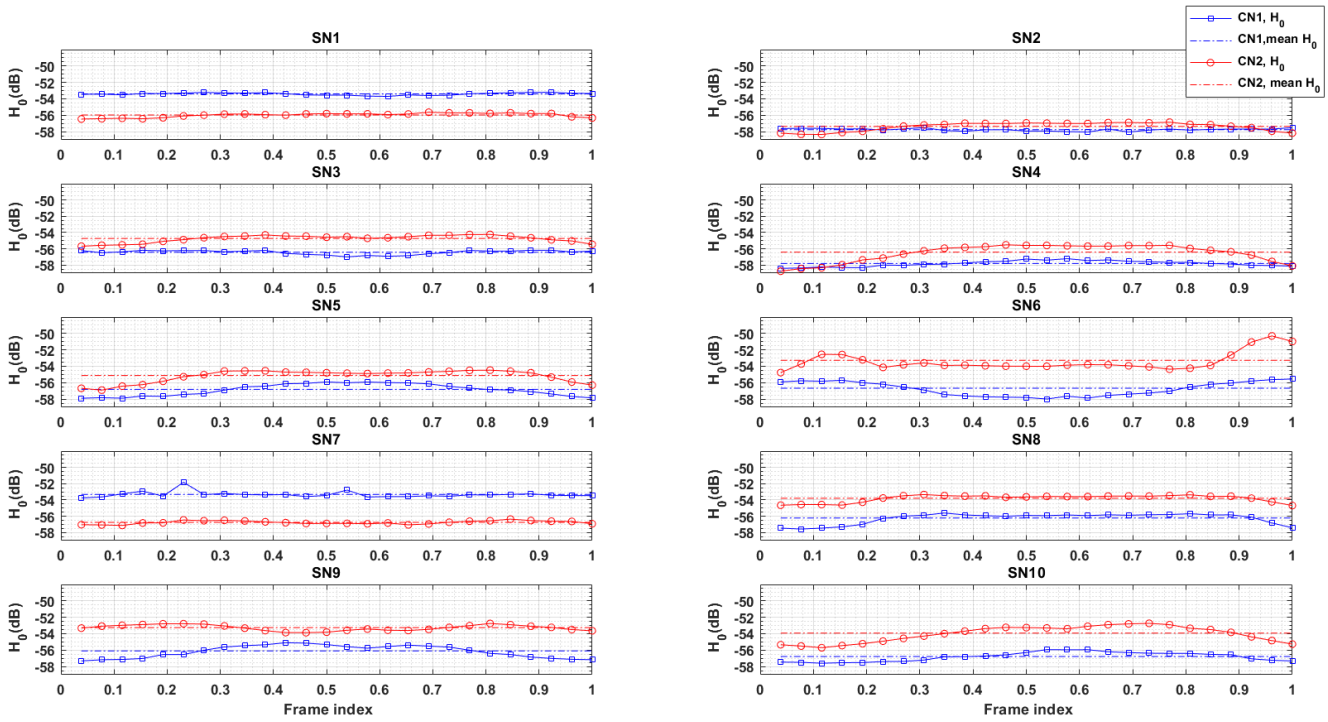

Figure 4.2 — H_0 variations and its mean value (in dB) for the cases of CN1 and CN2 in the local mobility configuration.

4.3.3.1 Local mobility

Figure 4.2 shows the time variations of H_0 for the cases of CN1 and CN2 in the local mobility configuration, where the abscissa represents the local mobility cycle, i.e., the frame number (see Fig. 3.7) normalized with respect to the total number of frames $N_{\text{frame}} = 27$. During the walk cycle, there is a periodic change of relative positions and orientations of the CNs and SNs. Also, link shadowing may occur resulting from body parts movement. For the body located at the center of the room and oriented toward one of the walls, these changes cause channel gain variations on the order of 0.2 to 2 dB for CN1, and 0.2 to 4 dB for CN2. This is consistent with the results presented in Subsection 4.3.1. A more detailed description of these results is provided in Appendix A.2.

An important point is to study the effects of Tx half-angle and room dimensions on H_0, which are not easily predictable. Indeed, for instance, a narrower Tx beam would imply more multipath reflections due to the increased LOS blockage probability whereas a wider beam could result in decreased LOS path gain and an effectively increased contribution of the multipath reflections. To investigate this, we have repeated the simulations by changing the Tx Lambertian order m from 1 to 45, and the room size from (5×5) to (10×10); results are not shown for the sake of brevity. Interestingly, we globally noticed the same trend as before with increasing m, with an increase in H_0 variations around 1 dB compared with $m = 1$; lower variations were noticed for the case of CN2 except for SN6. For this latter, LOS (present when the left leg is sufficiently raised) is mostly

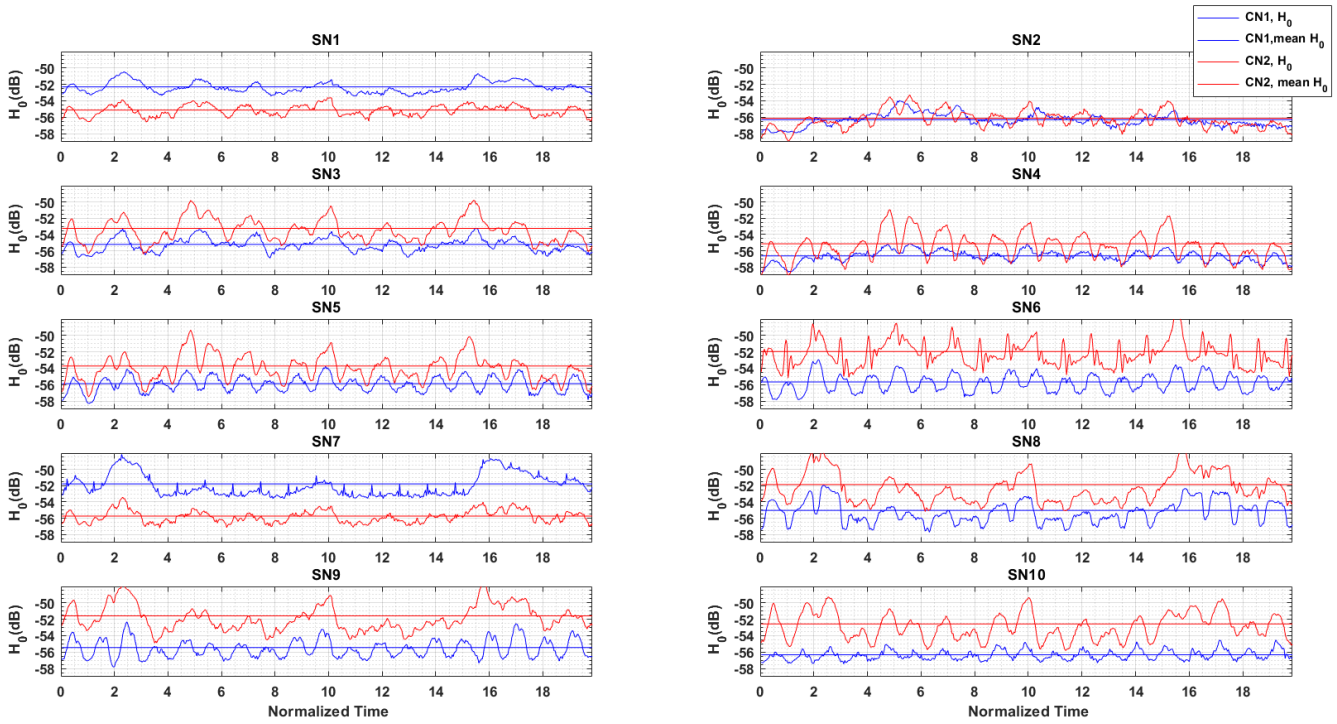

Figure 4.3 — H_0 variations and its mean (in dB) for the cases of CN1 and CN2 over the global mobility trajectory.

lost with a more directional beam. Also, when enlarging the room size, we again noticed the same global trend for all SNs, with a decrease in H_0 around 0.48 dB per 1 m^2 increase in the room size. Thus, the important result is that changing m or room size does not affect the general trend of the variations of the channel parameters.

4.3.3.2 Global mobility

Figure 4.3 shows the time variations of the DC channel gain for CN1 and CN2 during the global mobility scenario, where the abscissa represents the absolute time, in accordance with what is represented in Fig. 3.8. We can see that generally, global mobility implies channel gain variations by adding a random component, as compared to the periodic local mobility case. We can see that a straight walk towards a wall increases the channel gain, while rotations can increase or decrease it. This underlines the significant impact of user and body parts movement on the optical intra-WBAN channel. The presented results also show more significant variations of H_0 for the case of CN2. This can be explained by the fact that CN1 is mostly oriented toward the ceiling during the walk cycle, and consequently, it is less affected by the variations of body proximity to the walls due to rotations. Similar to the case of local mobility (see Subsection 4.3.1.2), the link between SN8 and CN2 experience periodic obstructions as a result of the right arm swinging back and forth during

the walk cycle.

4.3.4 Statistical Analysis of Channel Gain

Here, we present a statistical analysis of the DC channel gain H_0 for different SNs and CNs with the aim of proposing statistical models for their variations for the case of global mobility. Such a best-fit statistical channel model is in particular useful for the theoretical performance evaluation and the link physical layer design without resorting to timely numerical simulations of the optical channel. For this purpose, based on the AIC metric, described in Subsection 3.2.3, we have looked for the best fit of the corresponding data obtained from the simulations to Gaussian, Lognormal (LN), Rician, Gamma, Nakagami, and Weibull distributions. Globally, the best fit was obtained for LN, Gamma, and Nakagami PDFs, recalled in the following.

- LN:
$$f_X(x) = \frac{1}{x\sigma\sqrt{2\pi}} \exp\left(\frac{-(\ln(x)-\mu)^2}{2\sigma^2}\right), \tag{4.1}$$
where μ and σ stand for mean and standard deviation.

- Gamma:
$$f_X(x) = \frac{1}{b^a \Gamma(a)} x^{a-1} \exp(-\frac{x}{b}), \tag{4.2}$$
where a and b are the shape and rate parameters, respectively, and $\Gamma(\cdot)$ is the gamma function.

- Nakagami:
$$f_X(x) = \frac{2\alpha^\alpha}{\Gamma(\alpha)\,\xi^\alpha} x^{2\alpha-1} \exp\left(-\frac{\alpha}{\xi} x^2\right), \tag{4.3}$$
where α and ξ are the shape and scale parameters.

The corresponding fitted PDF parameters for each SN link together with the AIC values are presented in Appendix A.3, Tables A.2 and A.3, for the cases of CN1 and CN2, respectively.

Obviously, with this separate characterization of the different SN links, the estimated parameters highly depend on the exact locations and orientations of the sensors on the body. A more interesting approach is to find a global statistical model for the ensemble of the simulated H_0, i.e., corresponding to all links connecting a CN to different SNs. Compared to the SN-dependent distributions presented above, the obtained model will be simpler and more practical, i.e., with fewer parameters, but at the expense of less fitting accuracy. In fact, the SN-dependent model is useful for investigating special applications such as EEG and ECG recording, while the global model can be used as a generic channel model. Figures 4.4 and 4.5 illustrate the results of best-fit to different considered distributions, for the cases of CN1 and CN2, respectively. The best-fit model, according to the AIC criterion, for the case of CN1 corresponds to the Nakagami distribution, whereas the Gamma distribution provides the best-fit for links related to CN2. Table 4.6 presents the corresponding parameters of the two best-fit distributions together with the AIC values. Like for the case of individual SN characterization, Gaussian, Weibull, and Rician distributions showed less

tight fits. We suggest to use the Gamma distribution for both CN1 and CN2 cases since for the former, the difference between the corresponding Nakagami and Gamma PDFs in Fig. 4.4 is insignificant and AICs from Table 4.6 are rather close. Note that our results are consistent with the shadow fading models proposed for the case of RF-based WBANs, see for instance [25, 151].

Table 4.6 — Estimated parameters of best fit distributions to H_0 for the ensemble of simulated data.

CN	Best-fit PDFs	AIC	PDF parameters	
1	Nakagami	−4825	$\alpha = 3.72$	$\xi = 0.36$
	Gamma	−4772	$a = 13.79$	$b = 0.04$
2	Gamma	−3456	$a = 6.11$	$b = 0.07$
	LN	−3455	$\mu = -0.88$	$\sigma = 0.42$

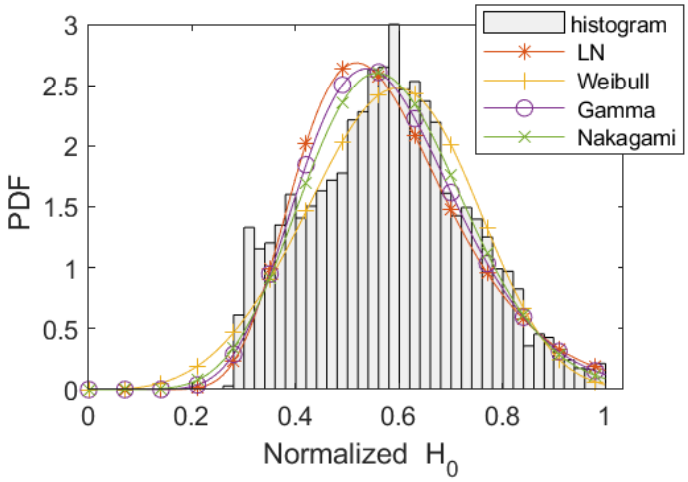

Figure 4.4 — Illustration of best-fitting PDFs to the ensemble of H_0 related to CN1.

4.3.5 Channel Coherence Time

Another important aspect in the design of appropriate signaling schemes concerns the statistical properties of the channel time variations. For this, we consider the ACF of the channel DC gain and coherence time for the different links. For instance, assuming a stationary channel, ACF indicates the correlation between different observation times, while the channel coherence time determines the packet length and the intervals of pilot transmission (used for channel estimation and probably for adaptive power control at the Tx) [151].

Figures 5.6 and 4.7 show the ACF of each SN link for the cases of CN1 and CN2, respectively, which are obtained based on the global mobility scenario. We notice an exponential decrease trend for all links, which is modulated by some oscillations whose frequency is related to the

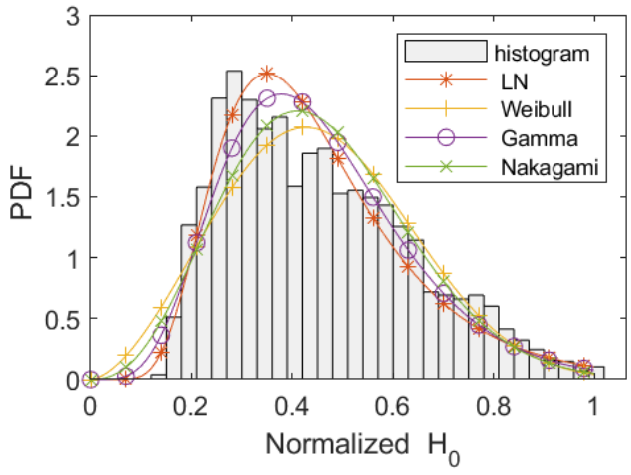

Figure 4.5 — Illustration of best-fitting PDFs to the ensemble of H_0 related to CN2.

movements of the corresponding SN during the walk cycle. We notice such oscillations even for SNs that experience small body swing movements, i.e., SN3, SN8, however, with small amplitudes. Indeed, SN3 on the torso is less affected by body movements than those SNs on the legs or arms.

Based on these results, we have estimated the channel coherence time as the delay at which the ACF drops by 50 % and 90 %, that we will denote by $T_{c,50}$ and $T_{c,90}$, respectively. The corresponding values are presented in Table 4.7. We notice a larger coherence time for SNs on the head and the torso, compared to those on the arms and the legs. For example, $T_{c,50}$ equals 1.01 and 2.09 sec for the links from SN5 and SN8 to CN2, respectively, which confirms a more stable channel for the latter link due to lower mobility.

Focusing on $T_{c,50}$, for instance, we note that it is on the order of hundreds of milliseconds to a few seconds, ranging between 0.78 to 3.27 sec for CN1 and between 0.95 to 2.26 sec for CN2. These relatively long coherence times indicate that optical intra-WBAN links have a slow time-varying nature, compared to their RF counterparts for which the coherence time is on the order of 0.025 to 0.07 sec [152, 153]. As a result, optical WBAN links benefit from larger packet sizes, a lower pilot overhead, and the possibility of using a simpler adaptive transmit power control over successive packets.

4.4 Performance analysis

For the considered system, we present here numerical results to study the performance of the intra-WBAN links in terms of outage probability. Following the method described in subsection 3.3.4, we generate for each SN-CN link, $N'_{\text{config}} = 10^7$ values for H_0 and calculate the BER for each value according to Eq(3.19). Then, P_{out} is calculated considering a $\text{BER}_{\text{th}} = 10^{-3}$. Note that given that P_t is the transmit power for sending an “On” OOK symbol, the average transmit power

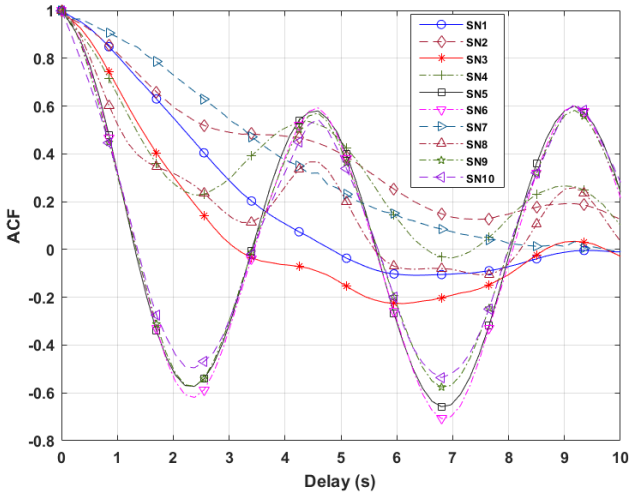

Figure 4.6 — ACF for the links between different SNs and CN1.

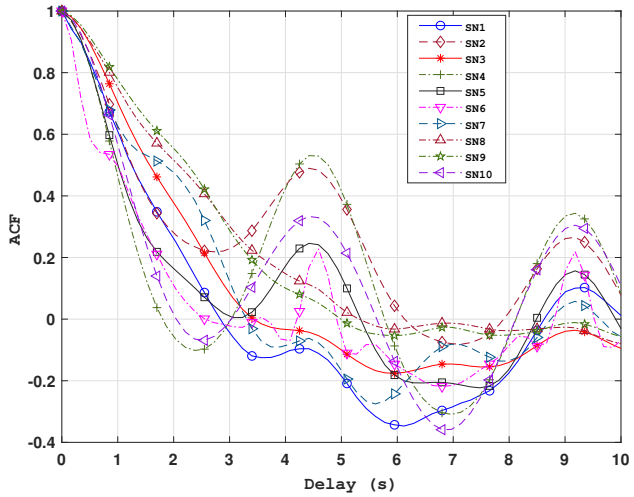

Figure 4.7 — ACF for the links between different SNs and CN2.

equals $(1+\alpha)\,P_t\,/2$, with α the extinction ratio.

4.4.1 Effect of PD Type and Data-Rate

Let us first compare the effect of link data-rate on the performances of PIN- and APD-based Rxs. For this, concerning the background noise, we set $I_b = 200\mu$A [98]. We have shown in Fig. 4.8 plots of P_{out} versus P_t for R_b ranging between 1 kbps and 50 Mbps. Here, for the sake of brevity, we show only the link from SN3 to CN1. We reasonably get a lower P_{out} for increased P_{t}, while a higher P_{out} is obtained for increased R_b due to increased thermal noise variance. As expected, APD provides a better performance due to its internal gain: for instance, for $R_b = 200$ kbps and a target P_{out} of 10^{-4}, the required P_{t} is about 41 and 29 mW for the cases of PIN- and APD-based Rxs, respectively.

Table 4.7 — Channel coherence time: Delays (in seconds) corresponding to 90 % and 50 % of the ACF.

SNs	CN1		CN2	
	$T_{c,50}$	$T_{c,90}$	$T_{c,50}$	$T_{c,90}$
1	2.19	0.63	1.25	0.34
2	2.81	0.62	1.26	0.40
3	1.44	0.43	1.57	0.49
4	1.34	0.35	0.95	0.36
5	0.83	0.28	1.01	0.36
6	0.81	0.28	0.99	0.18
7	3.27	0.90	1.82	0.33
8	1.06	0.33	2.09	0.51
9	0.79	0.27	2.26	0.56
10	0.78	0.17	1.10	0.40

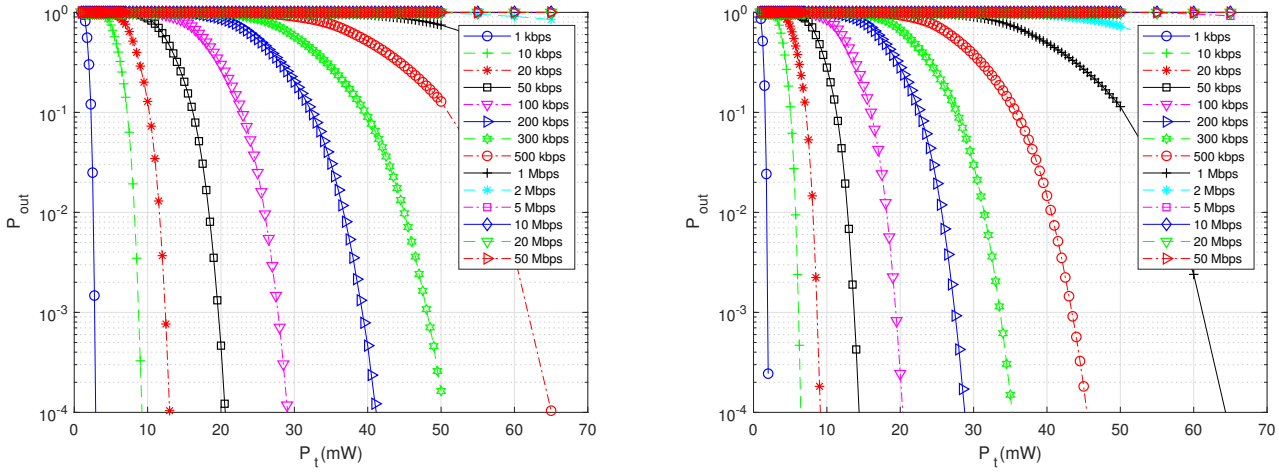

(a) (b)

Figure 4.8 — P_{out} versus peak transmit power P_t for different data-rates R_b for the case of SN3-to-CN1 link using (a) a PIN (b) an APD. Uncoded NRZ-OOK modulation.

4.4.2 Comparison of Intra-WBAN Links for Low Background Noise Level

Let us now compare the performances of the different links from SNs to CNs. We consider only the case of $R_b = 100$ kbps for both the PIN- and the APD-based Rxs, for the sake of brevity. First,

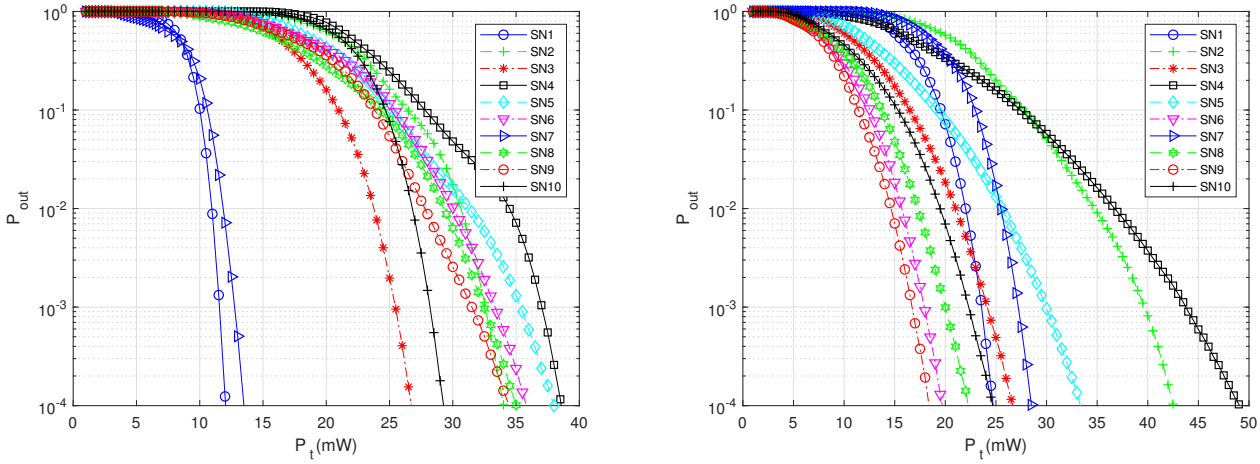

(a) (b)

Figure 4.9 — P_{out} versus peak transmit power P_t for different SN links and the cases of (a) CN1 and (b) CN2. Low background noise level with $I_b = 2\,\mu$A.

we consider the case of negligible background noise with $I_b = 2\,\mu$A (corresponding to background noise from fluorescent lights [154]), which could correspond to nighttime conditions. We have presented in Fig. 4.9 plots of P_{out} versus P_t for different SN links and for a PIN-based Rx. Note that the P_{out} values for the APD case are too low for the considered R_b and are not shown here. We notice that, generally, CN1 experiences a better link performance for SNs placed on the upper part of the body. For instance, to achieve a target $P_{\text{out}} = 10^{-4}$, the required P_t for SN7 are 13.5 and 28 mW, for the cases of CN1 and CN2, respectively. Meanwhile, CN2 experiences a better performance for SNs placed on the lower part of the body.

As another important result, we notice that, for the SNs located on the upper part of the body, the P_{out} slopes in the case of CN2 are smaller compared to the case of CN1, which means that CN1 is less affected by intensity fluctuations, or in other words, by channel fading. The inverse holds for the SNs on the lower part of the body, e.g., SN6, SN8 and SN9.

Based on these observations, we can deduce that the choice of CN placement is application dependent. For instance, for EEG applications, most of SNs will be placed on the head, where CN1 is a better choice. On the other hand, for ECG applications, SNs are placed on the heart, arms, and legs, where CN2 position should be preferred. Lastly, note that we can reduce the thermal noise by using a larger R_L, which is feasible given the low data rates needed in our context.

Comparing the results for different SNs, we can deduce the effect of mobility and shadowing. For instance, we notice from P_{out} plots of SN3 and SN5 (placed on the chest and left arm, respectively), that the former link achieves a better performance. We observe the same trend between SN2 and SN4 links. As expected, local mobility results in a degradation of the link performance. Also, from P_{out} plots in Fig. 4.9(a) of SN3 and SN10, we notice a better performance for the former for the case of CN1, whereas SN10 achieves a better performance for the case of CN2 from

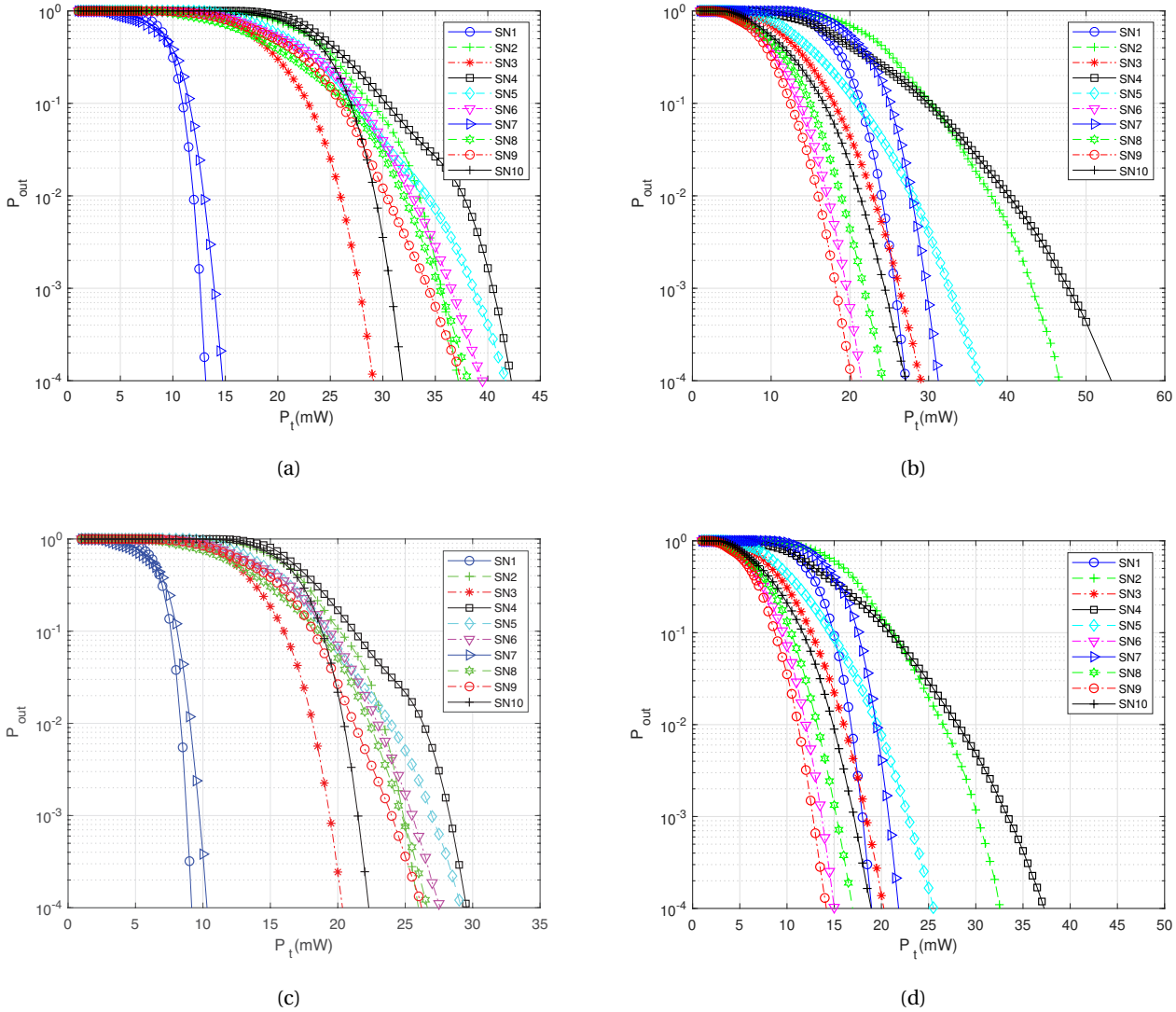

Figure 4.10 — P_{out} versus the peak transmit power P_t for different SNs for the cases of (a) CN1 with PIN PD, (b) CN2 with PIN PD, (c) CN1 with APD, and (d) CN2 with APD. Relatively high background noise level with $I_b = 200\,\mu$A.

Fig. 4.9(b). We can explain this by the higher probability of shadowing for CN2, due to the swing of the right arm during the walk.

4.4.3 Comparison of Intra-WBAN Links for Relatively High Background Noise Level

Consider now the case of relatively high background noise level with $I_b = 200\,\mu$A, that can be considered as corresponding to daytime conditions [98]. Plots of P_{out} versus P_t for this case are shown in Fig. 4.10. We notice the same trends between SN-CN links as in the previous subsection with a degradation of the link performances with increase in the background noise level, as expected. For instance, for the case of the PIN-based Rx, the required P_t to achieve the same performances as

in the previous case increases for all SNs by approximately 2 to 5 mW. Considering the link form SN5 to CN1, for a target P_{out} of 10^{-4}, the required P_t is 43 mW from Fig. 4.10(a), while it is 38 mW from Fig. 4.9(a). Notice that the performance degradation is more significant in the case of the APD-based Rx. This was expected due to the internal gain of the APD.

Comparing PIN- and APD-based Rxs, we observe the same trend between the different SN links, with the APD-based Rx still having a better performance (i.e., requiring a lower P_t to achieve a target P_{out}). For instance, for the link between SN10 and CN2, the required P_t to achieve $P_{\text{out}} = 10^{-4}$ is 54 mW for the case of PIN-based Rx from Fig.4.10(b), while it is only 37.5 mW when using an APD-based Rx from Fig.4.10(d).

4.5 Chapter summary

We investigated channel modeling and characterization for optical intra-WBANs links, i.e., between a set of SNs and a CN, during a walk scenario. The presented study provides useful insights into the effects of local and global user mobility and the corresponding beam shadowing. These effects were investigated using a realistic dynamic model based on a 3D animation of the walk cycle and a modified RWP mobility. MCRT-based simulations were then carried out using the Opticstudio software to obtain the CIRs for a set of SN and CN configurations at different instants of the walk scenario. The considered configurations cover the most likely locations of the CN and the SN for a practical implementation of a medical WBAN. We presented comprehensive numerical results on the channel first- and second-order statistics, namely the DC gain, delay spread, ACF, and coherence time. The positions and orientations of SNs and CNs along with the body geometry were found to have a significant impact on the channel gain statistics. Nevertheless, overall, the channel can be considered as frequency non-selective for data-rates up to 5 Mbps when using the simple OOK signaling, for example. Consequently, ISI can be neglected for most medical WBAN applications.

For the case of local mobility with the body located at the center of the room and oriented toward one of the walls, we showed periodic changes of the channel gain with variations on the order of 0.2 to 4 dB. Changing the Tx beam divergence or the room size was found to affect negligibly the general trend of the channel parameters variations. On the other hand, global mobility was shown to cause a higher attenuation and more significant random variations of the channel gain, compared to local mobility. Based on the datasets obtained from simulations, we proposed best-fit models to describe the statistical distributions of the channel parameters, which are particularly helpful for studying the channel behavior (and consequently, the link performance) for physical or upper layer design. LN and Gamma distributions were found to provide the best AIC fit models for the channel attenuation. Regarding channel time variations, optical intra-WBAN links were shown to have a slower time-varying nature (thus, of higher stability), as compared to their RF counterparts; the corresponding coherence times ranging between a few hundred milliseconds to a few seconds.

Note that the presented study was based on considering the typical body shape and dimensions of an adult person. The choice of body shape will determine the propagation of the rays in the vicinity of the human body. i.e., which rays will be absorbed by the body and which will be traced. The presented analysis, however, remains valid for the general case, in particular regarding the mobility effect. For example, for the case of a child, most propagation properties with respect to the local and global movements remain the same.

Based on the derived statistical channel model using non-parametric KDE, we investigated further the outage probability performance of different SN-CN links for the two cases of PIN- and APD-based Rxs. We showed the impact on the link reliability of CN positioning, which is related to the effect of link shadowing caused by the body parts movements, which can cause a significant degradation of the link performance. Therefore, the optimal placement of the CN depends on the targeted application. Lastly, investigating the effect of background radiations on the link performance, and given the generally low levels of required transmit power P_t, which remain in the eye-safe region, we can conclude the feasibility of implementing optical WBAN links in practice, in both daytime and nighttime conditions.

Chapter 5

Channel Modeling and Performance Analysis of Extra-WBAN links

Contents

5.1 Introduction 67
5.2 Simulation Approach 68
5.2.1 General Assumptions 68
5.3 Channel Characterization, Numerical Results 69
5.3.1 Single AP Configurations 69
5.3.2 Multiple AP Configurations 70
5.3.3 Channel RMS Delay Spread 71
5.3.4 Channel Coherence Time 73
5.4 Link Performance Analysis 73
5.4.1 Statistical Model of Channel Gain 73
5.4.2 Performance Comparison of Single and Multiple AP Configurations 75
5.4.3 Performance Comparison of PIN- and APD-based Rxs 76
5.5 Chapter summary 76

5.1 Introduction

In Chapter 4, we investigated channel characterization of optical intra-WBAN links via MCRT simulations, and further studied their performance. The fundamental differences of intra- and extra-WBAN links, in particular, regarding shadowing and link blockage properties, necessitate a dedicated study for the latter case.

In this chapter, we investigate the channel modeling and performance of optical extra-WBANs in the uplink. In contrast to the previous works on the topic, this study is based on more accu-

rate and realistic channel models as described in Chapter 3. Section 5.2 presents the considered simulation approach and parameter specification. Then, numerical results are provided in Section 5.3 to study the main channel metrics for different configurations, similar to the approach in Chapter 4. Next, in Section 5.4, the link performance is quantified in terms of outage probability considering OOK modulation. We further investigate the performance improvement achieved by using multiple APs. Lastly, Section 5.5 summarizes the chapter.

5.2 Simulation Approach

5.2.1 General Assumptions

Consider an extra-WBAN link between a CN on the patient's body and an AP. Like in Chapters 3 and 4, we consider two different placements for the CN, i.e., on the shoulder (the Rx pointing upward) and on the waist (the Rx pointing horizontally ahead) [19], see Fig.5.2. We consider an LED at the Tx side, i.e., at the CN, emitting on IR wavelength of $\lambda_0 = 850\,\text{nm}$ with a bandwidth of $\Delta\lambda = 30\,\text{nm}$, as well as a Lambertian pattern LED of $m = 1$ in order to ensure minimum beam blockage. For the sake of simplicity, we again consider an empty room, i.e., without any furniture or equipment.

At the Rx side, i.e., at the AP, we consider a simple PIN PD of $1\,\text{cm}^2$ active area without any lens and with a large FOV of 60° (semi-angle). Note that the assumption of such a relatively large active area is justified by the fact that relatively low data-rates, on the order of 1 Mbps at most, are required in medical WBANs [13]. To investigate the practical interest of using more than one AP at the Rx, we also consider the case where several APs are used in order to minimize beam blockage probability [155]. For this, multiple APs will be considered either on the ceiling or on the walls of the room. Then, the received signals are combined based on equal gain combining (EGC) or selection combining (SC) (i.e., taking the strongest signal) strategies [156]. We consider two trajectories of 516 and 587 sequential snapshots, generated using the modified RWP method described in Chapter 3. Overall, the two trajectories give an acceptable coverage of the room area and a detailed enough statistical description of the walk cycles. Note that generating these data has necessitated quite long Opticstudio simulations.
Figure 5.1 shows the top view of the room with the considered positions for the APs, and also illustrates the considered positions of the CN on the body. As it can be seen, AP1-AP5 are symmetrically placed on the ceiling and point downward. Also, AP6-AP9 are placed at half width and 2 m height and point straight toward the center of the room. Note that, by default, we consider the case of AP5 (i.e., a single AP at the center of the ceiling).

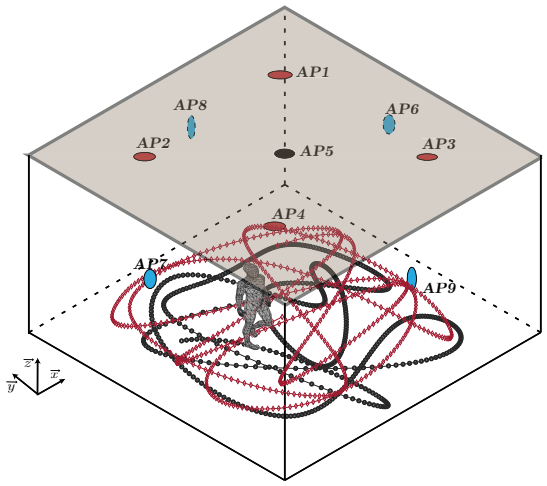

Figure 5.1 — Illustration of the considered placements for the APs and the simulation trajectories.

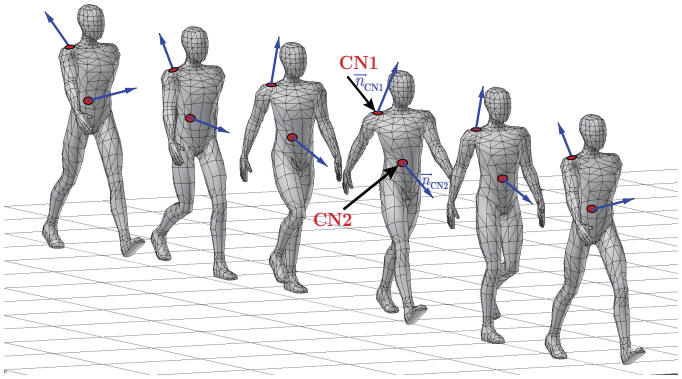

Figure 5.2 — Illustration of the considered placements for the CNs.

5.3 Channel Characterization, Numerical Results

5.3.1 Single AP Configurations

First, consider the case of a single AP at the center of the ceiling or on the wall, i.e., AP5 or AP8 in Fig. 5.1. Figure 5.3 shows the time evolution of the channel DC gain H_0, for the two cases of CN1 and CN2 considering the first simulated walk trajectory (i.e., $N_{\text{config}} = 516$). The abscissa represents the simulation time, with a time step of $\Delta t = 0.17$ sec.

Notice first the larger H_0 in average for CN1, compared to CN2. Interestingly, for a given CN position, the average H_0 is more or less the same, regardless of the position of the AP. The mean H_0 corresponding to CN1 and CN2 cases is around -53 and -55 dB, respectively. As for H_0 variations, we notice for both AP5 and AP8, larger variations and longer mean time between failures (MTBF) for CN1 case. For example, the range of H_0 variations for AP5 is around 9.2 and 4.4 dB, for CN1 and CN2 cases, respectively. The corresponding standard deviation is about 3 dB for CN1, and it ranges between 1 to 2 dB for CN2. In addition, compared to AP5, larger H_0 variations are observed

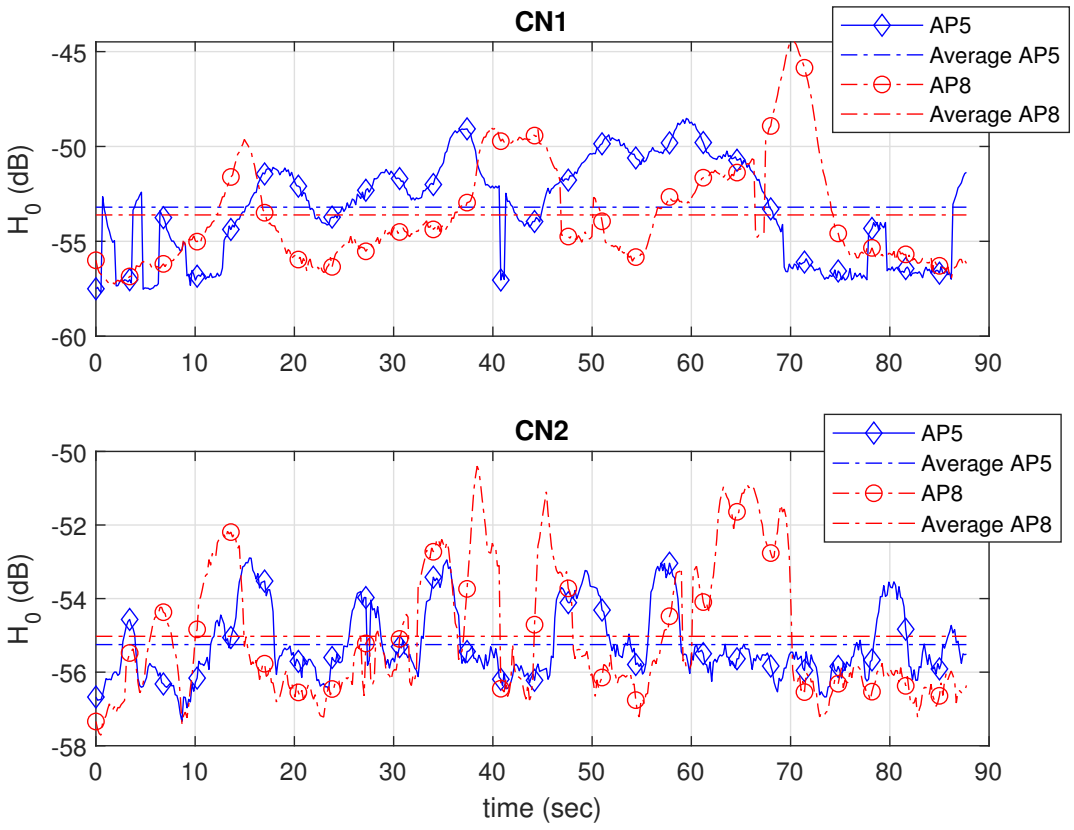

Figure 5.3 — H_0 variations for the cases of CN1 and CN2 in the single AP configuration for AP5 and AP8 positions (see Fig.5.2).

for AP8, with ranges about 12.8 and 7.3 dB, for CN1 and CN2 cases, respectively. These relatively large variations can be explained by the fact that, compared to AP5, AP8 is more sensitive to body shadowing caused by body rotations during the walk trajectory.

5.3.2 Multiple AP Configurations

Consider the case of using four APs for two configurations of APs placed on the ceiling (i.e., AP1 to AP4) or on the walls (i.e., AP6 to AP9), see Fig. 5.2. Let us first consider the case of individual APs separately. In Fig. 5.4 the time evolution of H_0 is shown for the cases of CN1 and CN2. Note that CN1 in average has a slightly larger H_0 for the case of APs located on the ceiling (around 0.5 dB difference), while CN2 has a larger H_0 for the case of APs located on the walls: the mean H_0 for the case of CN1 and CN2 is -54 and -55 dB, respectively. Notice also higher H_0 variations for the case of CN1 with the APs located on the ceiling, compared with APs on the walls: the corresponding standard deviation of H_0 is about 3 and 2 dB, respectively. This can be explained by the fact that the links from CN1 to AP1-AP4 experience frequent transitions between the availability or absence of the LOS path. On the other hand, CN2 has similar H_0 variations for both configurations, where its standard deviations are around 1.7 dB.

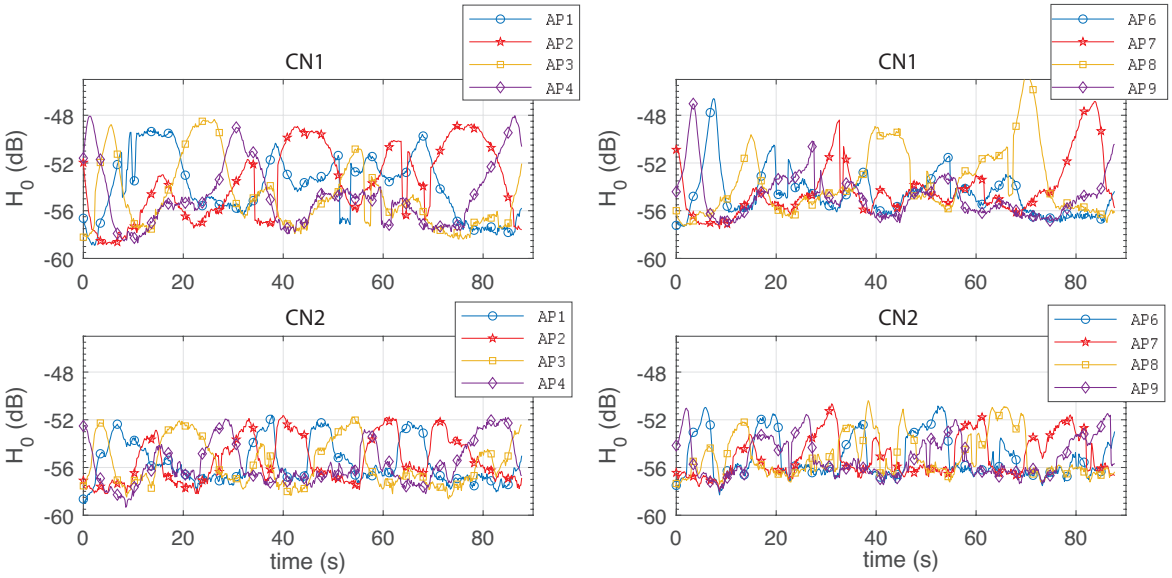

Figure 5.4 — H_0 variations for the cases of CN1 and CN2 in the multiple-AP configurations using EGC and SC detection methods.

Interestingly, in the case of CN2, less correlation is observed between the signals received on different APs. In other words, a higher effective diversity is obtained in this case. This can be explained by the short distance between CN1 and the APs which gives a strong LOS, while the coverage area of CN1 is smaller than CN2, which makes it more subject to user's movements. Figure 5.5 shows the variations of H_0 for the cases of EGC and SC techniques. As expected, the use of multiple APs, in particular with EGC, increases the mean H_0 and especially reduces its standard deviation due to spatial diversity. Compared to the single AP configuration, the increase in the mean H_0 is around 5.8 to 6.2 dB with EGC, and around 2.2 to 2.8 dB with SC, for both (AP1-AP4) and (AP6-AP9) cases. Meanwhile, compared with CN2, we notice a higher average H_0 (about 1.1 to 2.6 dB) and larger H_0 variations (about 1.4 to 3.6 dB) for the case of CN1, similar to the single AP configurations. Also, larger variations and shorter MTBFs are observed for the case of (AP6-AP9), compared with (AP1-AP4). This would suggest that the (AP1-AP4) configuration is more robust against user mobility effects. Based on this, in the sequel, only the case of (AP1-AP4) configuration is considered.

5.3.3 Channel RMS Delay Spread

Channel delay spread is the key factor for quantifying channel frequency selectivity and the need to channel equalization at the Rx [101]. From the simulated CIRs, we have calculated the mean and the standard deviation of the RMS delay spread, denoted by $\bar{\tau}$ and σ_τ, respectively. Results are presented in Table 5.1 for single and multiple AP configurations and the cases of CN1 and CN2.

For the single AP configurations, $\bar{\tau}$ ranges between 5.2 to 10.2 ns, with σ_τ between 1.9 and 4.4 ns. For AP5, we notice a smaller $\bar{\tau}$ with CN1, whereas a smaller $\bar{\tau}$ is obtained for AP8 with CN2. Comparing the cases of CN1 and CN2, we generally notice shorter $\bar{\tau}$ for the former, and lower σ_τ for the

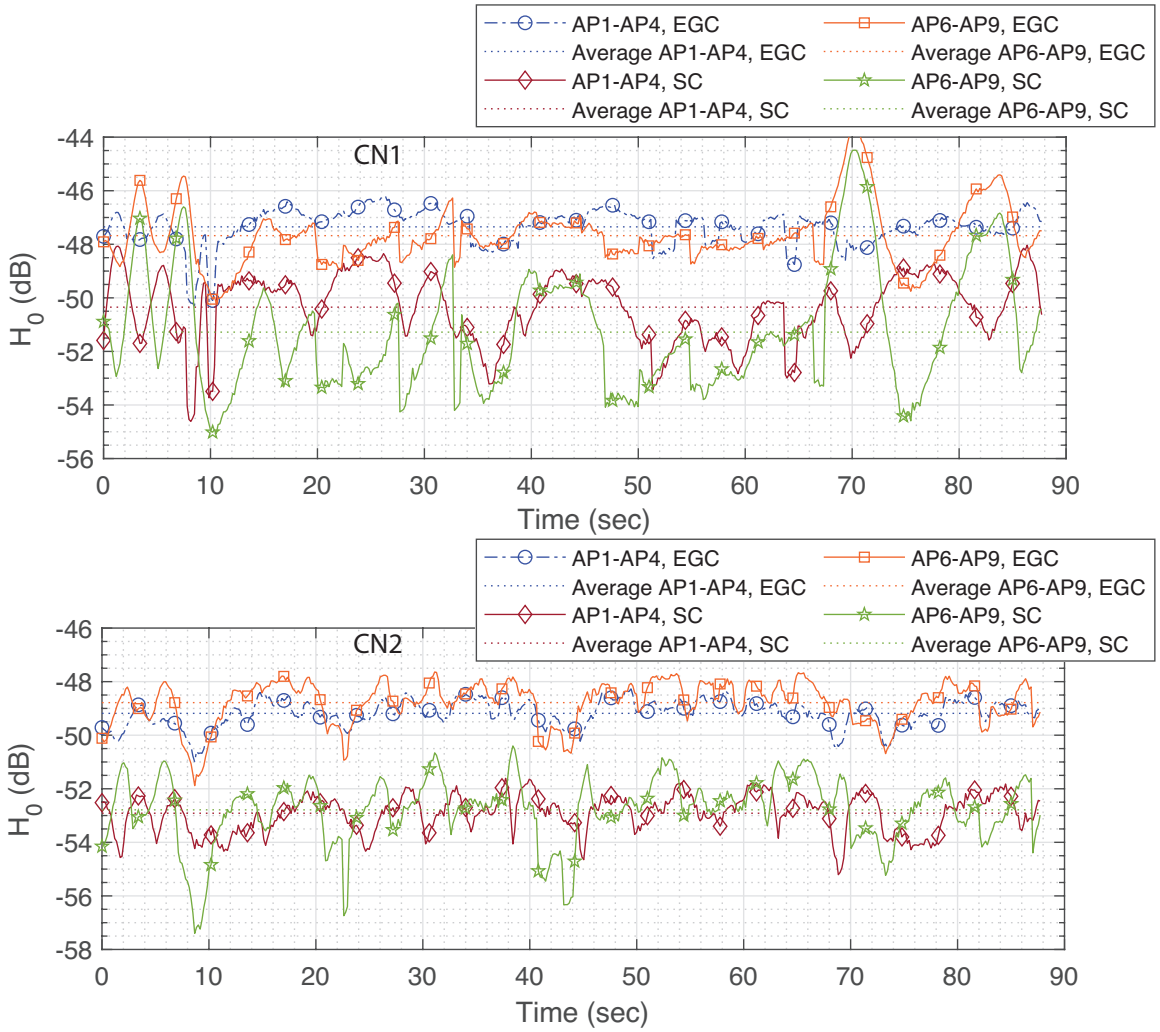

Figure 5.5 — H_0 variations for the cases of CN1 and CN2 in the multiple-AP configurations using EGC and SC detection methods.

Table 5.1 — Mean and standard deviation (in ns) of the RMS delay spread.

Configuration			CN1		CN2	
			$\bar{\tau}$	σ_τ	$\bar{\tau}$	σ_τ
Single AP	Ceiling AP5)		5.2	4.4	10.2	1.9
	Wall (AP8)		7.3	4.2	8.3	3.7
Multiple APs	Ceiling (AP1-AP4)	EGC	4.7	1.6	11.3	0.8
		SC	7.9	3.8	7.1	3.6
	Walls (AP6-AP9)	EGC	6.1	4.2	8.6	2.9
		SC	7.4	3.0	9.5	1.9

latter. A shorter $\bar{\tau}$ can be explained by a less shadowing impact on the direct LOS path, given the random orientations and positions of the Tx.

For the multiple AP configurations, we notice the same trend and the same range of $\bar{\tau}$ for the cases of CN1 and CN2 as for the single AP configurations. Nevertheless, with EGC detection, we have a quite smaller σ_τ, especially for APs on the ceiling, but it is the inverse for SC detection, which is again rational.

Overall, from these results and assuming simple OOK modulation, we can conclude that the communication channel can be considered as effectively frequency non-selective for data-rates up to approximately 10 Mbps, regardless of the position of the Tx. When AP(s) is (are) positioned on the ceiling, this condition is verified even for higher data-rates.

5.3.4 Channel Coherence Time

Channel coherence time T_c is a useful metric for characterizing channel time variations. It determines, for instance, the MAC layer parameters for setting the frame length and the transmission of training sequences. As explained in Section 5.2, to approximate T_c, we consider the delay where the ACF falls by 50%. The corresponding values are presented in Table 5.2. We have also presented the ACF plots for the different AP configurations and the cases of CN1 and CN2 in Fig. 5.6. The interesting point is the substantial reduction of the coherence time for the multiple AP configurations. In particular, a reduction of factor 3 is observed for the case of CN1 with respect to the AP5 configuration. This means that despite the benefit of spacial diversity in reducing channel fading, we have a degraded channel stability due to a higher dynamic for the ensemble of underlying channels.

Focusing on the ACF plots, we further notice a different trend for CN1 and CN2 cases, for AP5 and AP8 configurations. These results are consistent with those previously presented for H_0 above. For instance, for AP5 with CN1, the link is either LOS or shadowed by the head of the user for relatively a long period, thus a more spread ACF and a larger T_c. Whereas the link AP5 with CN2 is subject to periodic shadowing from the arms, which results in more variations, thus a more compact ACF and a smaller T_c. For the multiple AP configurations, we notice similar trends between CN1 and CN2 as for the single AP configurations. Also, the ACFs of the EGC strategy gives identical T_c values for CN1 and CN2 with the cases of both APs on the ceiling and the walls, whereas the SC strategy is slightly better for the case of APs on the walls (about 0.1 sec).

5.4 Link Performance Analysis

5.4.1 Statistical Model of Channel Gain

As explained in Subsection 3.3.4, to calculate the link BER, H_0 is generated randomly based on Gaussian-kernel KDE for the considered scenarios. For this, we reasonably combine the data of

Table 5.2 — Estimated channel coherence time T_c (in sec) corresponding to the 50 % of the ACF, based on the simulated user trajectory.

Configuration			CN1	CN2
Single AP	Ceiling		4.2	1.4
	Wall		2.3	2.0
Multiple AP	Ceiling	EGC	1.5	1.0
		SC	1.4	0.9
	Walls	EGC	1.5	1.0
		SC	1.6	1.0

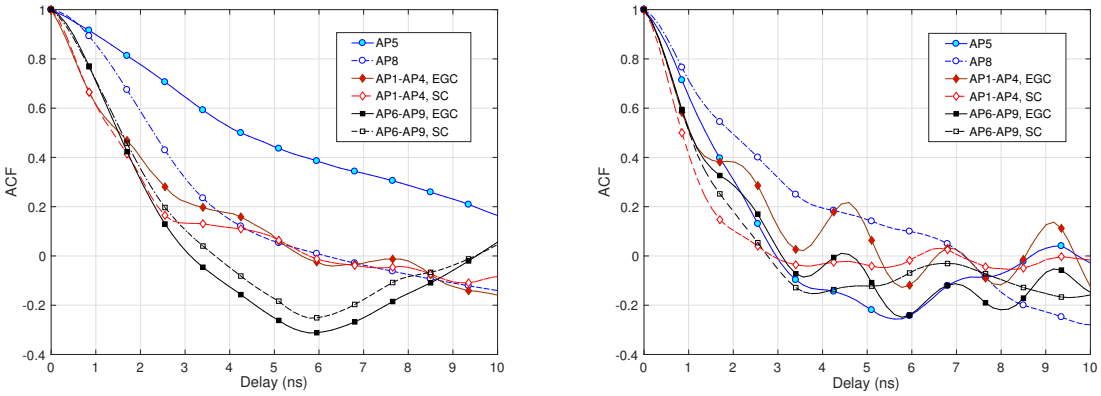

Figure 5.6 — Calculated ACF for the cases of (a) CN1 and (b) CN2 and different AP configuration based on the simulated user trajectory.

the two generated trajectories to increase the accuracy of the statistical estimation and also to have a better representation of the movement area. For instance, in Fig. 5.7, the 1103 samples histograms of the simulated H_0 for the case of CN1 via Opticstudio are presented together with the KDE-based PDF fits. The corresponding KDE parameters are specified in Table 5.3. First, notice a

Table 5.3 — Calculated smoothing parameter ρ.

Configuration			CN1	CN2
Single AP	Ceiling (AP5)		0.1579	0.0402
	Wall (AP8)		0.1115	0.0731
Multiple AP	Ceiling	EGC	0.0339	0.0314
		SC	0.0813	0.0462
	Walls	EGC	0.0453	0.0417
		SC	0.1138	0.0608

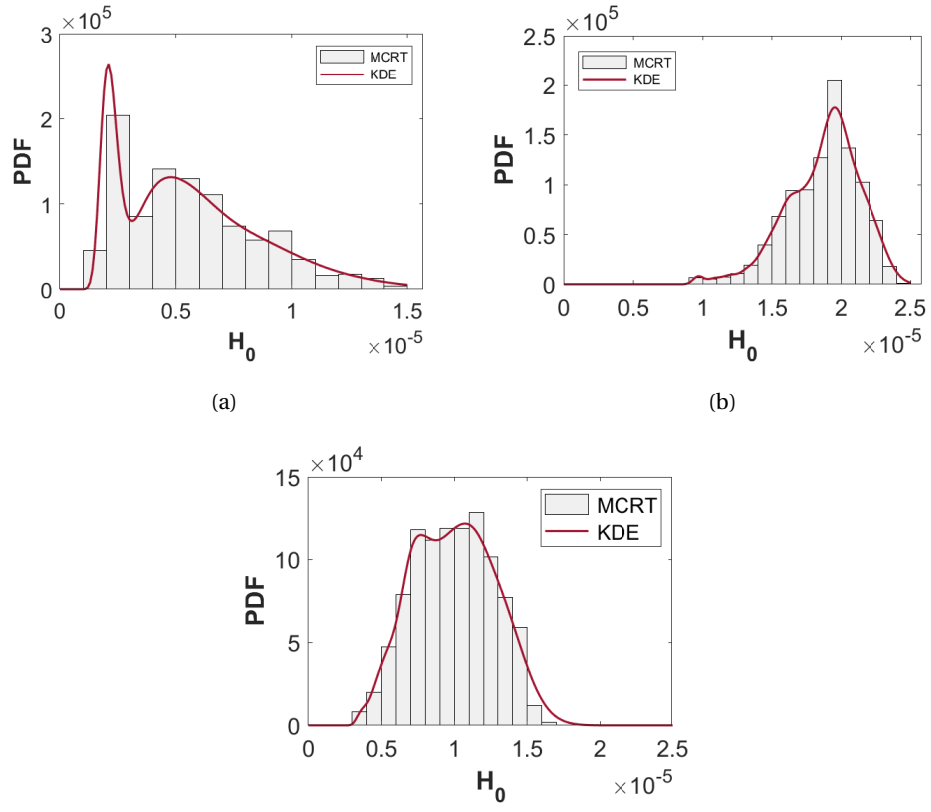

Figure 5.7 — Histograms of H_0 (in linear scale) for 1103 channel realizations and estimated PDF by KDE with Gaussian kernel. (a) CN1 and AP5, (b) CN1 and AP1-AP4 with EGC and with (c) SC.

good fit between the histograms of the simulated data and the estimated PDFs, in particular for the multiple AP cases with EGC. Also, the reduction in the histogram spread (in particular, for EGC) shows the benefit of spatial diversity in reducing shadowing and link blockage effects.

5.4.2 Performance Comparison of Single and Multiple AP Configurations

Using the obtained approximate PDFs, we randomly generate more than $N'_{\text{config}} = 10^7$ channel realizations. For each generated H_0, the BER is calculated from (3.19). Given the slow time-varying nature of the channel, the outage probability P_{out} is considered for the link performance analysis, which is, again, defined as the probability that the instantaneous link BER goes above a given threshold $\text{BER}_{\text{th}} = 10^{-3}$.

For the case of PIN-based Rx, Fig. 5.8 shows plots of P_{out} versus P_t for R_b ranging between 10 kbps to 1 Mbps, for the cases of CN1 and CN2, and single or multiple APs on the ceiling, i.e., AP5 or (AP1-AP4). Considering first the single AP case, notice the degradation of P_{out} with an increase in R_b, as expected. In fact, the Rx low-pass filter (LPF) bandwidth is changed according to

R_b. Consequently, for increased R_b, the Rx noise variance increases, resulting in a BER degradation. For the multiple AP case, from Figs. 5.8(c) and 5.8(e), for a given R_b, we reasonably note a considerably lower required P_t with EGC to attain a target P_{out}. For instance, for $P_{\text{out}} = 10^{-3}$ and $R_b = 100$ kbps, the required P_t is around 5.5 and 18 mW for the cases of EGC and SC signal detection, respectively, compared with 40.5 mW for the case of single AP from Fig. 5.8(a). This elucidates the tangible enhancement of the link reliability achieved by spatial diversity. Another interesting result is that the CN2 case offers a better performance than CN1 for the single AP configuration. This can be explained by the fact that the link to CN1 depends highly on the availability of the LOS, while the link using CN2 depends rather on first-order reflections. Given that the availability of LOS is less likely than that of first- and higher-order reflections, the link to CN2 can be considered as to be more stable. However, for the multiple AP configuration, the links to CN1 and CN2 have similar performance for both EGC and SC strategies. This similarity is again due to the spatial diversity that increases the likelihood of LOS and diffuse link availability, with the result of reduced shadowing and link blockage effect.

5.4.3 Performance Comparison of PIN- and APD-based Rxs

Figure 5.9 shows the performance of PIN and APD versus I_b with the two combination strategies for the case of CN1 and CN2, $P_t = 15$ mW, and $R_b = 200$ kbps (recall that I_b denotes the average photo-current due to background noise).
First, as it could be expected, the multiple AP configuration with EGC offers the best performance for both cases of CN1 and CN2. The corresponding P_{out} is too low for the considered I_b, this is why they are not shown in the figure. From Fig. 5.9(a), considering a target $P_{\text{out}} = 10^{-3}$, and the APD-based Rx, the link can operate up to an I_b of 80μA and 510μA, for the cases of AP5 and AP1-AP4 with SC detection, respectively. Also, as was expected [102], the performance of the APD-based Rx is more affected by I_b, compared to the PIN-based Rx. For example, from Fig. 5.9(b), considering AP1-AP4 with SC detection, for I_b up to 525 μA, the APD-based Rx has a better performance, whereas the inverse holds for $I_b > 525\,\mu$A. Interestingly, the case of single AP with APD-based RRx outperforms the PIN-based multiple AP with SC detection for $I_b \lesssim 155\,\mu$A. This I_b corresponds to environments with filtered ambient indirect sunlight [98, 103].

5.5 Chapter summary

We investigated channel characterization and performance study for medical optical extra-WBAN links, taking into account user mobility using a dynamic model based on a 3D animation of the user walk cycle and a modified RWP model. Based on an accurate MCRT approach, we calculated the CIR and the channel DC gain and studied the impact of the CN position on the user body and AP placement on different locations of the room. The presented results and analysis is quite insightful in the design of medical WBANs by taking into account practical and realistic system parameters and channel characteristics.

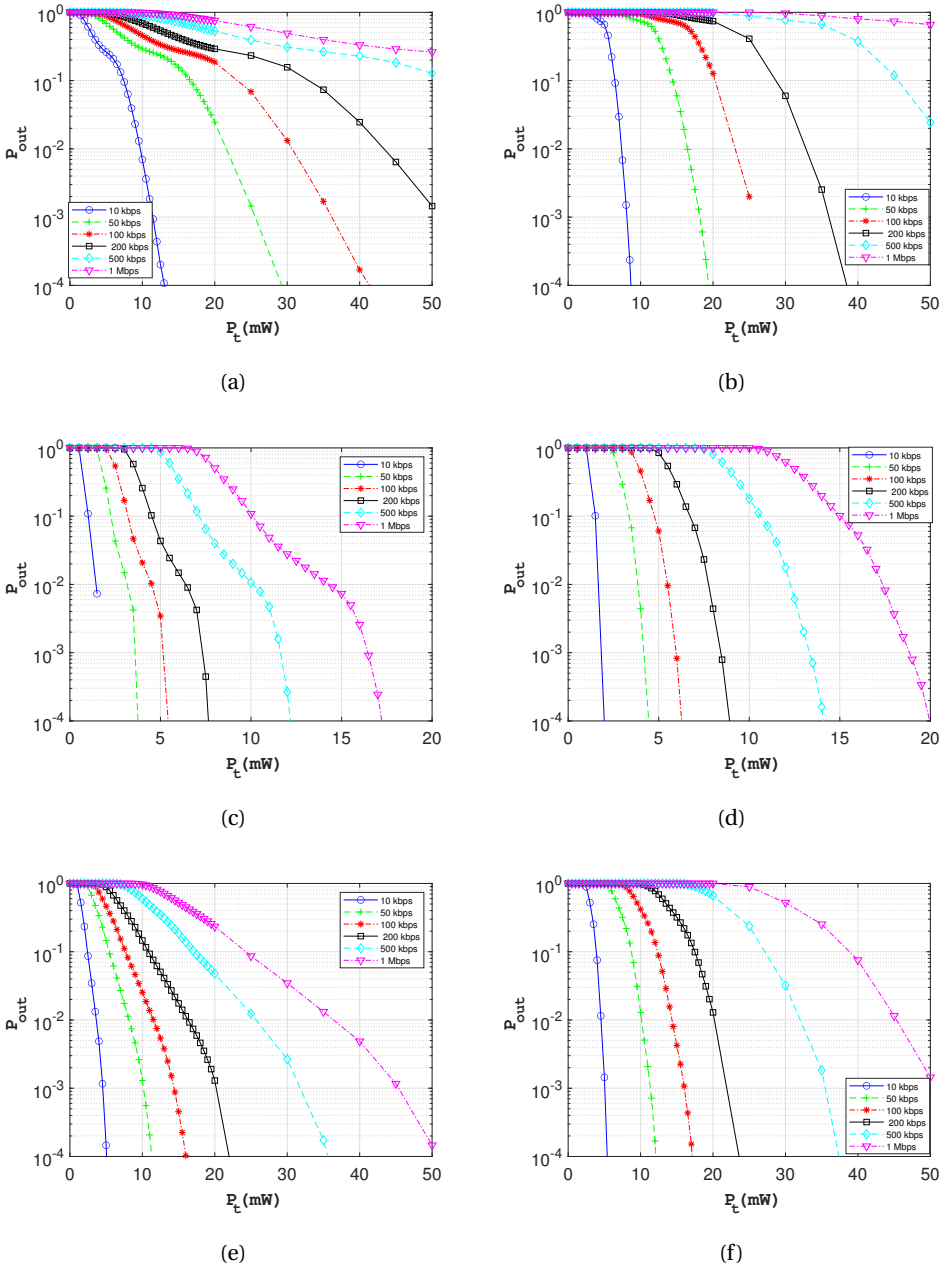

Figure 5.8 — P_{out} versus the transmit power for different data-rates for the cases of (a) CN1 and AP5, (b) CN2 and AP5, (c) CN1 and AP1-AP4 with EGC, (d) CN2 and AP1-AP4 with EGC, (e) CN1 and AP1-AP4 with SC, and (f) CN2 and AP1-AP4 with SC. Uncoded OOK modulation.

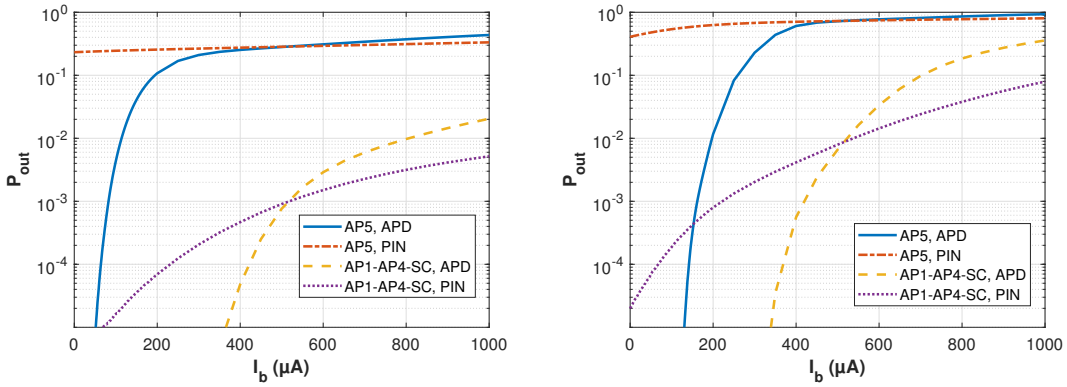

(a) (b)

Figure 5.9 — P_{out} versus background noise current I_b for PIN- and APD-based Rxs with different AP configurations. (a) CN1, (b) CN2. Uncoded OOK modulation. $P_t = 15$ mW, $R_b = 200$ kbps.

In particular, we demonstrated the benefit of using multiple-APs with EGC and SC combining strategies in improving link reliability due to the reduction of beam shadowing during user movements, which justifies the increased network implementation complexity. Placing the APs on the ceiling was found to provide a better performance, given the lower DC gain variations it offers. Also, our study revealed that the placement of the CN on the waist is more advantageous, as compared to the position on the shoulder, especially for the single AP configuration. Lastly, we investigated the use of PIN- and APD-based Rxs and showed that except under high background noise conditions, using one APD-based AP provides acceptable link performance. However, when working under moderate-to-strong background noise conditions, we would recommend using multiple PIN-based APs.

The next Chapter will focus on the design of efficient signaling schemes for managing MA requirements in intra-WBAN links.

Chapter 6

Multiple Access Management for Intra-WBAN Links

Contents

6.1 Introduction 79
6.2 TDMA 80
6.3 FDMA 82
6.3.1 MU m-CAP 82
6.3.1.1 Performance of MU m-CAP for the case of ideal channels 83
6.3.1.2 Performance of MU m-CAP for WBAN channels 84
6.4 Contention-based schemes 86
6.4.1 ALOHA 86
6.4.2 CSMA/CA 86
6.5 DQRA Scheme 88
6.5.1 DQ-MAC Description and modeling 89
6.5.1.1 DQ Scheme Design 89
6.5.1.2 Power consumption model 90
6.5.2 Performance Metrics 91
6.5.2.1 Access Delay 91
6.5.2.2 Energy Consumption 92
6.5.3 Performance analysis 92
6.6 Chapter summary 94

6.1 Introduction

When dealing with multiple users sharing the same communication channel, appropriate techniques need to be employed. These techniques share the available resources among the users,

e.g., by using time, frequency, or code division schemes. here, we distinguish between different MA schemes by classifying them into scheduled- and contention-based techniques.
Scheduled-based schemes include time-division MA (TDMA), where different time-slots are assigned to different users, frequency-division MA (FDMA), where users are allocated different frequency sub-bands, and CDMA, where users are differentiated by different codes. Concerning intra-WBAN links. Optical CDMA is not well suited for intra-WBANs due to the increased complexity and reduced efficiency for large number of users, because of the requirement of long optical orthogonal codes (OOC) [157]. Contention-based or packet radio techniques, on the other hand, such as ALOHA and CSMA/CA, can be viewed as a particular form of TDMA, where time-slots are allocated to the users in an adaptive manner. Another interesting approach that is well adapted to the context of IoT is the DQRA scheme, which separate the contention from data transmission by restricting the contention requests to short periods, as compared to the packet duration, resulting hence in a network performance improvement.
In this chapter, we briefly introduce scheduled-based and contention-based MA techniques. For this, we present briefly in Section 6.2 the main principle of TDMA protocol and its features. Then, Section 6.3 presents frequency-based MA techniques, that are adapted to OWC systems. Here, the concept of MU m-CAP scheme is presented and its performance studied for an ideal optical channel as well as intra-WBAN channels. Next, In order to introduce the DQRA scheme, we give in Section 6.4 a short overview of the contention-based MA protocols, namely, ALOHA and CSMA/CA. Afterwards, we propose to combine in Section 6.5 the DQRA scheme with MU m-CAP to provide efficient random access and data transmission capabilities for optical intra-WBAN links. Here, we first introduce the analytical model of DQ and the optical transmission system model of MU m-CAP with an emphasis on power consumption of optical transceivers. The link performance is quantified in terms of average energy consumption and average access delay. We further present a comparison between RF-based and optical-based systems as well as between single channel and multiple channel configurations. Lastly, Section 6.6 concludes the Chapter.

6.2 TDMA

In TDMA systems, the transmission frame is divided into N time slots, and each user is allocated one time slot to either transmit or receive, while using the full available bandwidth. During the remaining $N-1$ time slots, a given user remains silent and the operation is repeated periodically at each frame [158]. Figure 6.1 illustrates the concept of TDMA. The frame structure of TDMA is shown in Fig. 6.2 where it consists of a preamble, an information message, and the tail bits. The preamble contains the address and synchronization information for the CN and the SN to identify each other. The information message is composed of the N cyclically repeating time slots that are separated by guard times to account for synchronization bits of the Rxs [159] and for the propagation time of the signal through the channel. The main features of TDMA can be summarized as follows [160]:

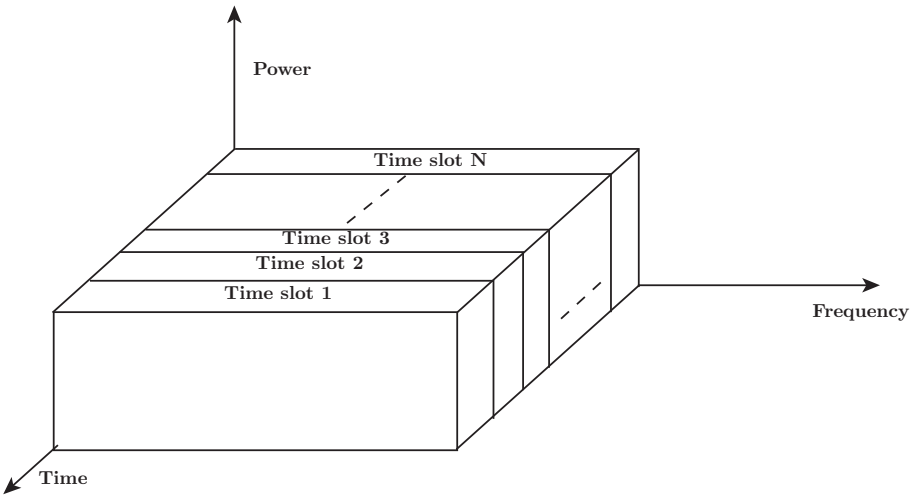

Figure 6.1 — the concept of TDMA [158].

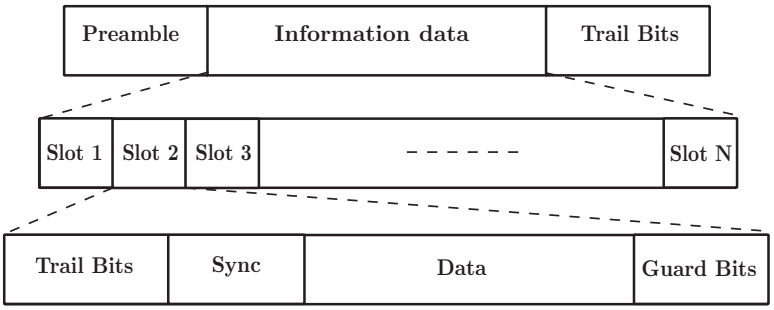

Figure 6.2 — the frame structure of TDMA [158].

- Data transmission in TDMA occurs in bursts, which allow the SNs to turn off their Tx when it is not used and hence minimizing the power consumption. Also, the discontinuous transmissions of TDMA make the handover process easier for the CNs in the case of extra-WBAN transmission, since they can listen for other APs during idle time slots and find whether they offer a better channel quality.

- TDMA systems use different time slots for transmission and reception, however, in the case of very high data-rates, there is a need to use adaptive equalization techniques, which increase the Rx complexity.

- Guard times are required for TDMA to compensate for the propagation time of the signal between the coordinator and the end users and also to compensate for the rise time of Tx modules. The guard time should be kept to the minimum without causing sharp suppressions of the signal at the edge of the time slots and thus avoiding spectrum expansion and inter-channel interference (ICI).

- TDMA systems require a high synchronization overhead because of burst transmissions, as synchronization and channel estimation might be needed for each time slot. The duration

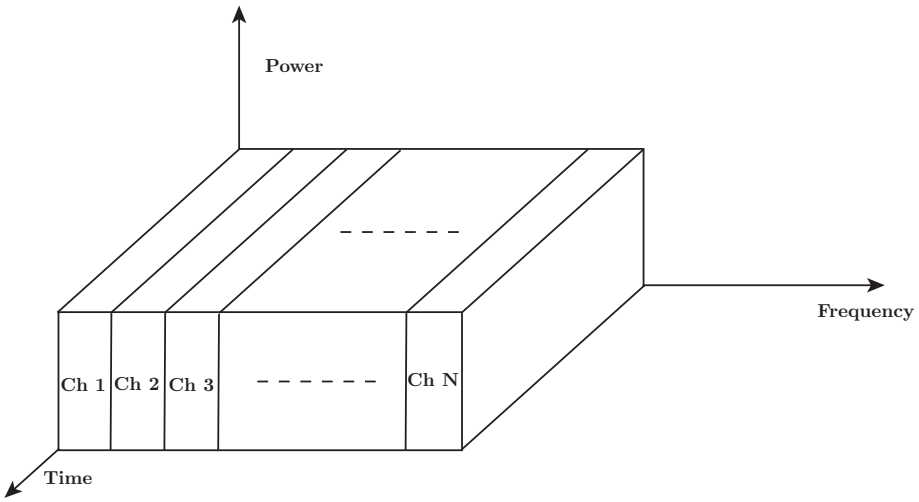

Figure 6.3 — the concept of FDMA.

of the time slot has a strong effect on the system performance. If it is too short, the synchronization overhead becomes important and if it is too long, the transmission delays become very large and the channel might change during one time slots, necessitating a new channel estimation. In addition, guard slots are necessary to separate users.

- The time slots in TDMA can be allocated dynamically to the SNs, where each SN can be allocated a different number of time slots per frame based on a given prioritization scheme.

6.3 FDMA

Frequency-based MA techniques such as FDMA assigns different frequency sub-bands, to different SN. Figure 6.3 illustrates the main concept of FDMA. FDMA systems needs only a few bits for synchronization overhead, compared to TDMA due to the continuous transmission nature of the scheme [158, 160]. A convenient way of implementing FDMA is through the use of optical OFDM; what is usually called optical orthogonal frequency-division MA (OFDMA). Given the practical issues encountered with optical OFDMA, in particular, the relatively high signal PAPR, and given that the required data-rates in medical WBAN systems is relatively low, we exclude here the case of optical OFDMA. Instead, we consider a simpler FDMA scheme, based on m-CAP, as described in the following.

6.3.1 MU m-CAP

As described in Chapter 2, the concept of m-CAP is to divide the signal bandwidth into m independent sub-bands using FIR filters, where the modulation order and the transmit power can be set independently for each sub-band. In MU m-CAP, one or multiple sub-bands are allocated to

each user. That is, users that need higher data-rates or experience a low quality of received signal can be dynamically allocated more sub-bands to improve their performance.
The block diagram of MU m-CAP is shown in Fig. 6.4. At the Tx, data streams of each n user are divided among the allocated sub-bands of the corresponding user. The m streams symbols are mapped on their corresponding QAM mapper, with the corresponding modulation order. The mapped symbols are then up-sampled and decomposed to their in-phase (I) and quadrature (Q) components, which are then filtered with SRRC filters at different frequencies depending on the sub-band number (see Fig. 6.4(a)). Each component of the sum represents a sub-band that can be assigned to a user. The CIR of the SRRC filter $g_{\text{SRRC}}(t)$, along with the I/Q filters are given below [161].

$$\begin{aligned} g_{\text{SRRC}}(t) &= \frac{\sin\left(\pi(1-\beta)\frac{t}{T_s}\right) + 4\beta\frac{t}{T_s}\cos\left(\pi(1-\beta)\frac{t}{T_s}\right)}{\pi\frac{t}{T_s}\left(1-\left(4\beta\frac{t}{T_s}\right)^2\right)}, \\ h_I^n[t] &= g_{\text{SRRC}}(t)\cos\left(\pi\frac{t}{T_s}(2n-1)(1+\beta)\right), \\ h_Q^n[t] &= g_{\text{SRRC}}(t)\sin\left(\pi\frac{t}{T_s}(2n-1)(1+\beta)\right), \end{aligned} \tag{6.1}$$

where $0 < \beta < 1$ is the SRRC roll-off factor, T_s denotes the symbol duration, and n is the index of the sub-carriers. Note that β is kept the smallest possible in order to increase the spectral efficiency.
The up-sampling is done by means of zero-padding, where the number of zeros/symbol is given by [162]:

$$n_s = 2\left\lceil 2m(1+\beta)\right\rceil, \tag{6.2}$$

where m is the number of sub-bands and $\lceil\cdot\rceil$ is the ceiling function.
The total signal S of the m-CAP system is expressed by:

$$S_{\text{tot}}(t) = \sum_{n=1}^{m} s^n(t) = \sum_{n=1}^{m}\left[s_I^n(t) \circledast h_I^n(t) - s_Q^n(t) \circledast h_Q^n(t)\right], \tag{6.3}$$

where $s_I^n(t)$ and $s_Q^n(t)$ are the I/Q components of the signal of the n^{th} user denoted by $s^n(t)$.
At the Rx side of user n, the down-sampled I/Q components for each of the user's assigned sub-bands are recovered using the matched filters $g_I^n(t) = h_I^n(-t)$ and $g_Q^n(t) = h_Q^n(-t)$, as illustrated in Fig. 6.4(b). The recovered data stream is obtained after recombining the de-mapped symbol streams.

6.3.1.1 Performance of MU m-CAP for the case of ideal channels

Let us limit our study here to the case of CN1 and consider first the case of an ideal channel, i.e., $H_0 = 1$, for all links from CN1 to SNs. Let us consider the scenario, where a patient wearing an intra-WBAN and walking inside a hospital room. Consider an uplink scenario with 10 users, $m = 10$, and $\beta = 0.1$. We assume that each SN transmits at a data-rate of 1 Mbps with a binary phase shift keying (BPSK) modulation and occupying each a sub-band of 1.1 MHz. The resulting total system

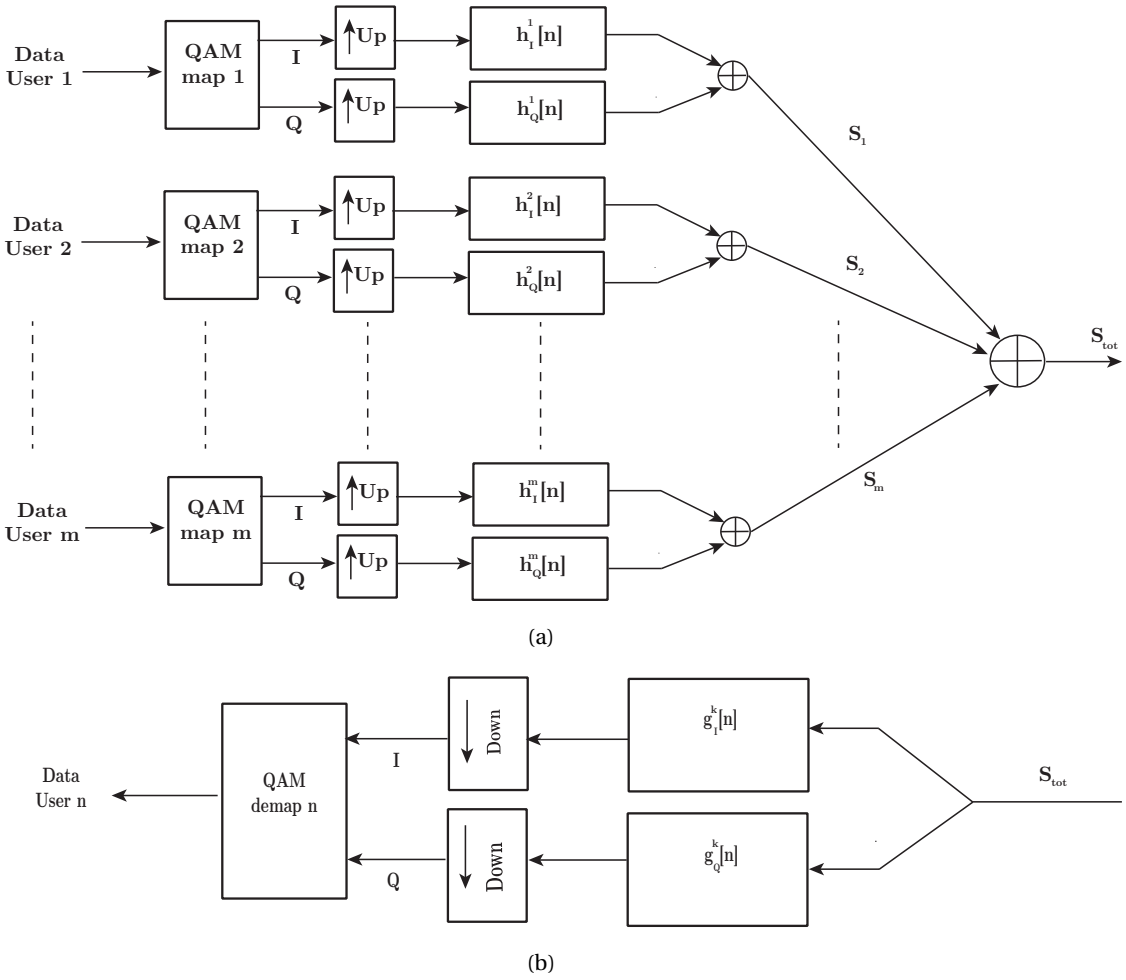

Figure 6.4 — the concept of MU m-CAP: (a) the Tx and (b) the Rx.

bandwidth is 11 MHz. In order to study the effect of limited LED modulation bandwidth, we set the LED cut-off frequency to 2 MHz. Figure 6.5 illustrates the BER versus SNR performance for such a configuration. We observe a degradation of performance with increased sub-band index. For instance, the SNR to achieve a target BER of 10^{-3} is 16, 21, and 26 dB for the sub-bands 3, 6, and 10, respectively. This can be explained by the low pass characteristics of the LED, which results in an SNR penalty at higher frequencies. Note that this problem can be addressed in part by bit and power loading.

6.3.1.2 Performance of MU m-CAP for WBAN channels

Now consider the case of practical WBAN channels, where SNs transmit at a fixed data-rate of 100 kbps with BPSK modulation, resulting in a total bandwidth of 1.1 MHz. Also, we consider PIN-based Rx and take into account thermal noise with load resistance of $R_L = 50\,\Omega$ and relatively high background noise level with $I_b = 100\,\mu$A. Here we do not consider any LED bandwidth limitations as IR LEDs have a cut-off frequency of about 20 MHz. Figure 6.6 illustrates the outage probability

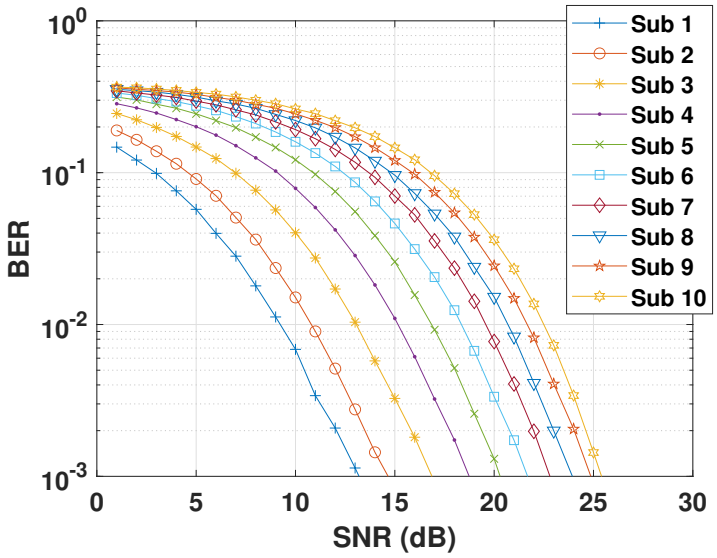

Figure 6.5 — BER vs SNR performance for MU 10-CAP system. Sub stands for sub-band.

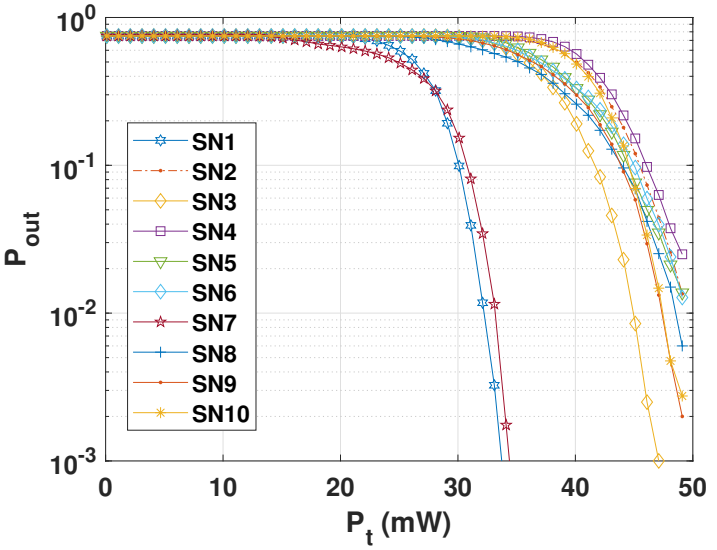

Figure 6.6 — P_{out} vs P_t performance for MU 10-CAP system.

performance considering a BER of 10^{-3}. We notice that, generally, the sub-bands are affected by the mobility and shadowing from each SN-CN link. For instance, for SN3 and SN5 (placed on the chest and left arm, respectively), the former link achieves a better performance. We observe the same trend between SN2 and SN4 links. Generally, the same conclusions and observations can be drawn as for subsection 4.4.3.

6.4 Contention-based schemes

In contention-based or packet radio (PR) access schemes, end users (i.e., SNs here) use bursts of data to try to access the same channel in an non-or minimal-coordination way. The CN then will detect the potential collisions that may occur from the simultaneous transmissions from multiple users and send back either an acknowledgment (ACK) or negative acknowledgment (NACK) signal to inform the end users whether the transmission was successful or not [163]. Contention-based MA schemes benefit from a rather easy implementation, at the cost of relatively low spectral efficiency and induced random delays due to the possible collisions. Meanwhile, they can serve a large number of users with a low overhead.
The basic contention-based protocol is ALOHA, which was developed for early satellite systems. In ALOHA, end users transmit on the common channel whenever they have data to send, and then wait for the acknowledgment feedback from the CN to determine the status of the transmission. In the case of a collision, the user waits for a random time period, and then re-transmits the packet. In this section, we will briefly describe the two main contention-based protocols which are ALOHA and CSMA/CA.

6.4.1 ALOHA

When the Tx chooses randomly the time at which it starts its packet transmission, we call the system a pure or unslotted ALOHA [164].
Pure ALOHA suffers from a large delay and a high probability of collisions when the number of users is large. Figure 6.7 shows an example of two Txs transmitting packets using pure ALOHA. Here a short collision is assumed to cause enough interference such that the Tx will need to retransmit the packet. Packet A transmitted by Tx2 can suffer from collisions with packets transmitted by Tx1 either at the start or at the end of the transmission. For a packet of duration T_p, collisions are avoided if, Tx1 starts its packet transmission at least T_p seconds before packet A, or starts its transmission after packet A has finished. Therefore, the total collision-sensitive time is $2\,T_p$. The maximum effective throughput is $1\,/\,(2\,e)$, where e denote the Euler number.

In a slotted ALOHA system, time is divided into slots of length larger than T_p. Each Tx has a synchronized clock to ensure that packets are transmitted only at the beginning of a time slot. Figure 6.8 shows an example of two Txs using slotted ALOHA. We notice that synchronization prevents partial collisions, encountered in pure ALOHA, and restricts them to complete collisions that occur only when more than two Txs transmits simultaneously. The maximum achievable throughput $1\,/\,e$ which is twice that of pure ALOHA.

6.4.2 CSMA/CA

In ALOHA protocols, explained above, a Tx sends its packets without listening to the channel state to check whether or not other Txs are transmitting. Collisions can be avoided more efficiently if

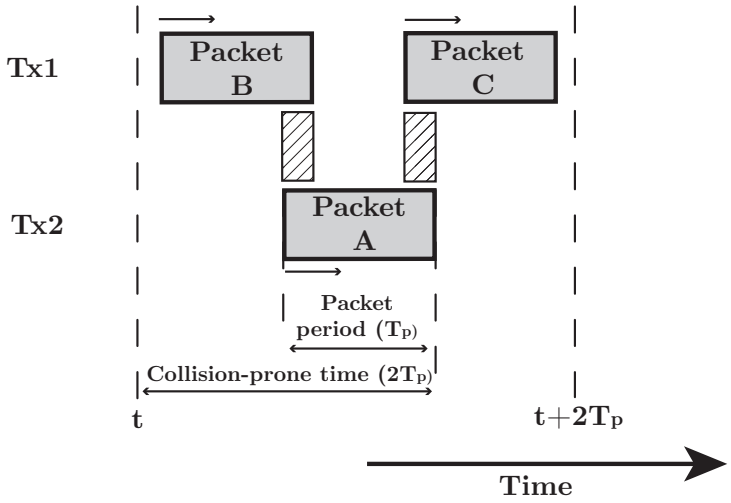

Figure 6.7 — The concept of pure ALOHA [160]. Two Txs are transmitting using pure ALOHA. Here, packets will collide as Tx1 started its transmission before Tx2 ended transmitting.

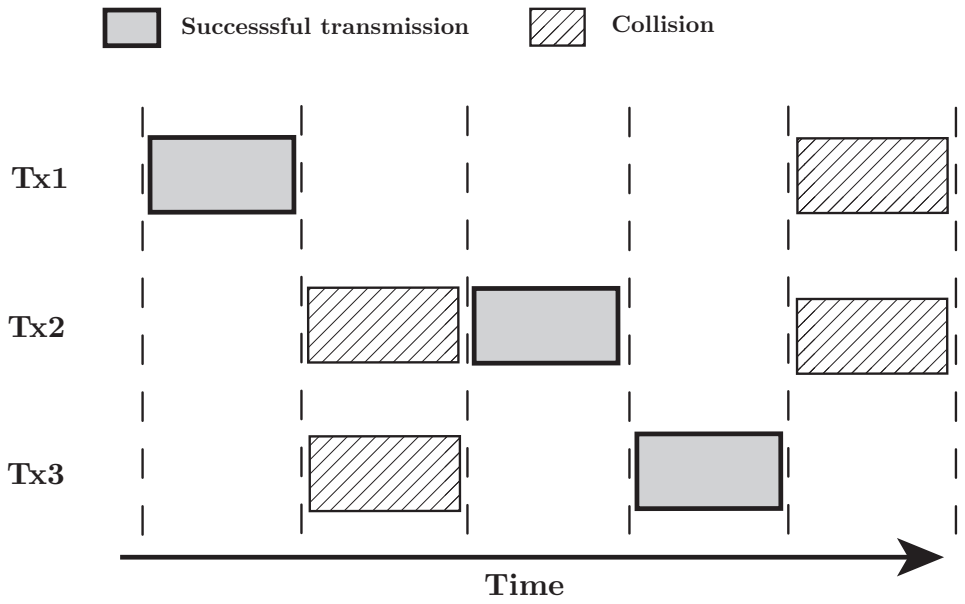

Figure 6.8 — The concept of slotted ALOHA. By allowing users to transmit only at the beginning of a slot, collisions are restricted to only when the Txs transmit simultaneously.

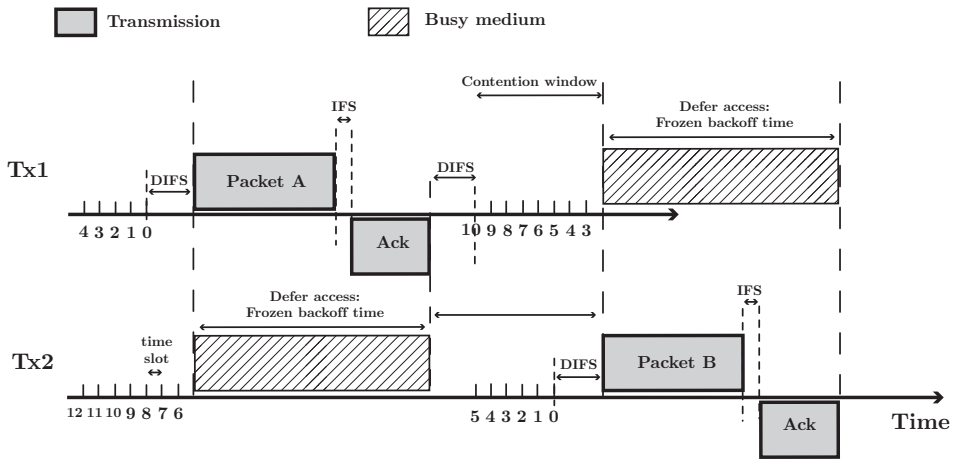

Figure 6.9 — The concept of CSMA/CA [163].

the Txs listen to the channel before they start transmitting their packets, which is the main concept behind CSMA/CA. This way, if the channel is found to be idle for a short period of time, called distributed inter-frame space (DIFS), the Tx will transmit its data. Otherwise, if the channel is sensed to be busy during the DIFS, the Tx defers its transmission and continues to sense the channel until finds it to be idle for a DIFS. Then, the Tx waits for a random back-off time, generated within an interval $[0, CW]$, before packet transmission (collision avoidance), where CW refers to the contention window. The latter will minimize the probability of collisions on the channel. Note that during the defer access period, the Tx will freeze its back-off time until the channel is sensed as idle. As for ALOHA, CSMA/CA can be either slotted or unslotted. Figure 6.9 illustrates the functioning of the CSMA/CA scheme.

There are two important parameters that could impact the performance of CSMA/CA protocols, which should be kept much smaller than the packet duration, detection and propagation delays. Detection delay is the time required for a Tx to sense the state of the channel and is related to the Tx hardware. Propagation delay, on the other hand, is a measure of the time it takes for a packet to travel from the Tx to the Rx.

6.5 DQRA Scheme

MAC-layer schemes such as CSMA/CA are not energy efficient enough, while scheduled-based protocols such as TDMA are not spectrally efficient enough, given the heterogeneous traffic of medical sensors [165]. These considerations motivate the investigation of DQ protocols, which can efficiently reduce both access delay and energy consumption, and cope with the heterogeneous traffic type that characterizes medical networks. DQRA was first introduced and analyzed in [166–169] for the context of RF transmission. For instance, a DQ-MAC protocol was proposed in [170] for medical applications and its energy analysis was considered in [171]. Also, a DQ-MAC with multiple transmission channels was proposed with a multiple-input multiple-output

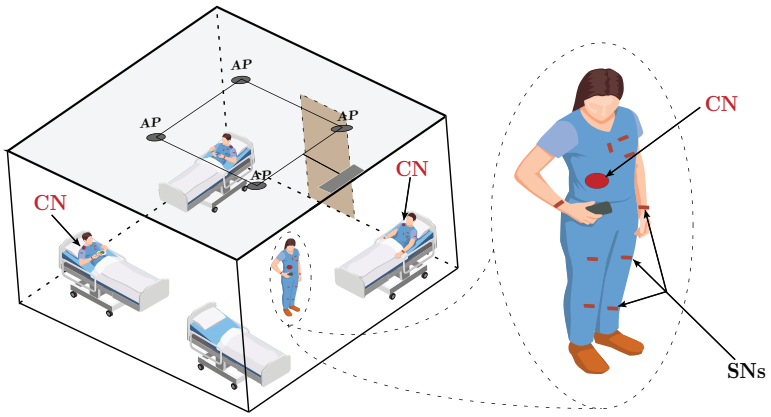

Figure 6.10 — The considered network architecture.

(MIMO) adaptation for massive M2M applications in [172], and in the context of WBANs in [173]. In what follows, we propose DQRA for optical WBAN, which is, to the best of our knowledge, the first introduction of DQ schemes to the context of OWC.

6.5.1 DQ-MAC Description and modeling

We describe here the main concept of DQ-MAC scheme and the proposed architecture for the case of optical WBANs.

6.5.1.1 DQ Scheme Design

Figure 6.10 recalls the considered network architecture. Multiple SNs are connected in a star topology to the CN, where each SN is assumed to generate a Poisson distributed traffic of average rate λ and exponentially distributed message length of average $(1/\mu)$. The basic idea of DQ-MAC is to restrict the users contention to short access requests while keeping the main part of the frame to the transmission of data packets. The frame structure of DQ-MAC is composed of three parts as illustrated in Fig. 6.11: a contention resolution window (CRW) that is divided into M contention resolution (CR) mini-slots for the transmission of access request sequences (ARS); a contention-free data transmission window (DTW); and a feedback window for downlink feedback packet (FBP) from the CN. The CRW is organized sequentially in time division duplexing (TDD) mode, while DTW is organized in frequency division duplexing (FDD) mode using MU m-CAP. The FBP is composed of three parts, a data ACK sequence, a preamble sequence for the purpose of synchronization for power saving [170], and a contention feedback (CF) sequence describing the status of each CR.

Figure 6.12 illustrates the system model of the proposed multichannel DQ scheme. It consists of three subsystems: the new-user access control (NAC), the contention resolution, and the data transmission subsystems. The algorithm of DQ-MAC works as follows: The NAC will prevent newly arrived SNs to contend for CRs until the resolution of all previous collisions. Then, at the start of a new frame, SNs with data to send and which have not sent an ARS yet, will randomly choose one of

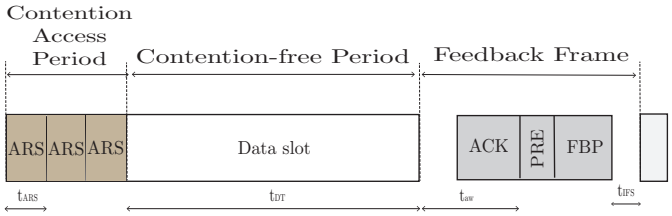

Figure 6.11 — DQ frame structure.

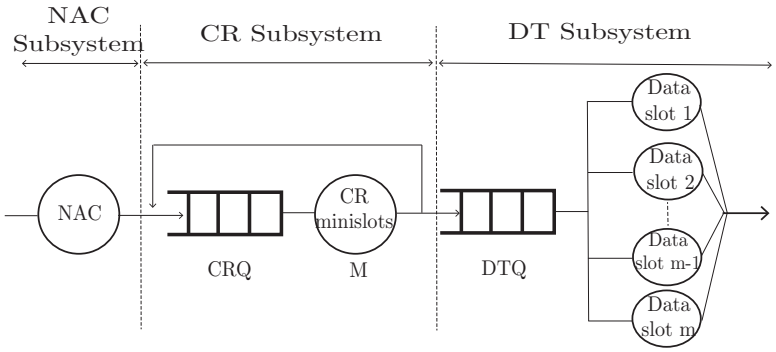

Figure 6.12 — Multichannel DQ-MAC model.

the M available CRs for their ARS. Depending on the reception status at the CN side, SNs will enter either the contention resolution queue (CRQ) if a collision was detected in their selected CR, or the data transmission queue (DTQ) if their ARS was transmitted correctly. This information is notified to the SNs in the FBP at the end of the frame [164]. For SNs that enter the CRQ, a tree-splitting algorithm is used to resolve the contentions [167]. On the other hand, SNs that successfully enter the DTQ will be allowed to transmit their data in a first-in first-out (FIFO) discipline, where up to m SNs can transmit within a single DTW on the available m sub-bands provided by the MU m-CAP.

6.5.1.2 Power consumption model

A major difference between optical and RF systems resides in the front-end architecture, which impacts power consumption accordingly. For the sake of comparison, two cases of RF- and OWC-based networks are considered. The RF network uses a ZigBee tranceiver, while the OWC network uses an Infrared Data Association (IrDA) tranceiver. Table. 6.1 presents the power consumption P_{tx}, P_{rx}, and P_{idle}, corresponding to the transmit, receive, and idle modes, respectively.

Table 6.1 — Power consumption (in mW) of optical and RF transceivers.

TRx	P_{tx}	P_{rx}	P_{idle}
Optical [174]	40	0.5	0.3
RF [175]	22.09	35.23	0.712

6.5.2 Performance Metrics

The multichannel DQ scheme can be statistically modeled with an M/M/1 and M/M/m queuing systems to represent the CRQ and DTQ, respectively [168]. As was mentioned in subsection 6.5.1.1, the input rate of packets follows a Poisson distribution with mean λ. Also, the service time of the CRQ μ_{rq} can be expressed as a function of λ as:

$$\mu_{rq} = ln\left(\frac{1}{(1-P(\lambda))}\right), \tag{6.4}$$

where $P(\lambda) = e^{-\lambda/M}$ is the probability of successful access to a CR slot [168].
Last, the departure rate of the CRQ is equal to λ in stable conditions. Similarly, the input rate of the DTQ is the same as the output rate of CRQ which is λ, and the service time of the DTQ is:

$$\mu_{dq} = T_1/\mu, \tag{6.5}$$

where $1/\mu$ is the mean message length as previously mentioned in subsection 6.5.1.1 and T_1 is the mean transmission time for each packet of the message. Defining p as the probability of packet error transmission (PER), we have [169]:

$$T_1 = (1-p)\sum_{n=1}^{\infty} n\,p^n = \frac{1}{1-p}. \tag{6.6}$$

6.5.2.1 Access Delay

The average delay an SN will spend in the DQ system to transmit its packets is the sum of the average delays of each subsystem:

$$E[t] = E[t_{NAC}] + E[t_{CRQ}] + E[t_{DTQ}], \tag{6.7}$$

where $E[t_{NAC}]$ is the average service time of the NAC subsystem which is distributed uniformly in the interval $[0, 1]$, i.e., $E[t_{NAC}] = 0.5$. $E[t_{CRQ}]$ is the average delay of the CRQ subsystem, and $E[t_{DTQ}]$ average delay of the DTQ subsystem. $E[t_{CRQ}]$ can be calculated from the response time of M/M/1 queuing system, which is [176]:

$$E[t_{CRQ}] = \frac{1}{\mu_{rq} - \lambda}, \tag{6.8}$$

and similarly, $E[t_{DTQ}]$ can be calculated from the response time of M/M/m queuing system as [176]:

$$E[t_{DTQ}] = \frac{1}{\mu_{dq}} + \frac{P_m}{m\,\mu_{dq}(1-\rho_{dq})}. \tag{6.9}$$

In (6.9), $\rho_{dq} = \lambda/(m\,\mu_{dq})$ is the utilization factor and P_m is the Erlang C formula of the delay probability, which is expressed for an M/M/m queuing system as [176]:

$$P_m = \frac{(m\,\rho_{dq})^m}{m!\,(1-\rho_{dq})}\left[\frac{(m\,\rho_{dq})^m}{m!\,(1-\rho_{dq})} + \sum_{k=0}^{m-1}\frac{(m\,\rho_{dq})^k}{k!}\right]^{-1}. \tag{6.10}$$

6.5.2.2 Energy Consumption

Following the analysis in [171], the average consumed energy per information bit $E[\gamma_{\text{bit}}]$ can be derived from $E[t_{tx}]$, $E[t_{rx}]$, $E[t_{idle}]$ the average time the SN spend in transmit, receive, and idle modes, respectively, as follows:

$$E[\gamma_{\text{bit}}] = \frac{P_{tx}E[t_{tx}] + P_{rx}E[t_{rx}] + P_{idle}E[t_{idle}]}{L}, \tag{6.11}$$

where:

$$E[t_{tx}] = E[N_{ARS}](t_{ARS} + t_{ia}) + E[T_{DT}] + t_{ia}, \tag{6.12a}$$

$$E[t_{rx}] = E[N_{wait}](t_{PRE} + t_{FBP} + t_{ia}) + t_{ACK}. \tag{6.12b}$$

$$\begin{aligned} E[t_{idle}] = {} & E[N_{wait}](E[t_F] - (t_{ARS} + t_{ia} + t_{PRE} + t_{FBP})) + \\ & E[N_{ARS}](E[t_F] - (t_{ARS} + t_{ia} + t_{PRE} + t_{FBP})) + (E[t_F] - (E[t_{DT}] + t_{PRE} + t_{FBP}. \end{aligned} \tag{6.13}$$

Here, $E[N_{ARS}]$ and $E[N_{wait}]$ are the average number of time frame before transmitting a successful ARS and the time the SNs wait in the whole DQ system, respectively. They are expressed as:

$$E[N_{wait}] = E[t] - (E[N_{ARS}] - 1) - m\rho_{dq}, \tag{6.14a}$$

$$E[N_{ARS}] = \sum_{i=1}^{\infty} \left[i\, e^{-\lambda/M^i} \prod_{j=1}^{i-1} (1 - e^{-\lambda/M^i}) \right]. \tag{6.14b}$$

Moreover, $E[t_{DT}]$ is the average data length and t_F is the frame length, which is expressed as:

$$t_F = M\, t_{ARS} + t_{DT} + t_{aw} + t_{PRE} + t_{FBP} + t_{IFS}. \tag{6.15}$$

Here, t_F is the frame duration, t_{ARS}, t_{DT}, t_{aw}, t_{ACK}, t_{PRE}, t_{FBP}, t_{IFS} and t_{ia} are illustrated in Fig. 6.12

6.5.3 Performance analysis

Table 6.2 — Simulation parameters [171].

Parameter	Value	Parameter	Value
Headers	15 bytes	t_{aw}	864 μs
Data rate	250 kbps	t_{IFS}	192 μs
Payload	20-120 bytes	PRE+FBP	4+11 bytes
ACK	11 bytes	M	3
Beacon	11 bytes	t_{ARS}	128 μs

Figure 6.13 shows the simulation results using MAC parameters from [171, Table 1], and considering an ideal channel (i.e., with no packet loss due to transmission). For the sake of comparison, two cases of RF- and OWC-based networks are considered. Power consumption in transmit, receive, and idle modes are respectively set to 22.09, 35.23, and 0.712 mW for the RF transceiver

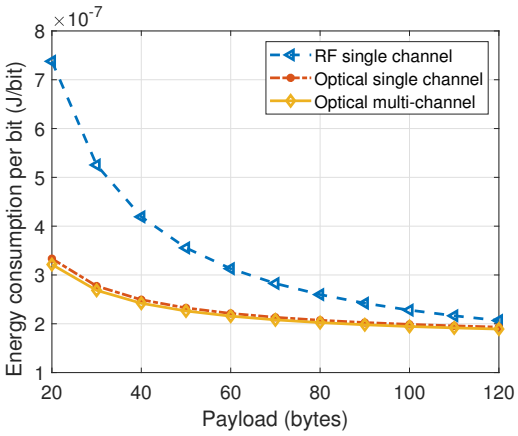

(a)

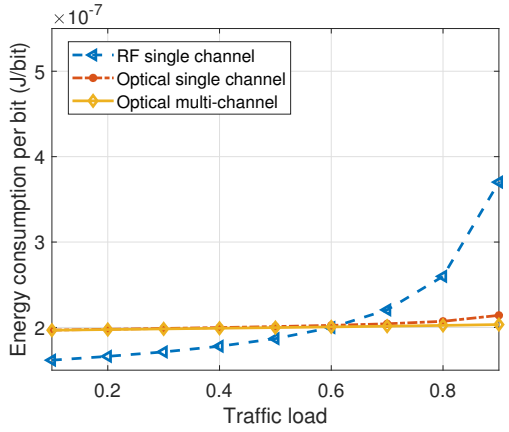

(b)

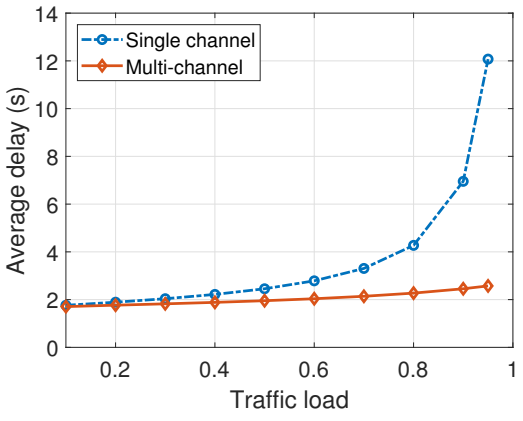

(c)

Figure 6.13 — (a) Energy consumption vs. payload length for $\lambda = 0.8$, (b) energy consumption vs. traffic load, (c) average delay.

(ZigBee), and 40, 0.5, 0.3 mW for the OWC transceiver (IrDA), as it is shown in Table. 6.1. From Fig. 6.13(a), we notice the decrease in energy consumption of DQ schemes for the cases of RF and single channel (OOK) and multichannel (10-CAP) OWC, assuming a traffic load of $\lambda = 0.8$ packets/frame. OWC allows a reduced energy consumption for payloads shorter than 120 bytes. From Fig. 6.13(b), interestingly, energy consumption does not increase considerably with increase in λ for OWC-based systems. Nevertheless, the RF-based system has a lower energy consumption for $\lambda \lesssim 0.6$. In fact, the energy consumption of OWC-based systems is higher in the transmit mode, but much lower in the receive and idle modes. For large λ, SNs will spend most of the time in idle/receive modes. Lastly, Fig. 6.13(c) shows the improvement in terms of average delay using m-CAP.

6.6 Chapter summary

In this Chapter, we presented different families of MA schemes, that we classified into scheduled- and contention-based techniques. Scheduled-based schemes include TDMA where different time-slots are assigned to different users, FDMA where users are allocated different frequency bands, and CDMA where users are differentiated by different codes. Contention-based or packet radio techniques such as ALOHA and CSMA/CA which can be viewed as a particular form of TDMA, where time-slots are allocated adaptively.
As MAC-layer schemes such as CSMA/CA are not energy efficient enough, while scheduled-based protocols such as TDMA are not spectrally efficient enough for WBAN links, DQRA was proposed. In order to manage the MA requirement, DQ in the MAC layer together with m-CAP transmission was proposed and its efficiency shown through numerical results. Future research will investigate the proposed scheme with realistic optical WBAN channel models, as well as its performance evaluation under heterogeneous traffic conditions.

Chapter 7

Conclusions and Perspectives

Contents

7.1 Conclusions **95**

7.2 Perspectives **97**

7.1 Conclusions

WBANs have recently received increasing attention thanks to the advances made in the very large-scale integration of sensors and actuators. In medical applications, WBANs can be used for real-time vital signs remote monitoring of patients in health-care centers and elderly people at home. Within this context, optical WBAN is a promising technology to cope with the interference and data security issues of RF-based solutions. OWC has the advantages of immunity to external interference, inherent security due to the indoor confinement of light, and a negligible small-scale fading effect. However, to asses the impact of body shadowing and mobility on the optical WBAN channel and to develop appropriate MA schemes that satisfy the requirements of WBANs, a dedicated study is needed. To address these issues, we focused in this thesis on developing realistic channel models that account for body local and global mobility for intra- and extra-WBANs, as well as the design of efficient, low energy, low complexity MA schemes.

After a general introduction to OWC systems in **Chapter 2**, we proposed in **Chapter 3** a new channel modeling approach based on MCRT, to characterize the optical WBAN channel. We explained the theoretical principles behind the MCRT approach, RWP mobility, and statistical channel characterization. Then, we validated the results obtained with the proposed method against results from the literature. We also discussed the statistical characterization of dynamic channels using best-fit and kernel density estimates, and outage probability calculation. Lastly, we explained how to configure the simulation for intra- and extra-WBAN scenarios, in particular, regarding 3D environment specifications, local and global mobility modeling, as well as sensor placement.

In **Chapter 4**, we focused on channel modeling and performance analysis of intra-WBANs links. We provided useful insights into the effects of local and global user mobility and their corresponding beam shadowing effects. These effects were investigated using a realistic dynamic model based on a 3D animation of the walk cycle and a modified RWP mobility. After specifying the simulation parameters for a practical implementation of a medical WBAN, we presented simulation results based on Opticstudio software on the temporal evolution of the channel DC gain, delay spread, and coherence time, as well as on their statistical distribution for the underlying intra-WBAN links. The latter is particularly helpful for studying the channel behavior and consequently, the link performance for physical or upper layer design. We showed that body positions and orientations inside the room have a high impact of on the variations of the channel gain. Intra-WBAN links' statistics can be best modeled with a Gamma or Nakagami distribution. They also have slower time variations (typical coherence times of a few seconds), compared to the RF counterparts (coherence times of tens of ms). These slow time variations allow using larger packet sizes for the former, thus a lower pilot overhead and a simplified power control over successive frames. Last, optical channels can be considered as effectively flat for low-to-moderate data-rates. Next, based on KDE statistical characterization, we evaluated the link performance for a simple NRZ-OOK modulation scheme based on the outage probability criterion, given the random time-varying nature of the channel. We evaluated the performance of PIN and APD Rxs in different background noise conditions. Concerning the link reliability, it is significantly affected by shadowing resulting from local body mobility, which also depends on the position of the CN. We concluded also that, given the constraints on the system complexity and power consumption, a PIN-based Rx (CN) is a suitable choice.

Similar to the study conducted in **Chapter 4**, we studied the extra-WBAN channel and evaluated its performance in **Chapter 5**. Meanwhile, we investigated the benefit of using multiple APs in the room. Results for the main channel metrics presented previously and outage probability analysis for PIN- and APD-based Rxs were provided and the impact of noise was discussed. We proposed a KDE based on Gaussian kernels for the extra-WBAN channels and showed that using an APD at the Rx (AP) is an appropriate choice except under strong background noise conditions. This allows increased robustness against shadowing by using a more sensitive PD, as well as reduced required IR power level at the Tx (CN). Lastly, we showed that the extra-WBAN link reliability can be significantly improved by using multiple APs, which is due to a significant reduction of beam shadowing during user movements. Although the use of multiple APs increases the implementation complexity of the network, it can be justified given the achieved performance improvement, in particular, regarding the substantial reduction of the required transmit power.

After studying the intra- and extra-WBAN channels and evaluating their performance, we focused in **Chapter 6** on the MA techniques. Given the potentially large number of SNs that could be used for each patient, developing a robust MA schemes in the PHY layer is quite challenging. More efficient MA management can be achieved through the MAC layer by minimizing packet collisions and their scheduling to ensure acceptable energy consumption and access delay. After providing

a general overview of PHY and MAC layer solutions, we considered the use of frequency multiplexing schemes such as MU m-CAP and showed their performance considering realistic WBAN channels obtained in Chapter 4. Next, we proposed the use of multi-channel DQRA scheme for energy-efficiency, seamless access to the channel, and flexibility to cope with heterogeneous data traffic. After presenting the system model of optical DQRA scheme, we provided an analytical analysis of the main metrics such as access delay and energy consumption. Last, we presented a comparison showing the performance improvement when using the multi-channel DQRA scheme compared to a single channel DQRA and compared to an RF system.

7.2 Perspectives

This thesis was devoted to a comprehensive study of the optical WBAN channel and the corresponding appropriate MA schemes. The main part of the thesis objectives presented in Chapter 1 were attained during the course of this work. However, due to time limitation, some research directions still remain to be investigated as a future extension of this work.

To accurately model the mobility and shadowing effects of the body, we considered an animation based 3D body walk cycles and walk trajectories based on an improved RWP mobility model. Future work could consider the use of MoCap methods to account for more realistic mobility models such as when the patient is sitting or sleeping. Also, more complex configurations with the effects of furniture and obstacles inside the hospital room need to be investigated. Medical devices and standard bedroom furniture could be taken into account to estimate the average induced fading caused by these obstacles. Another possible consideration is the effect of presence of other patients and medical staff in the room. This would add a random shadowing component that needs to be statistically estimated. Concerning extra-WBAN links, when the size of the room is too large, it would be interesting to study the use of multi-cell configurations. Suitable handover techniques that satisfy the low latency, low complexity requirements of WBANs will then be needed. On the other hand, in this study, we considered simple Tx/Rx models composed of one LED/PD element. This results in a limited LOS link availability, where the link relies mostly on diffuse propagations, which increases the required transmit power to satisfy a given SNR threshold. An interesting solution might be the use of omni-directional Tx/Rx, which can be done through the use of spatial diversity schemes or using MIMO techniques. This will obviously increase the hardware complexity and cost, but, this could change with the ongoing miniaturization of electronic components.

Concerning MA schemes, we proposed the use of MU m-CAP for more resource sharing efficiency for data transmission, and DQRA as a low-power, low-delay, and low-complexity MAC MA scheme. The next step is to investigate the proposed scheme with realistic optical WBAN channel models, as well as its performance evaluation under heterogeneous traffic conditions. In order to manage the MA requirements, DQ in the MAC layer together with m-CAP transmission can be investigated and its efficiency shown through numerical results through discrete-event simulations

using Omnet++ software. Also, future work can consider a combination of contention-based and multiple sub-carrier modulation schemes, similar to the random access OFDMA scheme, used in IEEE 802.11.ax for WiFi 6. Another point would be the investigation of multi-hop relaying schemes in optical WBANs to improve link reliability and robustness, reduce energy consumption and latency. Occupy COW algorithm which was first proposed for the context of RF technology could be adapted to optical WBAN [177].

As for experimental studies, experiments in NLOS scenarios using sensitive optical Rxs can be carried out. It would be also interesting to measure the DC channel gain in order to validate the analytical models proposed in this thesis. Here again, representing the mobility of the user and the potential obstacles that may exist will be the main issue. For this, the designed Tx/Rx front-ends should not be bulky to facilitate their wearing and to account for mobility. Another possible direction is to evaluate some of the proposed multiple access schemes proposed here and possibly the multi-hop relaying solutions.

Appendix A

A.1 Angles range of variation for each node

We provide here the minimal and maximal variations of ϕ and θ for each node. These are summarized in Table A.1.

Table A.1 — Range of variation of ϕ and θ for each sensor and coordinator nodes.

Node	$\phi(^\circ)$		$\theta(^\circ)$	
	min	max	min	max
SN1	22.83	22.84	11.95	11.95
SN2	-4.77	-3.03	84.77	85.17
SN3	73.79	77.89	33.39	38.45
SN4	57.05	103.72	60.16	77.83
SN5	47.23	121.15	33.53	48.41
SN6	46.19	114.3	11.23	40.33
SN7	10.77	11.11	-8.92	-4.33
SN8	95.56	97.58	-46.49	-21.59
SN9	65.64	130.59	-26.66	-22.93
SN10	71.15	150.27	-24.49	-23.96
CN1	11.63	17.96	-15.77	-4.72
CN2	93.74	96.30	-23.34	5.98

A.2 Detailed description of channel time variations for the cases of local and global mobility

A.2.1 Local mobility case

For the results presented in Fig. 4.2, the time variations of H_0 depend on the movement pattern of the body parts. We can explain these variations based on SNs locations as follows:

- Sensors on the left arm: For those sensors on the left arm (i.e., SN4 and SN5), H_0 experiences the same pattern for both CN1 and CN2 cases, where it varies by 2 dB when the left arm changes its orientation during the walk cycle. For the case of CN2, H_0 is also affected by the partial shadowing of the link by the right arm. The link from SN5 to CN2 experiences also a partial body shadowing when the left arm is behind the body.

- Sensors on the head and the shoulder: For SNs that move moderately such as SN1, SN2, and SN7, we logically observe only relatively small variations of about 0.7 dB due to the small changes of relative orientation angles. We also notice the same shadowing effects of the left arm for the link between SN2 and CN2, as before.

- Sensors on the legs: H_0 varies about 2 dB for the sensors on the legs (i.e., SN6, SN9, and SN10). For CN1, H_0 variations between SN6 on one hand, and SN9 and SN10, on the other hand, have opposite phases. For CN2, SN9 and SN10 have their highest H_0 when they have the same orientation. Also, due to the presence of a LOS between SN6 and CN2, H_0 increases considerably when the left thigh is raised to its maximum level.

- Sensors on the torso: We note that shadowing from the right arm experienced by SN8 has the same variation pattern for both CNs. Here, as concerns SN3, it additionally experiences left arm shadowing for the link with CN2.

A.2.2 Global mobility case

From the results of Fig. 4.3, we can notice periodic variations of H_0, which is consistent with the movement patterns of the SNs. Channel gains of the links related to the SNs on the legs and the arms experience more fluctuation than those of SNs on the torso. By observing the dynamics of the SN1 link, which has lower H_0 variations with respect to the local mobility case, we can see that approaching the walls increases the channel gain, which is true for all links. On the other hand, rotations of the body can decrease or increase H_0 significantly depending on whether it is close to or far from a wall.

Comparing the cases of CN1 and CN2, we notice that for SNs located on the arms and the legs, we have a higher H_0 for the case of CN2, whereas, for the SNs located on the upper part of the body, a higher H_0 is obtained with CN1. This is consistent with the observations on the average

Table A.2 — Estimated parameters of best fit distributions to H_0 for the case of CN1; Global mobility configuration.

SN	Best-fit PDFs	AIC	PDF parameters	
1	LN	−916	$\mu = -0.44$	$\sigma = 0.15$
	Gamma	−764	$a = 41.45$	$b = 0.02$
2	LN	−851	$\mu = -0.56$	$\sigma = 0.18$
	Gamma	−700	$a = 28.92$	$b = 0.02$
3	LN	−758	$\mu = -0.48$	$\sigma = 0.19$
	Gamma	−643	$a = 28.54$	$b = 0.02$
4	Nakagami	−818	$\alpha = 10.59$	$\xi = 0.50$
	Gamma	−786	$a = 41.22$	$b = 0.02$
5	LN	−681	$\mu = -0.51$	$\sigma = 0.21$
	Gamma	−625	$a = 23.54$	$b = 0.03$
6	LN	−665.1	$\mu = -0.65$	$\sigma = 0.24$
	Gamma	−570	$a = 16.79$	$b = 0.03$
7	LN	−653	$\mu = -0.89$	$\sigma = 0.31$
	Gamma	−460	$a = 9.45$	$b = 0.05$
8	LN	−521	$\mu = -0.76$	$\sigma = 0.31$
	Gamma	−405	$a = 10.2$	$b = 0.05$
9	LN	−741	$\mu = -0.75$	$\sigma = 0.25$
	Gamma	−595	$a = 15.57$	$b = 0.03$
10	LN	−1028	$\mu = -0.43$	$\sigma = 0.14$
	Gamma	−865	$a = 52.82$	$b = 0.01$

H_0 made in Subsection 4.3.1. For SN2, which is located on the head side, we see similar results for CN1 and CN2.

Lastly, for SN3 and SN5 located on the torso and the arm, we globally observe a local mobility pattern scaled by the global mobility variations.

A.3 Best-fit PDFs for H_0 for individual SN links

We provide here detailed data on the best-fit PDFs to the H_0 variations for each link between the SNs and the CNs. These are summarized in Tables A.2 and A.3 for the cases of CN1 and CN2, respectively.

Table A.3 — Estimated parameters of best fit distributions to H_0 for the case of CN2; Global mobility configuration.

SN	Best-fit PDFs	AIC	PDF parameters	
1	LN	−863	$\mu = -0.36$	$\sigma = 0.15$
	Gamma	−812	$a = 45.22$	$b = 0.02$
2	LN	−700	$\mu = -0.69$	$\sigma = 0.24$
	Gamma	−568	$a = 16.5$	$b = 0.03$
3	LN	−567.6	$\mu = -0.85$	$\sigma = 0.33$
	Gamma	−448	$a = 9.32$	$b = 0.05$
4	LN	−634	$\mu = -1.03$	$\sigma = 0.37$
	Gamma	−516	$a = 7.41$	$b = 0.05$
5	LN	−723	$\mu = -1.07$	$\sigma = 0.35$
	Gamma	−590	$a = 8.02$	$b = 0.05$
6	LN	−749	$\mu = -1.09$	$\sigma = 0.35$
	Gamma	−593	$a = 8.06$	$b = 0.05$
7	LN	−918	$\mu = -0.55$	$\sigma = 0.17$
	Gamma	−773	$a = 33.14$	$b = 0.02$
8	LN	−725	$\mu = -1.26$	$\sigma = 0.42$
	Gamma	−568	$a = 5.33$	$b = 0.06$
9	LN	−658	$\mu = -1.04$	$\sigma = 0.36$
	Gamma	−504	$a = 7.35$	$b = 0.05$
10	LN	−426	$\mu = -0.83$	$\sigma = 0.36$
	Gamma	−340	$a = 7.58$	$b = 0.06$

List of Figures

1.1 Typical hospital ward scenario with several patients equipped with medical WBANs. 5

1.2 A typical WBAN with the underlying communication tiers. 6

1.3 Block diagram of a typical OWC system. 10

1.4 OWC applications. 12

2.1 Block diagram of a typical OWC system. 20

2.2 Illustration examples of modulation schemes: (a) OOK, (b) 4-PPM, and (c) 4-PAM. 23

2.3 CAP transmission: Blocks denote up-sampler, FIR filers, and DAC. 24

2.4 PSD of a m-CAP signal: $m = 10$, $\beta = 0.1$, and system bandwidth is 1 MHz. 26

2.5 PIN-based PD schematic. 27

2.6 APD-based PD schematic. 27

2.7 System model of an optical system. 28

2.8 LOS and NLOS Contribution links of OWC systems. 30

3.1 Illustration of potential function: a) single reflection case, b) LOS case, c) multiple reflection case. 37

3.2 Illustration of the RWP mobility model for a node initially located at P_0. 39

3.3 Spatial node distribution according to RWP in a rectangular area of size (5 m × 5 m). 39

3.4 The simulated CIR for configuration A of [100]. (a) reference CIR and (b) simulated CIR using Opticstudio. 41

3.5 Adopted simulation methodology. 42

3.6 Illustration of the STL model of the body; (a) considered placements of SNs and CNs with the corresponding $\vec{n}_{\text{node}}$ vectors; (b) xyz intrinsic rotations made to direct the node along the orientation $\vec{n}_{\text{face}}$ of the triangular face: the Cartesian coordinates after roll-pitch-yaw rotations (in order) are denoted by $xy'z'$ (after roll rotation), $x''y'z''$ (after pitch rotation), and $x'''y'''z''$ (after yaw rotation). 44

3.7 Illustration of the local mobility during a walk cycle. 46

3.8 Top view of the typical user trajectory generated with the proposed improved RWP model for $N_p = 588$ positions. 47

4.1 A snapshot of the simulated random walk inside an empty room with Opticstudio. 51

4.2 H_0 variations and its mean value (in dB) for the cases of CN1 and CN2 in the local mobility configuration. 56

4.3 H_0 variations and its mean (in dB) for the cases of CN1 and CN2 over the global mobility trajectory. 57

4.4 Illustration of best-fitting PDFs to the ensemble of H_0 related to CN1. 59

4.5 Illustration of best-fitting PDFs to the ensemble of H_0 related to CN2. 60

4.6 ACF for the links between different SNs and CN1. 61

4.7 ACF for the links between different SNs and CN2. 61

4.8 P_{out} versus peak transmit power P_t for different data-rates R_b for the case of SN3-to-CN1 link using (a) a PIN (b) an APD. Uncoded NRZ-OOK modulation. 62

4.9 P_{out} versus peak transmit power P_t for different SN links and the cases of (a) CN1 and (b) CN2. Low background noise level with $I_b = 2\,\mu$A. 63

4.10 P_{out} versus the peak transmit power P_t for different SNs for the cases of (a) CN1 with PIN PD, (b) CN2 with PIN PD, (c) CN1 with APD, and (d) CN2 with APD. Relatively high background noise level with $I_b = 200\,\mu$A. 64

5.1 Illustration of the considered placements for the APs and the simulation trajectories. 69

5.2 Illustration of the considered placements for the CNs. 69

5.3 H_0 variations for the cases of CN1 and CN2 in the single AP configuration for AP5 and AP8 positions (see Fig.5.2). 70

5.4 H_0 variations for the cases of CN1 and CN2 in the multiple-AP configurations using EGC and SC detection methods. 71

5.5 H_0 variations for the cases of CN1 and CN2 in the multiple-AP configurations using EGC and SC detection methods. 72

5.6 Calculated ACF for the cases of (a) CN1 and (b) CN2 and different AP configuration based on the simulated user trajectory. 74

5.7 Histograms of H_0 (in linear scale) for 1103 channel realizations and estimated PDF by KDE with Gaussian kernel. (a) CN1 and AP5, (b) CN1 and AP1-AP4 with EGC and with (c) SC. . . 75

5.8 P_{out} versus the transmit power for different data-rates for the cases of (a) CN1 and AP5, (b) CN2 and AP5, (c) CN1 and AP1-AP4 with EGC, (d) CN2 and AP1-AP4 with EGC, (e) CN1 and AP1-AP4 with SC, and (f) CN2 and AP1-AP4 with SC. Uncoded OOK modulation. 77

5.9 P_{out} versus background noise current I_b for PIN- and APD-based Rxs with different AP configurations. (a) CN1, (b) CN2. Uncoded OOK modulation. $P_t = 15\,\text{mW}$, $R_b = 200\,\text{kbps}$. . . . 78

6.1 the concept of TDMA [158]. . . . 81

6.2 the frame structure of TDMA [158]. . . . 81

6.3 the concept of FDMA. . . . 82

6.4 the concept of MU m-CAP: (a) the Tx and (b) the Rx. . . . 84

6.5 BER vs SNR performance for MU 10-CAP system. Sub stands for sub-band. . . . 85

6.6 P_{out} vs P_t performance for MU 10-CAP system. . . . 85

6.7 The concept of pure ALOHA [160]. Two Txs are transmitting using pure ALOHA. Here, packets will collide as Tx1 started its transmission before Tx2 ended transmitting. . . . 87

6.8 The concept of slotted ALOHA. By allowing users to transmit only at the beginning of a slot, collisions are restricted to only when the Txs transmit simultaneously. . . . 87

6.9 The concept of CSMA/CA [163]. . . . 88

6.10 The considered network architecture. . . . 89

6.11 DQ frame structure. . . . 90

6.12 Multichannel DQ-MAC model. . . . 90

6.13 (a) Energy consumption vs. payload length for $\lambda = 0.8$, (b) energy consumption vs. traffic load, (c) average delay. . . . 93

List of Tables

1.1 Requirements on data-rate and BER for some medical applications [18, 19]. 7

3.1 Simulation parameters for configuration A of [100]. 40

3.2 Sensor and coordinator node positions and orientations as considered in Fig. 3.6(a). The last column indicates the corresponding Cartesian coordinates of the unit vectors $\vec{n}_{\text{node}}$ (after rotation). 45

4.1 Simulation parameters. 51

4.2 Mean H_0(in dB) and Standard variation σ_0 of the channel gain for different intra-WBAN links corresponding to CN1, for the Three considered configurations. 52

4.3 Mean H_0(in dB) and Standard variation σ_0 of the channel gain for different intra-WBAN links corresponding to CN2, for the Three considered configurations. 53

4.4 Mean and Standard Deviation (in ns) of the RMS delay spread for different intra-WBAN links corresponding to CN1, for the three considered configurations. 54

4.5 Mean and Standard Deviation (in ns) of the RMS delay spread for different intra-WBAN links corresponding to CN2, for the three considered configurations. 55

4.6 Estimated parameters of best fit distributions to H_0 for the ensemble of simulated data. . . 59

4.7 Channel coherence time: Delays (in seconds) corresponding to 90 % and 50 % of the ACF. . . 62

5.1 Mean and standard deviation (in ns) of the RMS delay spread. 72

5.2 Estimated channel coherence time T_c (in sec) corresponding to the 50 % of the ACF, based on the simulated user trajectory. 74

5.3 Calculated smoothing parameter ρ. 74

6.1 Power consumption (in mW) of optical and RF transceivers. 90

6.2 Simulation parameters [171]. 92

A.1 Range of variation of ϕ and θ for each sensor and coordinator nodes. 99

A.2 Estimated parameters of best fit distributions to H_0 for the case of CN1; Global mobility configuration. 101

A.3 Estimated parameters of best fit distributions to H_0 for the case of CN2; Global mobility configuration. 102

Bibliography

[1] *Life expectancy and healthy life expecancy data by country*, http://apps.who.int/gho/data/node.main.688?lang=en, Accessed: 16-02-2019.

[2] *Life expectancy increased by 5 years since 2000*, https://www.who.int/en/news-room/detail/19-05-2016-life-expectancy-increased-by-5-years-since-2000-but-health-inequalities-persist, Accessed: 16-02-2019.

[3] C. X. Wong, A. Brown, D. H. Lau, S. S. Chugh, C. M. Albert, *et al.*, "Epidemiology of sudden cardiac death: Global and regional perspectives," *Heart, Lung and Circulation*, vol. 28, no. 1, pp. 6–14, 2019.

[4] *Diabetes*, https://www.who.int/news-room/fact-sheets/detail/diabetes, Accessed: 04-10-2019.

[5] Y. Ma, Z. Luo, C. Steiger, G. Traverso, and F. Adib, "Enabling deep-tissue networking for miniature medical devices," in *ACM SIGCOMM Conference*, Budapest, Hungary, 2018, pp. 417–431.

[6] P. Abiri, A. Abiri, R. R. S. Packard, Y. Ding, A. Yousefi, *et al.*, "Inductively powered wireless pacing via a miniature pacemaker and remote stimulation control system," *Scientific Reports*, vol. 7, no. 6180, 2017.

[7] J. Kim, A. Balankutty, R. Dokania, A. Elshazly, H. S. Kim, *et al.*, "A 112Gb/s PAM-4 transmitter with 3-Tap FFE in 10nm CMOS," in *IEEE ISSCC Conference*, San Francisco, USA, 2018, pp. 102–104.

[8] L. Atzori, A. Iera, and G. Morabito, "The Internet of Things: A survey," *Computer Networks*, vol. 54, no. 15, pp. 2787 –2805, 2010.

[9] B. Varghese and R. Buyya, "Next generation cloud computing: New trends and research directions," *Future Generation Computer Systems*, vol. 79, pp. 849 –861, 2018.

[10] H. Cao, V. Leung, C. Chow, and H. Chan, "Enabling technologies for wireless body area aetworks: A survey and outlook," *IEEE Communications Magazine*, vol. 47, no. 12, pp. 84–93, 2009.

[11] M. Chen, S. Gonzalez, A. Vasilakos, H. Cao, and V. C. Leung, "Body area networks: A survey," *Mobile Networks and Applications*, vol. 16, no. 2, pp. 171–193, 2011.

[12] B. Latré, B. Braem, I. Moerman, C. Blondia, and P. Demeester, "A survey on wireless body area networks," *Wireless Networks*, vol. 17, no. 1, pp. 1–18, 2011.

[13] S. Movassaghi, M. Abolhasan, J. Lipman, D. Smith, and A. Jamalipour, "Wireless body area networks: A survey," *IEEE Communications Surveys & Tutorials*, vol. 16, no. 3, pp. 1658–1686, 2014.

[14] M. Ghamari, B. Janko, R. S. Sherratt, W. Harwin, R. Piechockic, *et al.*, "A survey on wireless body area networks for eHealthcare systems in residential environments," *Sensors*, vol. 16, no. 6, 2016.

[15] S. Majumder, T. Mondal, and M. J. Deen, "Wearable sensors for remote health monitoring," *Sensors*, vol. 17, no. 1, pp. 261–268, 2017.

[16] O. Haddad and M. A. Khalighi, "Enabling communication technologies for medical wireless body-area networks," in *2019 Global LiFi Congress (GLC)*, Paris, France, 2019, pp. 1–5.

[17] B. Zhen, M. Patel, S. Lee, E. Won, and A. Astrin, "TG6 technical requirements document (TRD), IEEE P802.15-08-0644-09-0006," 2008.

[18] D. Lewis, "TG6 applications summary, IEEE P802.15-08-0407-03," 2008.

[19] A. Julien-Vergonjanne, S. Sahuguède, and L. Chevalier, "Optical wireless communications: An emerging technology," in Springer, 2016, ch. Optical Wireless Body Area Networks for Healthcare Applications, pp. 569–587.

[20] X. Pu, W. Hu, and Z. L. Wang, "Toward wearable self-charging power systems: The integration of energy-harvesting and storage devices," *Small*, vol. 14, no. 1, p. 1 702 817, 2018.

[21] P. D. Diamantoulakis and G. K. Karagiannidis, "Simultaneous lightwave information and power transfer (SLIPT) for indoor IoT applications," in *GLOBECOM Conference*, Singapore, Singapore, 2017, pp. 1–6.

[22] *Bluetooth Core Specification Version 5.1*, 2019.

[23] *IEEE Standard for Low-Rate Wireless Networks*, 2016.

[24] *ZigBee Document 053474r20*, 2012.

[25] *IEEE standard for local and metropolitan area networks - part 15.6: Wireless body area networks*, 2012.

[26] M. Esposito, A. Minutolo, R. Megna, M. Forastiere, M. Magliulo, *et al.*, "A smart mobile, self-configuring, context-aware architecture for personal health monitoring," *Engineering Applications of Artificial Intelligence*, vol. 67, pp. 136 –156, Jan. 2018.

[27] J. Wannenburg, R. Malekian, and G. P. Hancke, "Wireless capacitive-based ECG sensing for feature extraction and mobile health monitoring," *IEEE Sensors Journal*, vol. 18, no. 14, pp. 6023–6032, 2018.

[28] A. Ahmed, A. A. Lukman, A. James, O. O. Mikail, B. U. Umar, *et al.*, "Human vital physiological parameters monitoring: A wireless body area technology based Internet of things," *Jurnal Teknologi dan Sistem Komputer*, vol. 6, no. 3, pp. 115–121, 2018.

[29] N. Dey, A. S. Ashour, F. Shi, S. J. Fong, and R. S. Sherratt, "Developing residential wireless sensor networks for ECG healthcare monitoring," *IEEE Transactions on Consumer Electronics*, vol. 63, no. 4, pp. 442–449, 2017.

[30] M. Clarke, J. de Folter, V. Verma, and H. Gokalp, "Interoperable end-to-end remote patient monitoring platform based on IEEE 11073 PHD and ZigBee health care profile," *IEEE Transactions on Biomedical Engineering*, vol. 65, no. 5, pp. 1014–1025, 2018.

[31] A. M. Cristiani, G. M. Bertolotti, E. Marenzi, and S. Ramat, "An instrumented insole for long term monitoring movement, comfort, and ergonomics," *IEEE Sensors Journal*, vol. 14, no. 5, pp. 1564–1572, 2014.

[32] T. Wu, F. Wu, J. Redouté, and M. R. Yuce, "An autonomous wireless body area network implementation towards IoT connected healthcare applications," *IEEE Access*, vol. 5, pp. 11 413–11 422, 2017.

[33] L. Wang, Y. Hsiao, X. Xie, and S. Lee, "An outdoor intelligent healthcare monitoring device for the elderly," *IEEE Transactions on Consumer Electronics*, vol. 62, no. 2, pp. 128–135, 2016.

[34] K. Becher, C. P. Figueiredo, C. Mühle, R. Ruff, P. M. Mendes, *et al.*, "Design and realization of a wireless sensor gateway for health monitoring," in *International Conference of the IEEE Engineering in Medicine and Biology*, Buenos Aires, Argentina, 2010, pp. 374–377.

[35] M. J. Weber, Y. Yoshihara, A. Sawaby, J. Charthad, T. C. Chang, *et al.*, "A high-precision 36 mm3 programmable implantable pressure sensor with wully ultrasonic power-up and data link," in *Symposium on VLSI Circuits*, Kyoto, Japan, 2017, pp. C104–C105.

[36] G. E. Santagati and T. Melodia, "Experimental evaluation of impulsive ultrasonic intrabody communications for implantable biomedical devices," *IEEE Transactions on Mobile Computing*, vol. 16, no. 2, pp. 367–380, 2017.

[37] C. Le Bas, S. Sahuguède, A. Julien-Vergonjanne, P. Combeau, and L. Aveneau, "Infrared and visible links for medical body sensor networks," in *Global LiFi Congress (GLC)*, Paris, France, 2018, pp. 1–6.

[38] C. Le Bas, S. Sahuguède, and A. Julien-Vergonjanne, "Theoretical and experimental approach for the design of an optical wireless physical activity monitoring system," *International Journal of Wireless Information Networks*, vol. 24, no. 2, pp. 65–77, 2017.

[39] J. L. Abita and W. Schneider, "Transdermal optical communications," *John Hopkins APL Tech*, vol. 25, no. 3, pp. 261–268, 2004.

[40] M. Faria, L. N. Alves, and P. S. de Brito Andre, "Visible light communications: Theory and applications," in CRC-Press, 2017, ch. Transdermmal Optical Communications, pp. 309–336.

[41] S. E. Trevlakis, A.-A. A. Boulogeorgos, P. C. Sofotasios, S. Muhaidat, and G. K. Karagiannidis, "Optical wireless cochlear implants," *Biomedical Optics Express*, vol. 10, no. 2, pp. 707–730, 2019.

[42] S. Parmentier, R. Fontaine, and Y. Roy, "Laser diode used in 16 Mb/s, 10 mw optical transcutaneous telemetry system," in *IEEE Biomedical Circuits and Systems Conference*, Baltimore, MD, USA, 2008, pp. 377–380.

[43] Y. Gil, N. Rotter, and S. Arnon, "Feasibility of retroreflective transdermal optical wireless communication," *Appl. Opt.*, vol. 51, no. 18, pp. 4232–4239, 2012.

[44] T. Liu, U. Bihr, S. M. Anis, and M. Ortmanns, "Optical transcutaneous link for low power, high data rate telemetry," in *International Conference of the IEEE Engineering in Medicine and Biology Society*, San Diego, CA, USA, 2012, pp. 3535–3538.

[45] T. Liu, U. Bihr, J. Becker, J. Anders, and M. Ortmanns, "In vivo verification of a 100 Mbps transcutaneous optical telemetric link," in *IEEE BioCAS Conference*, Lausanne, Switzerland, 2014, pp. 580–583.

[46] T. Liu, J. Anders, and M. Ortmanns, "Bidirectional optical transcutaneous telemetric link for brain machine interface," *Electronics Letters*, vol. 51, 1969–1971(2), 24 2015.

[47] Z. Ghassemlooy, S. Zvanovec, M.-A. Khalighi, W. O. Popoola, and J. Perez, "Optical wireless communication systems," *Optik*, vol. 151, pp. 1–6, 2017, Optical Wireless Communication Systems.

[48] M. A. Khalighi, Z. Ghassemlooy, M.-S. Alouini, S. Hranilovic, and S. Zvanovec, "Special issue on: Optical wireless communications for emerging connectivity requirements," *IEEE Open Journal of the Communications Society*, vol. 2, pp. 82–86, 2021.

[49] Z. Ghassemlooy, M. Uysal, M. A. Khalighi, V. Ribeiro, F. Moll, *et al.*, "An overview of optical wireless communications," in *Optical Wireless Communications: An Emerging Technology*, M. Uysal, C. Capsoni, Z. Ghassemlooy, A. Boucouvalas, and E. Udvary, Eds. Cham: Springer International Publishing, 2016, pp. 1–23.

[50] Y. Lu and H. Gu, "Flexible and scalable optical interconnects for data centers: Trends and challenges," *IEEE Communications Magazine*, vol. 57, no. 10, pp. 27–33, 2019.

[51] C. Chaintoutis, B. Shariati, A. Bogris, P. V. Dijk, C. G. H. Roeloffzen, *et al.*, "Free space intra-datacenter interconnects based on 2D optical beam steering enabled by photonic integrated circuits," *Photonics*, vol. 5, no. 3, 2018.

[52] I. Stefan, H. Burchardt, and H. Haas, "Area spectral efficiency performance comparison between VLC and RF femtocell networks," in *2013 IEEE International Conference on Communications (ICC)*, Budapest, Hungary, 2013, pp. 3825–3829.

[53] Y. Zhuang, L. Hua, L. Qi, J. Yang, P. Cao, *et al.*, "A survey of positioning systems using visible LED lights," *IEEE Communications Surveys Tutorials*, vol. 20, no. 3, pp. 1963–1988, 2018.

[54] T. Koonen, "Indoor optical wireless systems: Technology, trends, and applications," *Journal of Lightwave Technology*, vol. 36, no. 8, pp. 1459–1467, 2018.

[55] T. Nguyen, A. Islam, T. Hossan, and Y. M. Jang, "Current status and performance analysis of optical camera communication technologies for 5G networks," *IEEE Access*, vol. 5, pp. 4574–4594, 2017.

[56] P. Combeau, S. Joumessi-Demeffo, A. Julien-Vergonjanne, L. Aveneau, S. Sahuguède, *et al.*, "Optical wireless channel simulation for communications inside aircraft cockpits," *J. Lightwave Technol.*, vol. 38, no. 20, pp. 5635–5648, 2020.

[57] S. Joumessi-Demeffo, S. Sahuguède, A. Julien-Vergonjanne, and P. Combeau, "Performance trade-offs of an optical wireless communication network deployed in an aircraft cockpit," *IEEE Open Journal of the Communications Society*, vol. 1, pp. 849–862, 2020.

[58] M. Uysal, Z. Ghassemlooy, A. Bekkali, A. Kadri, and H. Menouar, "Visible light communication for vehicular networking: Performance study of a V2V system using a measured headlamp beam pattern model," *IEEE Vehicular Technology Magazine*, vol. 10, no. 4, pp. 45–53, 2015.

[59] M. Uysal, "Visible light communications: From theory to industrial standardization," in *Optical Fiber Communication Conference (OFC) 2019*, San Diego, CA, USA, Optical Society of America, 2019, Th3I.4.

[60] M.-A. Khalighi, C. Gabriel, T. Hamza, S. Bourennane, P. Léon, *et al.*, "Underwater wireless optical communication; recent advances and remaining challenges," in *2014 16th International Conference on Transparent Optical Networks (ICTON)*, Graz, Austria, 2014, pp. 1–4.

[61] C. Gabriel, M.-A. Khalighi, S. Bourennane, P. Léon, and V. Rigaud, "Monte-Carlo-based channel characterization for underwater optical communication systems," *J. Opt. Commun. Netw.*, vol. 5, no. 1, pp. 1–12, 2013.

[62] M.-A. Khalighi, C. Gabriel, L. Pessoa, and B. Silva, "Visible light communications: Theory and applications," in CRC-Press, Jun. 2017, ch. Underwater Visible Light Communications, Channel Modeling and System Design, pp. 337–371.

[63] T. Essalih, M. A. Khalighi, S. Hranilovic, and H. Akhouayri, "Optical OFDM for SiPM-based underwater optical wireless communication links," *Sensors*, vol. 20, no. 21, 2020.

[64] M. A. Khalighi and M. Uysal, "Survey on free space optical communication: A communication theory perspective," *IEEE Communications Surveys Tutorials*, vol. 16, no. 4, pp. 2231–2258, 2014.

[65] F. Nadeem, V. Kvicera, M. S. Awan, E. Leitgeb, S. S. Muhammad, *et al.*, "Weather effects on hybrid FSO/RF communication link," *IEEE Journal on Selected Areas in Communications*, vol. 27, no. 9, pp. 1687–1697, 2009.

[66] H. Willebrand and B. Ghuman, "Fiber optics without fiber," *IEEE Spectrum*, vol. 38, no. 8, pp. 40–45, 2001.

[67] D. Kedar and S. Arnon, "Urban optical wireless communication networks: The main challenges and possible solutions," *IEEE Communications Magazine*, vol. 42, no. 5, S2–S7, 2004.

[68] G. Parca, A. Shahpari, V. Carrozzo, G. M. T. Beleffi, and A. L. J. Teixeira, "Optical wireless transmission at 1.6-Tbit/s (16 x 100 Gbit/s) for next-generation convergent urban infrastructures," *Optical Engineering*, vol. 52, no. 11, pp. 1 –6, 2013.

[69] M. T. Dabiri, S. M. S. Sadough, and M. A. Khalighi, "Channel modeling and parameter optimization for hovering UAV-based free-space optical links," *IEEE Journal on Selected Areas in Communications*, vol. 36, no. 9, pp. 2104–2113, 2018.

[70] H. Haan, M. Gerken, and M. Tausendfreund, "Long-range laser communication terminals: Technically interesting, commercially incalculable," in *2012 8th International Symposium on Communication Systems, Networks Digital Signal Processing (CSNDSP)*, Poznan, Poland, 2012, pp. 1–4.

[71] J. Poliak, D. Giggenbach, F. Moll, F. Rein, C. Fuchs, *et al.*, "Terabit-throughput GEO satellite optical feeder link testbed," in *2015 13th International Conference on Telecommunications (ConTEL)*, Graz, Austria, 2015, pp. 1–5.

[72] H. Kaushal and G. Kaddoum, "Optical communication in space: Challenges and mitigation techniques," *IEEE Communications Surveys Tutorials*, vol. 19, no. 1, pp. 57–96, 2017.

[73] W. Fawaz, C. Abou-Rjeily, and C. Assi, "UAV-aided cooperation for FSO communication systems," *IEEE Communications Magazine*, vol. 56, no. 1, pp. 70–75, 2018.

[74] A. K. Majumdar, "Free-space optical (FSO) platforms: Unmanned aerial vehicle (UAV) and mobile," in *Advanced Free Space Optics (FSO): A Systems Approach*. New York, NY: Springer New York, 2015, pp. 203–225.

[75] F. Moll, J. Horwath, A. Shrestha, M. Brechtelsbauer, C. Fuchs, *et al.*, "Demonstration of high-rate laser communications from a fast airborne platform," *IEEE Journal on Selected Areas in Communications*, vol. 33, no. 9, pp. 1985–1995, 2015.

[76] Z. Ghassemlooy, L. N. Alves, S. Zvànovec, and M. A. Khalighi, Eds., *Visible Light Communications: Theory and Applications*. CRC-Press, 2017.

[77] W. Popoola and S. Rajbhandari, *Optical Wireless Communications: System and Channel Modelling with MATLAB*. Aug. 2012.

[78] P. Chvojka, P. Dvorak, P. Pesek, S. Zvanovec, P. A. Haigh, *et al.*, "Characterization of the organic LED based visible light communications," in *2016 10th International Symposium on Communication Systems, Networks and Digital Signal Processing (CSNDSP)*, Prague, Czech Republic, 2016, pp. 1–4.

[79] Z. N. Chaleshtori, S. Zvanovec, Z. Ghassemlooy, H. B. Eldeeb, and M. Uysal, "Coverage of a shopping mall with flexible OLED-based visible light communications," *Opt. Express*, vol. 28, no. 7, pp. 10 015–10 026, 2020.

[80] T. Komine, J. H. Lee, S. Haruyama, and M. Nakagawa, "Adaptive equalization system for visible light wireless communication utilizing multiple white LED lighting equipment," *IEEE Transactions on Wireless Communications*, vol. 8, no. 6, pp. 2892–2900, 2009.

[81] B. Schrenk, M. Hofer, F. Laudenbach, H. Hübel, and T. Zemen, "Visible-light multi-Gb/s transmission based on resonant cavity LED with optical energy feed," *IEEE Journal on Selected Areas in Communications*, vol. 36, no. 1, pp. 175–184, 2018.

[82] R. X. G. Ferreira, E. Xie, J. J. D. McKendry, S. Rajbhandari, H. Chun, *et al.*, "High bandwidth GaN-based micro-LEDs for multi-Gb/s visible light communications," *IEEE Photonics Technology Letters*, vol. 28, no. 19, pp. 2023–2026, 2016.

[83] G. Held, *Introduction to Light Emitting Diode Technology and Applications (1st ed.)* Auerbach Publications, 2008.

[84] S. Arnon, J. Barry, G. Karagiannidis, R. Schober, and M. Uysal, *Advanced Optical Wireless Communication Systems: Optical wireless communication theory*. Cambridge University Press, 2012.

[85] A. A. Farid and S. Hranilovic, "Outage capacity optimization for free-space optical links with pointing errors," *Journal of Lightwave Technology*, vol. 25, no. 7, pp. 1702–1710, 2007.

[86] M.-A. Khalighi, S. Long, S. Bourennane, and Z. Ghassemlooy, "PAM- and CAP-based transmission schemes for visible-light communications," *IEEE Access*, vol. 5, pp. 27 002–27 013, 2017.

[87] S. Long and M. Ali Khalighi, "Advantage of CAP signaling for VLC systems under non-linear LED characteristics," in *2019 2nd West Asian Colloquium on Optical Wireless Communications (WACOWC)*, Tehran, Iran, 2019, pp. 21–25.

[88] J. Armstrong, "OFDM for optical communications," *Journal of Lightwave Technology*, vol. 27, no. 3, pp. 189–204, 2009.

[89] J. Carruthers and J. Kahn, "Multiple-subcarrier modulation for nondirected wireless infrared communication," *IEEE Journal on Selected Areas in Communications*, vol. 14, no. 3, pp. 538–546, 1996.

[90] O. González, R. Pérez-Jiménez, S. Rodríguez, J. Rabadán, and A. Ayala, "OFDM over indoor wireless optical channel," *IEE Proceedings - Optoelectronics*, vol. 152, 199–204(5), 4 2005.

[91] D. Tsonev, S. Sinanovic, and H. Haas, "Novel unipolar orthogonal frequency division multiplexing (U-OFDM) for optical wireless," in *2012 IEEE 75th Vehicular Technology Conference (VTC Spring)*, Yokohama, Japan, 2012, pp. 1–5.

[92] S. D. Dissanayake and J. Armstrong, "Comparison of ACO-OFDM, DCO-OFDM and ADO-OFDM in IM/DD systems," *Journal of Lightwave Technology*, vol. 31, no. 7, pp. 1063–1072, 2013.

[93] S. C. J. Lee, S. Randel, F. Breyer, and A. M. J. Koonen, "PAM-DMT for intensity-modulated and direct-detection optical communication systems," *IEEE Photonics Technology Letters*, vol. 21, no. 23, pp. 1749–1751, 2009.

[94] Q. Wang, C. Qian, X. Guo, Z. Wang, D. G. Cunningham, *et al.*, "Layered ACO-OFDM for intensity-modulated direct-detection optical wireless transmission," *Opt. Express*, vol. 23, no. 9, pp. 12 382–12 393, 2015.

[95] P. A. Haigh, S. T. Le, S. Zvanovec, Z. Ghassemlooy, P. Luo, *et al.*, "Multi-band carrier-less amplitude and phase modulation for bandlimited visible light communications systems," *IEEE Wireless Communications*, vol. 22, no. 2, pp. 46–53, 2015.

[96] P. A. Haigh, P. Chvojka, Z. Ghassemlooy, S. Zvanovec, and I. Darwazeh, "Visible light communications: Multi-band super-Nyquist CAP modulation," *Opt. Express*, vol. 27, no. 6, pp. 8912–8919, 2019.

[97] Z. Ghassemlooy, M. Khalighi, and D. Wu, "Visible light communications: Theory and applications," in CRC-Press, 2017, ch. Channel Modeling, pp. 71–96.

[98] F. R. Gfeller and U. Bapst, "Wireless in-house data communication via diffuse infrared radiation," *Proceedings of the IEEE*, vol. 67, no. 11, pp. 1474–1486, 1979.

[99] J. M. Kahn and J. R. Barry, "Wireless infrared communications," *Proceedings of the IEEE*, vol. 85, no. 2, pp. 265–298, 1997.

[100] J. R. Barry, J. M. Kahn, W. J. Krause, E. A. Lee, and D. G. Messerschmitt, "Simulation of multipath impulse response for indoor wireless optical channels," *IEEE Journal on Selected Areas in Communications*, vol. 11, no. 3, pp. 367–379, 1993.

[101] S. Long, M. A. Khalighi, M. Wolf, S. Bourennane, and Z. Ghassemlooy., "Investigating channel frequency selectivity in indoor visible-light communication systems," *IET Optoelectronics*, vol. 10, 80–88(8), 3 2016.

[102] F. Xu, M. Khalighi, and S. Bourennane, "Impact of different noise sources on the performance of PIN- and APD-based FSO receivers," in *International Conference on Telecommunications (ConTel)*, Graz, Austria, 2011, pp. 211–218.

[103] M. A. Khalighi, F. Xu, Y. Jaafar, and S. Bourennane, "Double-laser differential signaling for reducing the effect of background radiation in free-space optical systems," *J. Opt. Commun. Netw.*, vol. 3, no. 2, pp. 145–154, 2011.

[104] J. B. Carruthers and P. Kannan, "Iterative site-based modeling for wireless infrared channels," *IEEE Transactions on Antennas and Propagation*, vol. 50, no. 5, pp. 759–765, 2002.

[105] Y. A. Alqudah and M. Kavehrad, "MIMO characterization of indoor wireless optical link using a diffuse-transmission configuration," *IEEE Transactions on Communications*, vol. 51, no. 9, pp. 1554–1560, 2003.

[106] F. J. Lopez-Hernandez, R. Perez-Jimenez, and A. Santamaria, "Ray-tracing algorithms for fast calculation of the channel impulse response on diffuse IR wireless indoor channels," *Optical Engineering*, vol. 39, no. 10, pp. 2775–2780, 2000.

[107] S. Rodriguez-Perez, R. Perez-Jimenez, F. J. Lopez-Hernandez, O. B. Gonzalez-Hernandez, and A. J. Ayala-Alfonso, "Reflection model for calculation of the impulse response on IR-wireless indoor channels using ray-tracing algorithm," *Microwave and Optical Technology Letters*, vol. 32, no. 4, pp. 296–300, 2002.

[108] F. Miramirkhani and M. Uysal, "Channel modeling and characterization for visible light communications," *IEEE Photonics Journal*, vol. 7, no. 6, pp. 1–16, 2015.

[109] H. Schulze, "Frequency-domain simulation of the indoor wireless optical communication channel," *IEEE Transactions on Communications*, vol. 64, no. 6, pp. 2551–2562, 2016.

[110] J. M. Kahn, W. J. Krause, and J. B. Carruthers, "Experimental characterization of non-directed indoor infrared channels," *IEEE Transactions on Communications*, vol. 43, no. 2/3/4, pp. 1613–1623, 1995.

[111] S. M. Mana, P. Hellwig, J. Hilt, P. W. Berenguer, and V. Jungnickel, "Experiments in non-line-of-sight Li-Fi channels," *Global LIFI Congress (GLC)*, pp. 1–6, 2019, Paris, France.

[112] R. Perez-Jimenez, J. Berges, and M. J. Betancor, "Statistical model for the impulse response on infrared indoor diffuse channels," *Electronics Letters*, vol. 33, no. 15, pp. 1298–1300, 1997.

[113] J. B. Carruthers and S. M. Carroll, "Statistical impulse response models for indoor optical wireless channels," *International Journal of Communication Systems*, vol. 18, no. 3, pp. 267–284, 2005.

[114] T. Komine, S. Haruyama, and M. Nakagawa, "A study of shadowing on indoor visible-light wireless communication utilizing plural white LED lightings," *Wireless Personal Communications*, vol. 34, no. 1, pp. 211–225, 2005.

[115] Y. Xiang, M. Zhang, M. Kavehrad, M. I. S. Chowdhury, M. Liu, *et al.*, "Human shadowing effect on indoor visible light communications channel characteristics," *Optical Engineering*, vol. 53, no. 8, pp. 1–8, 2014.

[116] P. Chvojka, S. Zvanovec, P. A. Haigh, and Z. Ghassemlooy, "Channel characteristics of visible light communications within dynamic indoor environment," *Journal of Lightwave Technology*, vol. 33, no. 9, pp. 1719–1725, 2015.

[117] F. Miramirkhani, O. Narmanlioglu, M. Uysal, and E. Panayirci, "A mobile channel model for VLC and application to adaptive system design," *IEEE Communications Letters*, vol. 21, no. 5, pp. 1035–1038, 2017.

[118] M. D. Soltani, A. A. Purwita, Z. Zeng, H. Haas, and M. Safari, "Modeling the random orientation of mobile devices: Measurement, analysis and LiFi use case," *IEEE Transactions on Communications*, vol. 67, no. 3, pp. 2157–2172, 2019.

[119] A. Behlouli, P. Combeau, and L. Aveneau, "MCMC methods for realistic indoor wireless optical channels simulation," *Journal of Lightwave Technology*, vol. 35, no. 9, pp. 1575–1587, 2017.

[120] Behlouli, P. Combeau, S. Sahuguède, A. Julien-Vergonjanne, C. Le Bas, *et al.*, "Impact of physical and geometrical parameters on visible light communication links," in *2017 Advances in Wireless and Optical Communications (RTUWO)*, Riga, Latvia, 2017, pp. 73–76.

[121] D. R. Dhatchayeny, S. Arya, and Y. H. Chung, "Patient mobility support for indoor non-directed optical body area networks," *Sensors*, vol. 19, no. 10, 2019.

[122] B. Hoang Thai, S. Sahuguède, and A. Julien-Vergonjanne, "Optical wireless network design for off-body-sensor based monitoring," *Wireless Communications and Mobile Computing*, vol. 2019, pp. 1–13, 2019.

[123] M. Gallo, P. S. Hall, Y. I. Nechayev, and M. Bozzetti, "Use of animation software in simulation of on-body communications channels at 2.45 GHz," *IEEE Antennas and Wireless Propagation Letters*, vol. 7, no. 7, pp. 321–324, 2008.

[124] M. Gallo, P. S. Hall, Q. Bai, Y. I. Nechayev, C. C. Constantinou, *et al.*, "Simulation and measurement of dynamic on-body communication channels," *IEEE Transactions on Antennas and Propagation*, vol. 59, no. 2, pp. 623–630, 2011.

[125] T. Uusitupa and T. Aoyagi, "Analysis of dynamic on-body communication channels for various movements and polarization schemes at 2.45 GHz," *IEEE Transactions on Antennas and Propagation*, vol. 61, no. 12, pp. 6168–6179, 2013.

[126] S. L. Cotton, W. G. Scanlon, and B. K. Madahar, "Millimeter-wave soldier-to-soldier communications for covert battlefield operations," *IEEE Communications Magazine*, vol. 47, no. 10, pp. 72–81, 2009.

[127] M. Mackowiak and L. M. Correia, "A statistical model for the influence of body dynamics on the gain pattern of wearable antennas in off-body radio channels," *Springer Wireless Personal Communications*, vol. 73, no. 3, pp. 381–399, 2013.

[128] K. Turbic, L. M. Correia, and M. Beko, "A mobility model for wearable antennas on dynamic users," *IEEE Access*, vol. 6, no. 6, pp. 63 635–63 648, 2018.

[129] H. Ren and M. Q. h. Meng, "Understanding the mobility model of wireless body sensor networks," *International Conference on Information Acquisition*, pp. 306–310, 2006, Weihai, China.

[130] M. Nabi, M. Geilen, and T. Basten, "MoBAN: A configurable mobility model for wireless body area networks," *International ICST Conference on Simulation Tools and Techniques (SIMUTools)*, pp. 168–177, 2011, Barcelona, Spain.

[131] S. N. Pattanaik and S. P. Mudur, "The potential equation and importance in illumination computations," *Computer Graphics Forum*, vol. 12, no. 2, pp. 131–136, 1993.

[132] Ph. Dutré, E. Lafortune, and Y. D. Willems, "A mathematical framework for global illumination algorithms," in *Winter School of Computer Graphics and CAD Systems*, Pilsen, Czech Republic, 1994, pp. 75–84.

[133] C. Bettstetter, H. Hartenstein, and X. Pérez-Costa, "Stochastic properties of the random waypoint mobility model," *Wireless Networks*, vol. 10, no. 5, pp. 555–567, 2004.

[134] *Opticstudio*, `https://www.zemax.com/products/opticstudio`, Accessed: 16-09-2019.

[135] O. Haddad, M. Khalighi, S. Zvanovec, and M. Adel, "Channel characterization and modeling for optical wireless body-area networks," *IEEE Open Journal of the Communications Society*, vol. 1, pp. 760–776, 2020.

[136] A. Fort, C. Desset, P. De Doncker, P. Wambacq, and L. Van Biesen, "An ultra-wideband body area propagation channel model-from statistics to implementation," *IEEE Transactions on Microwave Theory and Techniques*, vol. 54, no. 4, pp. 1820–1826, 2006.

[137] V. Epanechnikov, "Non-parametric estimation of a multivariate probability density," *Theory of Probability and Its Applications*, vol. 14, no. 1, pp. 153–158, 1969.

[138] B. Silverman, *Density Estimation for Statistics and Data Analysis*. London: Chapman & Hall/CRC, 1986.

[139] *Blender*, `https://www.blender.org/`, Accessed: 23-09-2019.

[140] *3D mesh*, `https://3docean.net/item/low-poly-base-mesh-male/73426?WT.ac=category_thumb&WT.seg_1=category_thumb&WT.z_author=karan8/`, Accessed: 23-05-2020.

[141] P. B. Davenport, "Rotations about nonorthogonal axes.," *AIAA Journal*, vol. 11, no. 6, pp. 853–857, 1973.

[142] F. d. Dinechin and M. Istoan, "Hardware implementations of fixed-point atan2," in *2015 IEEE 22nd Symposium on Computer Arithmetic*, Lyon, France, 2015, pp. 34–41.

[143] *Animation tutorial*, `https://www.blendernation.com/2020/05/16/rig-anything-with-rigify-3-prebuilt-meta-rigs-biped-quadruped/`, Accessed: 23-05-2020.

[144] J. E. Graham, S. R. Fisher, I.-M. Bergés, Y.-F. Kuo, and G. V. Ostir, "Walking speed threshold for classifying walking independence in hospitalized older adults," *Physical Therapy*, vol. 90, no. 11, pp. 1591–1597, 2010.

[145] R. P. Duncan, M. E. McNeely, and G. M. Earhart, "Maximum step length test performance in people with Parkinson disease: A cross-sectional study," *Journal of Neurologic Physical Therapy*, vol. 41, no. 4, pp. 215–221, 2017.

[146] M. T. Dabiri, S. M. S. Sadough, and M. A. Khalighi, "FSO channel estimation for OOK modulation with APD receiver over atmospheric turbulence and pointing errors," *Optics Communications*, vol. 402, pp. 577 –584, 2017.

[147] O. Haddad, M. A. Khalighi, S. Zvanovec, and M. Adel, "Performance analysis of optical Intra-WBAN links," in *Int. Symp. Commun. Syst., Netw. Digital Sig. Proc. (CSNDSP)*, Porto, Portugal, 2020.

[148] K. Lee, H. Park, and J. R. Barry, "Indoor channel characteristics for visible light communications," *IEEE Communications Letters*, vol. 15, no. 2, pp. 217–219, 2011.

[149] L. Chevalier, S. Sahuguède, and A. Julien-Vergonjanne, "Optical wireless links as an alternative to radio-frequency for medical body area networks," *IEEE Journal on Selected Areas in Communications*, vol. 33, no. 9, pp. 2002–2010, 2015.

[150] M. Abtahi and H. Hashemi, "Simulation of indoor propagation channel at infrared frequencies in furnished office environments," in *Proceedings of 6th International Symposium on Personal, Indoor and Mobile Radio Communications*, Toronto, Ontario, Canada, vol. 1, 1995, pp. 306–310.

[151] D. B. Smith and L. W. Hanlen, "Ultra-low-power short-range radios," in Springer International Publishing, 2015, ch. Channel Modeling for Wireless Body Area Networks, pp. 25–55.

[152] D. B. Smith, J. Zhang, L. W. Hanlen, D. Miniutti, D. Rodda, *et al.*, "Temporal correlation of dynamic on-body area radio channel," *Electronics Letters*, vol. 45, no. 24, pp. 1212–1213, 2009.

[153] M. Mohamed, M. Cheffena, and A. Moldsvor, "Characterization of the body-to-body propagation channel for subjects during sports activities," *Sensors*, vol. 18, no. 2, 2018.

[154] A. J. C. Moreira, R. T. Valadas, and A. M. de Oliveira Duarte, "Characterisation and modelling of artificial light interference in optical wireless communication systems," in *Proceedings of 6th International Symposium on Personal, Indoor and Mobile Radio Communications (PIMRC)*, Toronto, ON, Canada, vol. 1, 1995, pp. 326–331.

[155] O. Haddad, M. A. Khalighi, and S. Zvanovec, "Channel characterization for optical extra-WBAN links considering local and global user mobility," *SPIE Conference, Broadband Access Communication Technologies XIV*, vol. 11307, pp. 89–97, 2020, San Francisco, CA.

[156] J. G. Proakis and M. Salehi, *Digital Communications*, 5th. New York: McGraw-Hill, 2007.

[157] M. J. Hasan, M. A. Khalighi, J. Garcia-Marquez, and B. Béchadergue, "Performance analysis of Optical-CDMA for uplink transmission in medical extra-WBANs," *IEEE Access*, vol. 8, pp. 171 672–171 685, 2020.

[158] A. Molisch, *Wireless Communications*, 2nd. J. Wiley & Sons, 2005.

[159] A. Goldsmith, *Wireless Communications*. Cambridge University Press, 2005.

[160] T. Rappaport, *Wireless communications - principles and practice*. Prentice Hall, 1996.

[161] P. A. Haigh, A. Burton, K. Werfli, H. L. Minh, E. Bentley, *et al.*, "A multi-CAP visible-light communications system with 4.85-b/s/Hz spectral efficiency," *IEEE Journal on Selected Areas in Communications*, vol. 33, no. 9, pp. 1771–1779, 2015.

[162] M. I. Olmedo, T. Zuo, J. B. Jensen, Q. Zhong, X. Xu, *et al.*, "Multiband carrierless amplitude phase modulation for high capacity optical data links," *Journal of Lightwave Technology*, vol. 32, no. 4, pp. 798–804, 2014.

[163] G. Bianchi, "Performance analysis of the ieee 802.11 distributed coordination function," *IEEE Journal on Selected Areas in Communications*, vol. 18, no. 3, pp. 535–547, 2000.

[164] A. Laya et al., "Goodbye, ALOHA!" *IEEE Access*, vol. 4, pp. 2029–2044, 2016.

[165] O. Haddad, M. A. Khalighi, and A. Zubow, "Wireless body-area networks in medical applications using optical signal transmission," in *Optical Fiber Communication Conference (OFC) 2021*, San Francisco, CA, Optical Society of America, 2021, Th4F.1.

[166] W. Xu and G. Campbell, "A near perfect stable random access protocol for a broadcast channel," in *[Conference Record] SUPERCOMM/ICC '92 Discovering a New World of Communications*, Chicago, IL, USA, 1992, 370–374 vol.1.

[167] W. Xu and G. Campbell, "A distributed queueing random access protocol for a broadcast channel," in *Conference Proceedings on Communications Architectures, Protocols and Applications*, San Francisco, CA, USA, 1993, pp. 270–278.

[168] X. Zhang and G. Campbell, "Performance analysis of distributed queueing random access protocol–DQRAP"," en, Computer Science Dept. IIT, DQRAP Research Group Report 93-1, 1993.

[169] L. Alonso, R. Agusti, and O. Sallent, "A near-optimum MAC protocol based on the distributed queueing random access protocol (DQRAP) for a CDMA mobile communication system," *IEEE Journal on Selected Areas in Communications*, vol. 18, no. 9, pp. 1701–1718, 2000.

[170] B. Otal, L. Alonso, and C. Verikoukis, "Highly reliable energy-saving MAC for wireless body sensor networks in healthcare systems," *IEEE Journal on Selected Areas in Communications*, vol. 27, no. 4, pp. 553–565, 2009.

[171] B. Otal, L. Alonso, and C. Verikoukis, "Design and analysis of an energy-saving distributed MAC mechanism for wireless body sensor networks," *EURASIP Journal on Wireless Communications and Networking*, vol. 2010, no. 1, p. 571 407, 2010.

[172] J. Yuan, H. Shan, A. Huang, T. Q. S. Quek, and Y. Yao, "Massive machine-to-machine communications in cellular network: Distributed queueing random access meets MIMO," *IEEE Access*, vol. 5, pp. 2981–2993, 2017.

[173] A. K. Pandey and N. Gupta, "An energy efficient distributed queuing random access (EE-DQRA) MAC protocol for wireless body sensor networks," *Wireless Networks*, vol. 26, no. 4, pp. 2875–2889, 2020.

[174] *Infrared transceiver module (SIR, 115.2 kbit/s)for IrDA applications*, TFDU4101, Data sheet, Vishay Semiconductors, Mar. 2020.

[175] *2.4 GHz IEEE 802.15.4 / ZigBee-ready RF transceiver*, CC2420, Data sheet, Texas Instruments, Sep. 2020.

[176] G. Bolch, S. Greiner, H. Meer, and K. Trivedi, *Queueing Networks and Markov Chains: Modeling and Performance Evaluation With Computer Science Applications, Second Edition*. J. Wiley & Sons, Apr. 2006, pp. 869–878.

[177] V. N. Swamy, S. Suri, P. Rigge, M. Weiner, G. Ranade, *et al.*, "Cooperative communication for high-reliability low-latency wireless control," in *2015 IEEE International Conference on Communications (ICC)*, London, UK, 2015, pp. 4380–4386.

RÉSUMÉ:

Les solutions de e-santé connaissent une popularité croissante dans un certain nombre de scénarios d'application en tant que moyens efficaces pour améliorer la qualité de vie et réduire les coûts des soins de santé. Les exemples typiques sont la surveillance en temps réel des patients dans les centres de soins et la télésurveillance des patients post-opératoires ou des personnes âgées à domicile. Ces solutions peuvent être réalisées grâce aux réseaux corporels (WBAN), où un certain nombre de capteurs médicaux situés à l'intérieur et/ou sur le corps collectent et transmettent les signes vitaux des patients à un centre médical par l'intermédiaire de coordinateurs et de points d'accès. Concernant la connectivité des réseaux WBAN, un certain nombre de solutions ont été proposées jusqu'à présent sur la base de la technologie radiofréquences (RF), utilisant principalement les bandes non licenciées. Cependant, les considérations relatives aux interférences RF, à la sécurité des données et à l'impact possible des ondes RF sur les tissus suggèrent les communications optiques sans fil (OWC) comme une alternative appropriée. Cette thèse porte sur la caractérisation et la modélisation du canal WBAN optique d'une part, et les schémas de signalisation appropriés, en particulier, pour gérer la fonctionnalité d'accès multiple (MA) de ces réseaux, d'autre part. Nous considérons d'abord la caractérisation des liaisons infrarouges (IR) intra et extra-WBAN dans un environnement hospitalier typique et étudions les effets de la mobilité et du blocage des faisceaux causés par corps du patient. Pour cela, en simulant un mouvement réaliste du patient à l'aide d'une approche de tracé de rayons Monte-Carlo, nous estimons la réponse impulsionnelle du canal (CIR) et dérivons les statistiques du premier et du second ordre des paramètres du canal tels que le gain DC, retard de propagation et le temps de cohérence. De plus, nous proposons des modèles statistiques basés sur l'approximation optimal (best-fit) et la densité de noyau (kernel densité) pour décrire la distribution de ces paramètres pour un scénario plus général. Sur la base de cette étude initiale, nous évaluons les performances de ces liaisons intra et extra WBAN en termes de probabilité de blocage et quantifions l'amélioration des performances lors de l'utilisation de plusieurs points d'accès (AP). Dans un deuxième temps, nous nous focalisons sur la transmission du signal depuis les capteurs médicaux vers un point d'accès et étudions, dans ce contexte, les schémas MA appropriés dans la couche physique (PHY) et la couche de contrôle d'accès au support (MAC). En particulier, nous étudions le schéma m-CAP MA, basé sur la modulation d'amplitude et de phase sans porteuse a bande multiple (m-CAP) et le schéma des files d'attente distribuées (DQRA). Nous démontrons l'adéquation de la signalisation DQRA aux WBAN à base optique et l'amélioration obtenue en termes de délai d'accès, et de consommation d'énergie par rapport à d'autres schémas.

MOTS-CLÉS : Communications optiques sans fil, reseaux corporels, modelisation de canal, acces multiple.

ABSTRACT:

E-Health solutions are gaining increasing popularity in a number of application scenarios as efficient means for improving the quality of life and reducing health-care costs. Typical examples include real-time monitoring of patients in health-care centers and telemonitoring post-operative patients or elderly people at home. These can be realized through the use of medical wireless body-area networks (WBANs), where a number of in- and/or on-body medical sensors collect and transmit vital information to a medical center through coordinators and an access points. Concerning wireless connectivity for WBANs, a number of solutions have been proposed so far based on the radio-frequency (RF) technology, mostly using unlicensed frequency bands. However, the considerations of RF interference, data security, and the possible impact of RF waves on the tissues suggests optical wireless communications (OWC) as a suitable alternative. This thesis focuses on the characterization and modeling of the optical WBAN channel on one hand, and appropriate signaling schemes, in particular, for managing the multiple access (MA) feature of these networks, on the other hand. We first consider the characterization of the intra- and extra-WBAN infra-red (IR) links in a typical hospital environment and investigate the effects of mobility and beam shadowing due to the patient's body. For this, simulating a realistic body movement using Monte-Carlo ray-tracing , we estimate the channel impulse response (CIR) and derive the first- and second-order statistics of the channel parameters such as DC gain, delay spread, and coherence time. Furthermore, we propose best-fit distribution and kernel-density statistical models to describe the distribution of these parameters for a more general scenario. Based on this initial study, we evaluate the performance of such intra- and extra-WBAN links in terms of outage probability and quantify the performance improvement when using multiple access points (APs). At a second step, we focus on the signal transmission from the medical sensors to an AP and inves-

tigate appropriate MA schemes in the physical and medium-access control layers within this context. In particular, we study the MA scheme based on multi-band carrier-less amplitude and phase (m-CAP), the carrier-sense MA with collision avoidance (CSMA/CA), and the distributed queuing random access (DQRA) scheme, and demonstrate the improvement achieved through DQRA signaling in terms of access delay and energy consumption.

KEY WORDS : Optical wireless communications, wireless body area networks, channel modeling, multiple access.

Adresse :

Institut Fresnel, UMR CNRS 7249, Ecole Centrale Marseille,
D.U. de Saint Jérôme, 13397 Marseille - France.